Modelling winter precipitation heterogeneities within an urban area

Dissertation

zur Erlangung des Doktorgrades

an der Fakultät für Mathematik, Informatik und Naturwissenschaften

Fachbereich Erdsystemwissenschaften

der Universität Hamburg

vorgelegt von

Karolin Sarah Samsel

Hamburg, 2025

Fachbereich Erdsystemwissenschaften

Datum der Disputation:	15.05.2025
Gutachter*innen der Dissertation:	Prof. Dr. K. Heinke Schlünzen
	Dr. Kevin Sieck
Zusammensetzung der Prüfungskommission:	Prof. Dr. K. Heinke Schlünzen
	Dr. Kevin Sieck
	Prof. Dr. Bernd Leitl
	Prof. Dr. Jürgen Böhner
	Prof. Dr. Lars Kutzbach
Vorsitzender des Fach-Promotionsausschusses Erdsystemwissenschaften:	Prof. Dr. Hermann Held
Dekan der Fakultät MIN:	Prof. Dr.-Ing. Norbert Ritter

Zusammenfassung

Städte beeinflussen die Verteilung von Regen und Schnee am Boden. Heterogenitäten im Niederschlag treten auch auf der Nachbarschaftsskala auf, die ein Gebiet von $\mathcal{O}(1\,\mathrm{km}^2)$ umfasst. Trotz ansteigender Temperaturen aufgrund des globalen Klimawandels wird Schnee weiterhin eine Rolle in Städten im warmgemäßigten Klima spielen. Niederschlagsereignisse mit Schnee wirken sich auf Gesundheit und Komfort aus. Anpassungsmaßnahmen für den Sommer könnten im Winter unerwünschte Auswirkungen haben. Um den Einfluss urbaner Effekte auf Winterniederschlag zu untersuchen, sind hochaufgelöste Daten notwendig, die mittels numerischer Modellierung hergestellt werden können. Diese Daten sollten in der Lage sein, ein Winterereignis in einer Stadt im warmgemäßigten Klima realistisch zu repräsentieren. In dieser Arbeit wird die notwendige Modellkomplexität für eine realistische Repräsentation untersucht.

Ein Winterniederschlagsschema, das Regen und Schnee als Niederschlag sowie Schneebedeckung berücksichtigt, wurde dem mikroskaligen, hindernisauflösenden Modell MITRAS hinzugefügt. Für die Auswahl der Schemas wurden bereits existierende Parameterisierungen im Modellsystem, die Modellskala und die beabsichtigten Anwendungsfälle berücksichtigt. Im Modellsystem wird bereits ein Drei-Kategorien-Bulk-Modell für warme Wolken verwendet. Um Gebäudewände korrekt mit einzubeziehen, wurde die Diffusion von Skalaren angepasst und Randbedingungen an Gebäudewänden für Wassergehaltsvariablen wurden eingeführt. Die Parameterisierung der Wolkenmikrophysik wurde durch ein Ein-Kategorie Eisschema erweitert, das Schnee als Niederschlag beinhaltet und sich für Mischphasenwolken eignet. Schneebedeckung am Boden wurde mit einem Schneeschema umgesetzt, in dem eine einzelne Schneelage angenommen wird.

Das Winterniederschlagsschema wurde validiert, indem die Ergebnisse verschiedener Modellversionen mittels Trefferquoten verglichen wurden. Für die Trefferquoten von Tempera-

tur, Strahlung und Niederschlag wurden Schwellwerte abgeschätzt, die auf der Rechengenauigkeit beruhen. Das führte zu einem strikten Vergleichskriterium um Programmierfehler zu entdecken. Die Schwellwerte für die Abweichungen sind $0,02\,\mathrm{ms}^{-1}$ (5 %) für die Windkomponenten, $0,05\,\mathrm{K}$ (0,02 %) für die Temperatur, $0,5\,\mathrm{Wm}^{-2}$ (0,5 %) und $0,5\,\mathrm{Wm}^{-2}$ (0,2 %) für die netto Lang- und Kurzwellenstrahlung und $0,001\,\mathrm{mm}$ (1 %) für den Niederschlag am Boden. Die Vergleiche offenbaren die zu erwartenden Unterschiede und zeigen, dass das erweiterte Modell plausible Resultate erzeugt. Das erweiterte Modell ist dafür geeignet, Winterniederschlag zu repräsentieren.

Sensitivitätstudien für veschiedene Anfangswindgeschwindigkeiten, Niederschlagsmengen, Windrichtungen, Temperaturen und Gebietsanordnungen wurden durchgeführt. Dabei wurde entweder die wolkenmikrophysikalische Parameterisierung für warme Wolken oder für Mischphasenwolken angewendet. Es stellte sich heraus, dass die Stadtstruktur sich auf das Niederschlagsmuster am Boden auswirkt. Es gibt hoch-reichende Effekte von Gebäuden auf die atmosphärische Durchmischung und auf die Wolkenprozesse sowie nichtlineare Effekte von Gebäuden und Orographie. Im Falle von Schnee wurden häufiger kleinskalige Variationen des Niederschlags am Boden auf der Gebäudeskala ($\mathcal{O}(10\,\mathrm{m})$) gefunden, die von Gebäuden erzeugten Winden verursacht wurden. Der Grund ist die geringere Sedimentationsgeschwindigkeit von Schnee. Es hat sich gezeigt, dass das Schmelzen von Schnee durch benachbarte Wasserflächen und durch Temperaturadvektion aufgrund von Straßenschluchtzirkulationen beeinflusst wird.

Für eine realistische Repräsentation eines Winterereignisses innerhalb der Hindernisschicht einer Stadt im warmgemäßigten Klima sollte die Topographie der Stadt (d.h. Gebäude und Orographie) aufgelöst werden und die Sedimentationsgeschwindigkeiten von Schnee und Regen sollten simuliert werden. Zusätzlich sollten Wasserflächen berücksichtigt werden.

Abstract

Urban areas impact the distribution of rain and snow on ground. Precipitation heterogeneities also occur on the neighbourhood scale, which covers areas of $\mathcal{O}(1\,\mathrm{km}^2)$. Despite increasing mean temperatures due to global climate change, snow will remain a feature of winter in warm temperate climate cities. Snow fall events impact human health and comfort. Adaptation measures for summer could have adverse effects in winter. For investigations of urban effects on winter precipitation, high-resolution data is required, which can be generated using numerical modelling. This data should realistically represent a winter event in a warm temperate climate city. In this thesis, the model complexity needed for a realistic representation is assessed.

A winter precipitation scheme considering precipitating rain and snow as well as snow cover was added to the microscale, obstacle-resolving model MITRAS. The schemes were chosen by taking pre-existing parameterisations within the model system, model scale and intended use cases into account. A three-category bulk water-continuity model designed for warm clouds was already applied in the model system. For considering building walls properly, the diffusion of scalars was adjusted and boundary conditions for water content variables at obstacle surfaces were introduced. The cloud microphysics parameterisation was extended with a one-category ice scheme designed for mixed-phase clouds, that includes precipitating snow. Snow cover on ground was realised using a single layer snow cover scheme.

The winter precipitation scheme was validated by comparing the results of different model versions using hit rates. For the hit rates of temperature, radiation, and precipitation, threshold values were estimated based on computational accuracy leading to strict accuracy criteria to detect programming errors. The deviation thresholds are $0.02\,\mathrm{ms}^{-1}$ (5 %) for the wind components, 0.05 K (0.02 %) for temperature, $0.5\,\mathrm{Wm}^{-2}$ (0.5 %) and $0.5\,\mathrm{Wm}^{-2}$ (0.2 %) for the net long and short wave radiation, and 0.001 mm (1 %) for precipitation on ground. The

comparisons reveal expected differences and show that the extended model produces plausible results. The extended model is suitable for representing winter precipitation.

Sensitivity studies were performed for different initial wind speeds, precipitation amounts, wind directions, temperatures, and domain configurations using either a cloud microphysical parameterisation suited for warm clouds or mixed-phase clouds. The city structure is found to impact the precipitation pattern on ground. There are high-reaching effects of buildings on atmospheric mixing and cloud processes and non-linear effects of buildings and orography. In case of snow fall, more small-scale variations of precipitation on ground on a building scale ($\mathcal{O}(10\,\mathrm{m})$) caused by building induced winds are found. This is due to the lower sedimentation speed of snow compared to rain. Snow melt is found to be affected by neighbouring water surfaces and temperature advection by street canyon circulations.

For a realistic representation of a winter event within the canopy layer of a warm temperate climate city, the city's topography (i.e. buildings and orography) should be resolved and the sedimentation speed of snow and rain should be simulated. In addition, water surfaces should be considered.

List of Publications

Ferner, K. S. and M. Boettcher and K. H. Schlünzen (2023): Modelling the heterogeneity of rain in an urban neighbourhood with an obstacle-resolving model. *Meteorologische Zeitschrift* 32(1), 67-81. http://dx.doi.org/10.1127/metz/2022/1149.

Samsel, K. S. and M. Boettcher and D. Grawe and K. H. Schlünzen and K. Sieck: A method for assessing model extensions: Application to modelling winter precipitation with a microscale obstacle-resolving meteorological model (MITRAS v4.0). *Geoscientific Model Development*, in review.

Samsel, K. S. and M. Boettcher and D. Grawe and K. H. Schlünzen and K. Sieck: Modelling snow processes in an urban neighbourhood using an obstacle-resolving model. Submitted to *Meteorologische Zeitschrift*.

Ferner, K. S. and M. Boettcher and K. Sieck and V. Voss (2024): Sensitivity studies on rain heterogeneity in Hamburg city centre using the obstacle-resolving model MITRAS. *World Data Center for Climate (WDCC) at DKRZ*.
https://doi.org/10.26050/WDCC/MitrasWinterHamburg.

Samsel, K. S. (2024): A method for assessing model extensions: Application to modelling winter precipitation with a microscale obstacle-resolving meteorological model (MITRAS v4.0). *Zenodo*. https://doi.org/10.5281/zenodo.14269493.

Contents

List of Figures

List of Tables

1 Introduction

1.1 Motivation

The effects of urban areas on precipitation patterns on ground have been scarcely researched for winter in a warm temperate climate city on a building scale ($\mathcal{O}(10\,\mathrm{m})$) to neighbourhood scale ($\mathcal{O}(1\,\mathrm{km})$). The scales are defined following table 2.1 in WMO (2023b) covering characteristic horizontal lengths of 10 m to $1-2$ km (microscale β and α).

Snowy conditions are a common feature in winters of warm temperate climate with humid winters (Kottek et al., 2006). There are hazards associated with snowy conditions cites including and not limited to hypothermia and traffic accidents (Haney, 2020). For instance, Hamburg's municipal winter service (Stadtreinigung Hamburg) found that the winter season 2023/2024 was more demanding than the season before. Instead of 5 860 tons of de-icing salt and gravel, 15 500 tons were applied in order to keep pedestrian crossings, bike lanes, bus stops, and roads safe (Stadtreinigung Hamburg, 2024). Yet, in 2023, 68 people were injured due to snowy or icy conditions on roads, five of them seriously (Statistik Nord, 2024).

Numerous analyses on human comfort in urban areas focus on summer (e.g. Theeuwes et al., 2013; Marginean et al., 2024; Lopez-Cabeza et al., 2024), but there are rarely any for winter conditions. In their systematic review on human thermal comfort in urban outdoor spaces, Costa et al. (2024) mentioned only few studies, that investigated cold stress. Also, to lessen the impacts of the expected increasing temperatures in urban areas in summer, measures for adaptation to global climate change are introduced in several urban areas. But how do those adaptation measures perform in the winter season? Could they even have adverse effects?

Even though the effects of adaptation measures in the winter season are not well studied, there are hints for adverse effects. For instance, Boettcher (2017) investigated the influences of adaptation measures developed for summer on the winter climate for the regional scale

for the metropolitan area of Hamburg. She found increasing wind speeds for a scenario with increasing population and temperatures, and with widespread implementation of adaptation measures. This can negatively impact wind comfort. Another example is the investigation on how applying national codes for city design affects outdoor thermal comfort performed by Haddid and Al-Obaidi (2022) for Bristol and Cardiff, UK. Even though they found overall a positive effect in summer, in winter, under certain circumstances, extreme cold stress could occur.

Analyses of human comfort and studies of adaptation measures in urban areas provide climate-related information, which can be transformed into customised products for climate services. In order to conduct studies for the building and neighbourhood scale for the winter season, high-resolution data is required, which includes precipitation and snow cover. Data obtained via numerical modelling is able to meet these requirements. The aim of this work is to provide the foundation for the creation of numerical model data, which can be utilised for a wide range of investigations.

1.2 Urban impacts on precipitation and snow cover in winter

Urban effects on precipitation are threefold: thermodynamic, chemical and dynamic. Thermodynamic effects include the well-researched phenomenon of the Urban Heat Island, where the temperatures within a city are higher at night-time compared to their surroundings. In winter, this affects the phase of precipitation (i.e. rain or snow) reducing snowfall events downwind of city centres (Oke et al., 2017). More specifically, in 81 % of nearly 5000 pairs of urban and rural areas the snow probability is smaller in the urban region (Salvi and Kumar, 2024). Also Perryman and Dixon (2013) found a decrease of snowfall downwind of city centres in 9 of 13 cases, but the detention of some enhanced events indicates additional urban effects. An urban area not only emits warmth, it is also a source of aerosols (chemical) and moisture (thermodynamic). Aerosols influence cloud formation and precipitation by causing

snowfall enhancement (Oke et al., 2017).

In summer, the above mentioned processes cause rainfall enhancement downwind of urban areas (Shepherd, 2005; Han et al., 2014; Song et al., 2016; Oke et al., 2017; Liu and Niyogi, 2019; Zhang et al., 2022; Lu et al., 2024; Katzfey et al., 2024). In their meta-analysis, Liu and Niyogi (2019) found an average rainfall increase of 18 % approximately 52 km downwind the city. However, for winter, not enough studies were available for a statistically sound analysis. Katzfey et al. (2024) investigated urban influences on precipitation by comparing global model results with and without an urban parameterisation. They found increases in precipitation for northern extratropic urban areas and a dependency of the urban impact on season and time of day. Analyses of precipitation events in the area of St. Louis, USA, revealed a higher occurrence of rainfall enhancement, when atmospheric conditions are conductive to convection (Changnon et al., 1991). In winter, synoptic-scale events like frontal precipitation associated with cyclones are more common. During those events, Changnon et al. (1991) found little evidence of rainfall enhancement indicating that urban effects on the regional scale tend to be masked in winter.

Dynamic effects are caused by urban obstacles such as buildings, bridges, trees, etc. affecting the surface roughness. While in general the wind speed is reduced, turbulence is increased (Oke et al., 2017). Even single buildings or street canyons can have high-reaching impacts on the regional scale. For instance, Song et al. (2016) found in sensitivity studies that rain fall enhancement in summer is 3.85 % higher for a non-uniform city structure (mix of various urban densities fitting to the study area Nanjing, China) than for a uniform (high-density residential) city structure. Moreover, they found the best agreement with observations for the non-uniform city structure. Since out of the test cases the non-uniform city structure is the most similar to the study area, this indicates the importance of considering the geometry of an urban area in numerical models.

In general, snow cover has a high albedo, which decreases with snowmelt, and adds an

insulating layer on ground. All of this influences the surface radiative exchange and heat transfer (Dong, 2018). Without snow, the urban-rural albedo difference is between -0.09 and 0.03 (Oke et al., 2017) – the urban area is usually darker. With snow cover, the albedo increase in the surrounding area is more pronounced than in the urban area, leading to albedo contrasts of -0.55 to -0.11. Assuming a difference in the snow albedo of 0.2 and a mean solar radiation of $200\,\mathrm{W\,m^{-2}}$, the daily snowmelt in a city would be 10 mm higher than in a rural environment (Dobre et al., 2017). The increase of the average albedo in urban areas is less pronounced, because snow cover in urban areas is more patchy and darker. The patchiness results from urban topography and human activity. On the one hand, snow cover is removed by snowmelt due to the increased urban warmth, by winter services, or by traffic (Oke et al., 2017). For instance, Shui et al. (2019) found that the mean albedo after snowfall decreased due to snowmelt by 30 % at an urban site compared to 10 % at a rural side. At the urban site snow on pavements was removed causing a decrease in the mean albedo. On the other hand, the remaining snow is also affected by the urban area. The albedo of snow is lower in a city due to pollution, which influences the short wave radiation balance. Moreover, buildings not only cast shadows, they also reflect and emit radiation. The extent of the radiation emitted by buildings depends on their temperature and emissivity and its influence is pronounced under clear skies. The before mentioned building induced wind fields affect the sensible and latent heat, which are expected to be higher in cities compared to rural areas (Dobre et al., 2017).

On the building scale, obliquely falling rain, so-called wind-driven rain, is researched for instance in building science due to its effects on hygrothermal performance and durability of building facades (Blocken and Carmeliet, 2004). Even though the building configuration, i.e. stand-alone building, street canyon, etc., significantly impacts the surface wetting distribution on building facades, the understanding of the effects of surrounding buildings is still lacking (Gholamalipour et al., 2022). The study areas used for investigations of the snow distribution

are usually cities, that experience heavy snow, which is an exceptionally rare occurrence in warm temperate climate cities. Heavy snow may cause unbalanced loads on buildings, therefore the research focus lies on accumulation due to snow drift. For a realistic representation of the snow distribution, models need to include snow drift, i.e. transport processes occurring after the snow particles have reached the ground (Tominaga et al., 2011). This has been investigated using wind tunnel experiments (e.g. Watanabe et al., 2017; Zhang et al., 2021; Zhou et al., 2021) and numerical modelling (e.g. Tominaga, 2018; Chen et al., 2021).

1.3 Climate of Hamburg

A suitable focus area for studying winter climate is Hamburg, Germany. The city has a warm temperate climate (following Kottek et al., 2006), which is characterised by a fully humid climate with warm summers and mild winters. Snow as precipitation is relevant in winter and will be found in future winters in Hamburg (Bell, 2024). For 1981-2010, the area mean temperature in winter was 1.5 °C (9 °C for the whole year). In these decades, the mean precipitation sum for the whole year was 720 mm. For Hamburg-Fuhlsbüttel, a mean number of 28 days with snow cover was observed (Meinke et al., 2018). Compared to the mean winter precipitation of 1961-1990, observations show a statistically significant increase of 26 % from 1881 to 2014, which is likely to continue (Wiesner et al., 2018). Based on the results in Schlünzen et al. (2010) and her own analysis of station data from Hamburg-Fuhlsbüttel, Bell (2024) concluded that temperatures around and below freezing point might remain a regular occurrence until the end of this century.

1.4 Research Questions

Even in warm temperate climate cities with mild winters, snowy and icy conditions impact city dwellers. For investigations on human thermal comfort or the effects of adaptation measures in winter on a building to neighbourhood scale, numerical modelling is a suitable method.

However, in the previous sections a research gap concerning the representation of winter events within a warm temperate climate city on a neighbourhood scale was identified. This leads to the guiding research question of this thesis:

GRQ: What model complexity is needed for a realistic representation of a winter event within a warm temperate climate city?

For this, a microscale and obstacle-resolving model will be enhanced with a winter precipitation scheme. There are various established parameterisations for the inclusion of snow cover (Lee et al., 2023) and precipitation (Khain et al., 2015) in numerical models depending on model scale and intended use cases. A parameterisation represents processes or structures, that are too small to be explicitly resolved. For example, in contrast to models with resolutions of $\mathcal{O}(1\,\mathrm{m})$, obstacles cannot be resolved in a model with grid resolutions of $\mathcal{O}(10\,\mathrm{km})$. Instead, physical processes like this are parameterised using experimental data or simplified fundamental concepts. As long as the representation is quantitatively accurate, the parameterisation may be computationally simple (Pielke, 2013).

This leads to the first subsidiary research question:

RQ 1: What model complexity is needed for a winter precipitation scheme in a microscale obstacle-resolving model?

Usually, the quality of numerical models is assessed by comparing model results with field measurements, wind tunnel data, or numerical model results. This process is called validation. Field measurements are not necessarily more accurate than other types of comparison data, and all types of data carry uncertainties (Oberkampf and Trucano, 2002). Physical modelling data is commonly used for the validation of numerical models (Schatzmann and

Leitl, 2011), but it is rarely applied for precipitation in urban neighbourhoods. According to Blocken and Carmeliet (2004), using wind tunnels for analyses of surface wetting on buildings, is labour intensive, expensive and difficult, which negatively impacts the accuracy.

The second subsidiary research question therefore addresses the quality assessment of the parameterisation:

RQ 2: How to validate a winter precipitation scheme without high-resolution measurement data?

The validated extended microscale, obstacle-resolving model is applied and sensitivity tests are performed for various meteorological situations and topographies to investigate the third subsidiary research question of this thesis:

RQ 3: How do obstacles influence precipitation heterogeneities within an urban neighbourhood?

The implementation of the winter precipitation scheme in MITRAS (RQ 1) as well as a method for the assessment of model extensions (RQ 2) is provided in Chapter 2. In Chapter 3, the heterogeneity of rain and in Chapter 4, the heterogeneity of snow are investigated. The research questions are answered in Chapter 5.

2 A method for assessing model extensions: Application to modelling winter precipitation with a microscale obstacle-resolving meteorological model (MITRAS v4.0)

Preface

This chapter was submitted for publication as:

Samsel, K. S. and M. Boettcher and D. Grawe and K. H. Schlünzen and K. Sieck: A method for assessing model extensions: Application to modelling winter precipitation with a microscale obstacle-resolving model (MITRAS v4.0). *Geoscientific Model Development*, in review.

The full manuscript of the submitted paper is included in this chapter. Layout and numbering within the manuscript were adopted to fit this thesis. All references are combined in References. Supporting information and statements submitted with this manuscript can be found in Appendix A. Symbols are adjusted and the list of symbols provided with this manuscript is combined with all symbols used in this thesis in List of Symbols.

K. H. Schlünzen has contributed to the conceptualisation and contributed some ideas for the analysis. M. Boettcher, K. H. Schlünzen and D. Grawe contributed to the discussion of the results.

2.1 Abstract

The microscale, obstacle-resolving meteorological transport and stream model MITRAS has been extended with a snow cover and precipitation scheme. The performance of the model extension is assessed by comparing the results of different model versions using a method based on hit rates originally developed for assessing wind performance. For temperature, radiation and precipitation, estimates for the threshold values were derived based on computational accuracy; these are used in the hit rate calculation for these variables. The threshold

values for the deviations are $0.02\,\mathrm{ms}^{-1}$ (5 %) for the wind components, 0.05 K (0.02 %) for temperature, $0.5\,\mathrm{Wm}^{-2}$ (0.5 %) and $0.5\,\mathrm{Wm}^{-2}$ (0.2 %) for the net long and short wave radiation, and 0.001 mm (1 %) for precipitation on ground. The model extensions produce plausible results and better represent winter precipitation. This opens the opportunity to study with higher accuracy the influence of obstacles on precipitation heterogeneities.

2.2 Introduction

Climate change related impacts on the urban climate in winter situations are usually investigated focusing on cities in high-latitude or cold climate regions, where high snow loads are expected. Multiple studies based on measuring campaigns were performed on the influence of snow on, e.g., the Urban Heat Island in Minneapolis (USA) (Malevich and Klink, 2011), in the Twin Cities metropolitan area (Minneapolis-St. Paul, USA) (Smoliak et al., 2015), or in Madison (USA) (Schatz and Kucharik, 2014). Special focus on the impact of snow cover and snow melt on the surface energy balances was laid in studies for example in Montreal (Canada) (Lemonsu et al., 2008, 2010; Bergeron and Strachan, 2012), in Calgary (Canada) (Ho and Valeo, 2005), or in Harbin (China) (Shui et al., 2019). Also, numerical examinations were carried out for example for Sapporo (Japan) (Mori and Sato, 2015) or for Yichun (China) (Shui et al., 2016).

Investigating the influence of urban areas on patterns of rainfall (Hu et al., 2024; Lu et al., 2024; Zhang et al., 2022; Liu and Niyogi, 2019) and snowfall (Salvi and Kumar, 2024) received more and more interest in the scientific community. Local scale influences of obstacles on the heterogeneity of snow has been investigated using wind tunnel experiments with focus on urban block designs (Watanabe et al., 2017), or on the interference of high-rise buildings on the snow load on a low-rise building (Zhang et al., 2021), or on snowdrift on flat roofs during snowfall (Zhou et al., 2021).

Increasing computational power allows the use of high resolution in modelling. In numer-

ical models, fit-for-purpose microphysical schemes are used to model precipitation processes depending on the scale of the model. At global scales, simple schemes with one ice phase are applied (Roeckner et al., 2003). The sedimentation of falling hydrometeors is often neglected, i.e. precipitation is falling from the cloud to the surface in one time step, because the numerical time step is large enough to justify this assumption. With increasing resolution, more elaborated schemes are used. Typical regional weather and climate models use multi-moment schemes (e.g., Doms et al., 2011) and take into account e.g. evaporation of rain during sedimentation over several time steps, which requires special treatment of the sedimentation in order to keep numerical stability (e.g., Bouteloup et al., 2011; Doms et al., 2011; Geleyn et al., 2008).

Available obstacle-resolving models do not yet commonly consider precipitation. The microscale model MITRAS, for instance, includes a precipitation scheme (Ferner et al., 2023). The obstacle-resolving high-resolution urban climate model PALM-4U, which is based on PALM (Maronga et al., 2020), does not include precipitation, yet (Maronga et al., 2019). The Regional Atmospheric Modeling System (RAMS) (Pielke et al., 1992) includes a parameterisation for cloud processes and has also been used for flow simulations around obstacles (Castelli and Reisin, 2010), but no investigations of precipitation within urban neighbourhoods were performed.

Studies specifically focusing on the influence of obstacles on snow are predominantly conducted for snow climate cities. Less severe snowfall occurs in warm temperate climate cities like Hamburg (Germany) (Meinke et al., 2018); it still influences e.g. pedestrian comfort due to icy grounds or public transport due to snow covered bus stops. For these smaller snow loads, other processes might have a stronger influence on the heterogeneity of snow than for the high loads. Information on snow heterogeneities within an urban area are a useful first step for analyses concerning frost heterogeneities or human comfort. To our knowledge, there is no obstacle-resolving model currently available, that includes both rain and snow. In this

paper, a description of the implemented winter precipitation scheme in the obstacle-resolving model MITRAS (Schlünzen et al., 2003; Salim et al., 2018) is provided as well as plausibility tests and their results to assess the reliability of the new scheme. The implemented processes are included in MITRAS v4.0, which also includes other developments.

A short description of MITRAS v3.0 is given in Section 2.3. The model extensions for MITRAS v3.1 concerning the diffusion of scalars and the newly introduced boundary conditions for rain on building surfaces are described in Section 2.4. The representation of snow cover and the adjustments made for scale and obstacles for MITRAS v3.3 can be found in Section 2.5. Note that the model extensions for MITRAS v3.2 (Badeke et al., 2021) are not within the scope of this paper. The extension of the cloud microphysics is described in Section 2.6. The changes to the model are tested for plausibility by comparing the above-mentioned model versions in Section 2.7. Finally, conclusions and outlook are given in Section 2.8.

2.3 The obstacle-resolving model MITRAS

The three-dimensional, non-hydrostatic, prognostic, **MI**croscale, obstacle-resolving **TRA**nsport and **S**tream model **MITRAS** is part of the M-SYS model system (Trukenmüller et al., 2004; Schatzmann et al., 2006). The basic equations are written in flux form, transformed into a terrain-following coordinate system, $\dot{x}^1$, $\dot{x}^2$, $\dot{x}^3$, and filtered using Reynolds averaging (Salim et al., 2018). As a consequence, the atmospheric state variables are divided into an average value over a finite time and grid volume and its deviation. For scalar quantities ϕ such as temperature or humidity the average value is further decomposed into a basic state value, ϕ_0, and its microscale deviation, $\tilde{\phi}$ (Pielke, 2013).

The equations are numerically solved on an Arakawa C grid (Arakawa and Lamb, 1977). Scalar quantities such as temperature or cloud and rain water content are defined at grid cell centres (scalar points), whereas the u-wind is defined at the x-boundaries of the grid

cell, the v-wind at the y-boundaries, and the w-wind at the vertical (z) boundaries; these are named vector grid points. Obstacle surfaces are positioned at vector grid points. Obstacles are simulated by assuming impermeable grid cells at the building position using 3-D fields of weighting factors. The weighting factors contain the information whether a grid cell lies in the atmosphere or in a building. Weighting factors are additionally used to define whether a grid cell's boundary denotes a building face (Briscolini and Santangelo, 1989; Mittal and Iaccarino, 2005).

The solved prognostic equation for a scalar quantity includes advection, diffusion $\overline{F}_{\overline{\phi}}$ (Eq. 2.1) containing the subgrid-scale turbulent fluxes, as well as sources and sinks (Schlünzen et al., 2018a; Salim et al., 2018). The subgrid-scale fluxes of scalars mathematically result from averaging the model equations. The flux terms prevent closing the coupled nonlinear equations system. Consequently, solutions to this so-called "closure problem" are needed, which are presented in Section 2.3.1. The cloud microphysics parameterisation for warm rain is given Section 2.3.2. As the model is well documented (Salim et al., 2018; Schlünzen et al., 2018a; Fischereit, 2018), only a brief description of those parts of MITRAS v3.0, that will be extended, are provided in the following. The model extensions are given in Sects. 2.4 to 2.6.

2.3.1 Diffusion term

The diffusion term is given in the terrain-following coordinate system as

$$\begin{aligned}\overline{F}_{\overline{\phi}} =& \frac{\partial}{\partial \dot{x}^1}\left(\alpha^* \rho_0 \overline{u'\phi'} \frac{\partial \dot{x}^1}{\partial x}\right) + \frac{\partial}{\partial \dot{x}^2}\left(\alpha^* \rho_0 \overline{v'\phi'} \frac{\partial \dot{x}^2}{\partial y}\right) \\ &+ \frac{\partial}{\partial \dot{x}^3}\left(\alpha^* \rho_0 \overline{u'\phi'} \frac{\partial \dot{x}^3}{\partial x} + \alpha^* \rho_0 \overline{v'\phi'} \frac{\partial \dot{x}^3}{\partial y} + \alpha^* \rho_0 \overline{w'\phi'} \frac{\partial \dot{x}^3}{\partial z}\right)\end{aligned} \tag{2.1}$$

with the grid volume α^*, the basic state atmospheric density ρ_0, the wind velocity components u, v, w, and Cartesian coordinates x, y, z. The fluxes are parameterised using a

first-order closure

$$-\rho_0 \overline{u'\phi'} = \rho_0 K_{\text{hor}} \left(\frac{\partial \overline{\phi}}{\partial \dot{x}^1} \frac{\partial \dot{x}^1}{\partial x} + \frac{\partial \overline{\phi}}{\partial \dot{x}^3} \frac{\partial \dot{x}^3}{\partial x} \right) \tag{2.2}$$

$$-\rho_0 \overline{v'\phi'} = \rho_0 K_{\text{hor}} \left(\frac{\partial \overline{\phi}}{\partial \dot{x}^2} \frac{\partial \dot{x}^2}{\partial y} + \frac{\partial \overline{\phi}}{\partial \dot{x}^3} \frac{\partial \dot{x}^3}{\partial y} \right) \tag{2.3}$$

$$-\rho_0 \overline{w'\phi'} = \rho_0 K_{\text{ver}} \left(\frac{\partial \overline{\phi'}}{\partial \dot{x}^3} \frac{\partial \dot{x}^3}{\partial z} \right) \tag{2.4}$$

with the horizontal and vertical exchange coefficients K_{hor} and K_{ver}, respectively (Schlünzen et al., 2018a; Salim et al., 2018). Inserting the expressions for the subgrid-scale turbulent fluxes (Eqs. 2.2-2.4) into the diffusion term (Eq. 2.1) leads to the equations as used in the prior model version MITRAS v3.0 (Salim et al., 2018; Schlünzen et al., 2018a; Fischereit, 2018).

2.3.2 Microphysics for warm clouds

In the M-SYS model system (Schlünzen et al., 2018a), a Kessler-type parameterisation (Kessler, 1969) is applied (Köhler, 1990). It is a three-category (water vapour q_1^1, cloud water q_1^{2c}, and rain water q_1^{2r}) bulk water-continuity model designed for warm clouds (Doms, 1985; Köhler, 1990). In Section 2.6 Fig. 2.3, the processes included in the warm scheme are shown in grey and black.

Liquid water drops in the atmosphere are distinguished by their droplet size. Drops with a mean drop radius of about 10 μm are considered cloud water, whereas drops with a mean radius of about 100 μm are defined as rain water. The separation radius is 40 μm (Schlünzen et al., 2018a). For rain drops, the Marshall-Palmer size distribution (Marshall and Palmer, 1948) is assumed.

A terminal velocity is the mass weighted mean of the individual sedimentation speeds. The following expression for the terminal velocity of rain, v_{TR}, is used (Köhler, 1990; Schlünzen

et al., 2018a)

$$v_{\mathrm{TR}} = 68.81\,\frac{\mathrm{m}}{\mathrm{s}}\left(\frac{\mathrm{m}^3}{\mathrm{kg}}\right)^{0.1905} \cdot \left(10^{-3}\cdot\rho_0 q_1^{2\mathrm{r}}\right)^{0.1905} \tag{2.5}$$

which is taken from Doms (1985), recalculated to SI-units. To take the smaller densities at higher altitudes into account, a correction factor

$$F = \sqrt{\frac{\rho_{\mathrm{ref}}}{\rho_0}} \tag{2.6}$$

with the reference density $\rho_{\mathrm{ref}} = 1.29\,\mathrm{kg\,m^{-3}}$ is included. The terminal velocity is thus larger for larger altitudes.

The coagulation of cloud water drops leads to new rain water drops, which is called autoconversion. For the autoconversion process to start, enough cloud drops, that are big enough to allow coagulation, have to be present (Doms, 1985). The critical value is taken as $q_{1,\mathrm{cri}}^{2\mathrm{c}} = 10^{-3}\,\mathrm{kg\,kg^{-1}}$. Above the critical value, rain water production depends linearly on the cloud water content with the inverse autoconversion interval $k_{\mathrm{warm}}^{\mathrm{r}} = 10^{-3}\,\mathrm{s^{-1}}$. Consequently, the autoconversion rate for the warm rain scheme is

$$B_{\mathrm{au}}^{\mathrm{w}} = \max\left(0, k_{\mathrm{warm}}^{\mathrm{r}}\cdot\left(q_1^{2\mathrm{c}} - q_{1,\mathrm{cri}}^{2\mathrm{c}}\right)\right) \tag{2.7}$$

(Köhler, 1990; Schlünzen et al., 2018a).

Accretion is the growth of rain drops by collecting cloud drops. The parameterisation of this process is based on the continuous model for droplet growth. It assumes a uniform and continuous distribution of cloud drops, as well as that their radii are much smaller than the rain drop radii and that the cloud drop sedimentation speed is zero (Doms, 1985). This leads to the accretion equation

$$B_{\mathrm{acc}}^{\mathrm{w}} = \frac{934.63}{\mathrm{s}}\left(\frac{\mathrm{m}^3}{\mathrm{kg}}\right)^{0.875} \cdot q_1^{2\mathrm{c}} \cdot \left(10^{-3}\cdot\rho_0\cdot q_1^{2\mathrm{r}}\right)^{0.875} \tag{2.8}$$

(Köhler, 1990; Schlünzen et al., 2018a) which is the original equation by Doms (1985) converted to SI units.

The calculation of condensation and evaporation to and from cloud droplets is based on the method of saturation adjustment (Asai, 1965). It assumes that within a cloud, saturation is achieved. The sedimentation flux of cloud droplets is neglected. If the humidity exceeds the saturation specific humidity $q^1_{1,\mathrm{sat}}$, condensation is

$$B_{\mathrm{cond}} = \frac{q^1_1 - q^1_{1,\mathrm{sat}}}{\alpha_{\mathrm{cond}}} \tag{2.9}$$

with the condensation parameter

$$\alpha_{\mathrm{cond}} = 1\,\mathrm{s} + \frac{I_{21} \cdot q^1_{1,\mathrm{sat}} \cdot 4028\,\mathrm{K\,s}}{c_{\mathrm{p}} \cdot \left(T \cdot \left(\frac{p_0}{p_{\mathrm{S}}}\right)^{\frac{R}{c_{\mathrm{p}}}} - 38.33\,\mathrm{K}\right)^2} \tag{2.10}$$

with the latent heat of vaporisation I_{21}, the specific heat for dry air c_{p}, temperature T, basic state pressure p_0, the ground surface pressure p_{S}, and the gas constant for dry air R (Köhler, 1990; Schlünzen et al., 2018a).

In the sub-saturated areas below the cloud, evaporation of rain water may occur. The evaporation is given as

$$B_{\mathrm{evap}} = A_{\mathrm{t}} \cdot \sqrt{\rho_0 \cdot 10^{-3} \cdot q^{2\mathrm{r}}_1} \cdot F_{\mathrm{v}} \cdot \frac{S}{\rho_0 \cdot 10^{-3}} \tag{2.11}$$

with saturation S and the parameter for the rain droplet spectrum

$$A_{\mathrm{t}} = \frac{2.623 \cdot 10^{-3}\ \left(\frac{\mathrm{m}^3}{\mathrm{kg}}\right)^{0.5}\ \frac{1}{\mathrm{s}} \cdot \left(\rho_0 \cdot 10^{-3} \cdot q^1_{1,\mathrm{sat}}\right)}{1 + 1.282 \cdot 10^{10}\ \frac{\mathrm{m^3 K^2}}{\mathrm{kg}} \cdot \left(\rho_0 \cdot 10^{-3} \cdot q^1_{1,\mathrm{sat}}\right) \theta^{-2}} \tag{2.12}$$

and the ventilation factor

$$F_{\mathrm{v}} = 0.78 + 80.73 \left(\frac{\mathrm{kg}}{\mathrm{m}^3}\right)^{-0.225} \cdot \left(\rho_0 \cdot 10^{-3} \cdot q_1^{2\mathrm{r}}\right)^{0.225} \tag{2.13}$$

(Köhler, 1990; Schlünzen et al., 2018a). The potential temperature is given as θ.

The influence of liquid water on radiation is included in the radiation parameterisation in MITRAS (Schlünzen et al., 2018a; Fischereit, 2018; Uphoff, 2019). There are two radiation schemes implemented: the two-stream approach and the vertically integrated approach, which does not consider clouds. Thus, only the two-stream approach can be applied when atmospheric liquid water is present. For the long wave radiation, cloud and rain water is included in the calculation of the absorption coefficient. For the short wave radiation, only small droplets like cloud water are taken into account when deriving scattering and absorption by liquid water (Uphoff, 2019).

2.4 Modification of turbulent scalar fluxes

The cloud microphysics parameterisation (Section 2.3.2) was implemented in the mesoscale sister model METRAS (Schlünzen et al., 2018a; Köhler, 1990), which does not resolve obstacles. To include liquid water contents in MITRAS, adjustments are made for the diffusion at obstacle surfaces, which apply to all scalar quantities (Section 2.4.1). Additionally, boundary conditions for cloud, rain and snow water content at obstacles are introduced (Section 2.4.2).

2.4.1 Changes in the model domain

The horizontal subgrid-scale fluxes depend on both the grid surface parallel gradient of ϕ (first terms in brackets on the right hand side in Eqs. 2.2 and 2.3), and on the vertical gradients (second terms in brackets). The latter result from the transformation into the terrain-following coordinate system. However, the terrain-following coordinates create some numerical problems at obstacle walls. To explain these, the calculation of the diffusion in

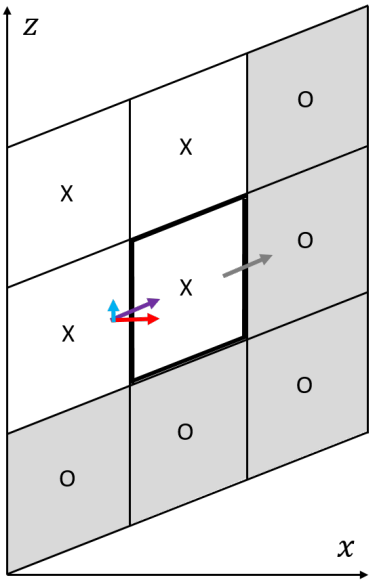

Figure 2.1: Example for the calculation of the diffusion in x-direction (violet and grey arrow parallel to grid cell boundaries) in a grid cell (thick black boundary) prior to model enhancements. The diffusive fluxes including the horizontal and vertical gradient of the scalar quantity are represented by the red and blue arrow. The grey arrow represents the obstacle surface flux. Obstacle cells are grey. Scalar quantities are defined at the crosses (atmospheric grid cells) and circles (building grid cells).

x-direction of e.g. liquid water content in a terrain-following grid cell will serve as an example (Fig. 2.1). An obstacle cell (shaded grey) is assumed below and in x-direction of the grid cell for which the diffusion is calculated (thick black boundary). The diffusion in x- direction following Eqs. (2.1)-(2.3) results in

$$\overline{F}_{\overline{\phi},\dot{x}^1} = -\frac{\partial}{\partial \dot{x}^1}\left(\alpha^* \rho_0 K_{\text{hor}} \frac{\partial \overline{\phi}}{\partial \dot{x}^1}\frac{\partial \dot{x}^1}{\partial x}\frac{\partial \dot{x}^1}{\partial x} + \alpha^* \rho_0 K_{\text{hor}} \frac{\partial \overline{\phi}}{\partial \dot{x}^3}\frac{\partial \dot{x}^3}{\partial x}\frac{\partial \dot{x}^1}{\partial x}\right). \tag{2.14}$$

The diffusion is the grid following gradient $\partial/\partial\dot{x}^1$ of the fluxes through the vertical grid cell boundaries (purple and grey arrow in Fig. 2.1). With a building at the right hand side of the grid cell, the flux is not calculated following Eq. (2.14). Instead, a specific building surface flux is applied (Section 2.4.2).

For the calculation of the fluxes between atmospheric grid cells, the grid following gradient $\partial/\partial\dot{x}^1$ and vertical gradients of ϕ are required. The first term in brackets is represented as

the violet arrow and the second as the blue arrow in Fig. 2.1. The calculation of the grid following $\partial/\partial\dot{x}^1$ gradient of ϕ is straight forward using the values of ϕ located at the grid cell centres left and right from the grid cell boundary (crosses in the central and middle left grid cell in Fig. 2.1). For the calculation of the vertical gradient, however, values of ϕ from all six grid cells, that surround the grid cell boundary, are used (two left columns of grid cells). This includes in the example provided in Fig. 2.1 two building grid cells (grey), which give no physically useful values. When the horizontal diffusion is calculated, only fluxes through vertical walls are taken into account.

In general, the orography in MITRAS with the resolution of a few metres is relatively flat. Therefore, the second term in brackets in Eq. (2.14), which includes the slope of the terrain as $\partial\dot{x}^3/\partial x$, is small. By neglecting the influence of terrain steepness in the horizontal flux, Eq. (2.14) simplifies to only the first term. Similar simplifications can be done for the diffusion in the y-direction. This leads to the following expressions for the horizontal turbulent fluxes:

$$-\rho_0\overline{u'\phi'} = \rho_0 K_{\text{hor}}\frac{\partial\overline{\phi}}{\partial\dot{x}^1}\frac{\partial\dot{x}^1}{\partial x} \tag{2.15}$$

$$-\rho_0\overline{v'\phi'} = \rho_0 K_{\text{hor}}\frac{\partial\overline{\phi}}{\partial\dot{x}^2}\frac{\partial\dot{x}^2}{\partial y}. \tag{2.16}$$

2.4.2 Changes at obstacle surfaces

Boundary fluxes had been defined before for all scalar quantities at obstacle surfaces, except for cloud, rain and snow water content. For MITRAS, those quantities are added and the treatment of building surface fluxes at obstacle surfaces is adapted for all scalar quantities.

Previously, building surface fluxes for $\rho_0\overline{u'\phi'}$, $\rho_0\overline{v'\phi'}$, and $\rho_0\overline{w'\phi'}$ were defined as a three-dimensional variable located at scalar grid points. Wall orientation was taken into account in the calculation of the building surface fluxes, but when more than one building surface was present, only the value, that has been calculated last, was stored in the variable. For

the example of a building edge as in Fig. 2.1, the same building surface flux was used for the vertical wall (grey arrow) as for the roof below (bottom boundary of central grid cell). Therefore, the structure of the building surface flux variables has been adjusted for all scalar quantities. Like other building surface variables (e.g. building surface temperature), a value is defined for each obstacle adjacent atmospheric grid cell and for each wall orientation. For the calculation of the pre-existing building surface fluxes, boundary conditions as described in Salim et al. (2018); Schlünzen et al. (2018a) are applied.

For liquid water at the ground surface, the model allows for three surface boundary conditions: zero gradient, prescribed fixed value, and flux at the boundary equal to flux in the atmosphere above. For obstacle surfaces, the latter is chosen. Water and snow reaching a building close to the wall is considered to be absorbed by the adjacent surface. Considering again the configuration in Fig. 2.1: In order to get the building surface flux at the obstacle wall in positive x-direction of the atmospheric grid cell (grey arrow), the flux at the opposite grid cell boundary is used, calculated following Eqs. (2.1) and (2.15) (Ferner et al., 2023, Section 3.3.3). The same approach is applied for other wall directions and for cloud, rain and snow water content.

2.5 Consideration of a snow cover scheme in MITRAS

The microscale model MITRAS' mesoscale sister model METRAS (Trukenmüller et al., 2004; Schatzmann et al., 2006; Schlünzen et al., 2018a) includes a snow cover scheme, which is described in Boettcher (2017). In the present study, a similar approach has been adapted in MITRAS. In METRAS, the snow cover scheme is only used when flux aggregation with the blending height concept is applied (von Salzen et al., 1996). In MITRAS, however, the effects of surface fractions and corresponding subgrid-scale fluxes are significantly lower due to the small grid cell sizes. Therefore, using the parameter averaging method is suitable (Schlünzen et al., 2018a) and the snow cover scheme is adapted to it. Additional adjustments are made

for the consideration of obstacles, as well as for the smaller time spans and time steps of MITRAS model runs.

2.5.1 Surface energy budget at the ground

Without snow, the change of temperature at ground surface, T_S, with time t is calculated following Eq. (2.17) in MITRAS considering net short and long wave radiation SW_{net} and LW_{net}, sensible and latent heat fluxes H_S and L_S, heat flux to and from the soil at the surface G_{soil} (Eq. 2.19), using thermal diffusivity k_{soil}, thermal conductivity ν_{soil}, and deep soil temperature $T_{h,soil}$ at the depth h_{soil}.

$$\frac{\partial T_S}{\partial t} = B^* \left(SW_{net} + LW_{net} + H_S + L_S + G_{soil}\right) \tag{2.17}$$

with

$$B^* = 2\sqrt{\pi}\frac{k_{soil}}{\nu_{soil} h_{soil}} \tag{2.18}$$

The soil heat flux G_{soil} (Eq. 2.19), is expressed using the force-restore method (Bhumralkar, 1975; Deardorff, 1978). The deep soil temperature can be assumed constant for shorter time ranges ($<$ 3 days).

$$G_{soil} = -\sqrt{\pi}\left(\frac{h_{soil}}{\nu_{soil}}\right)^{-1}\left(T_S(t) - T_{h,soil}\right) \tag{2.19}$$

In case of snow on ground, an additional snow layer is assumed, which impacts the temperature on and near the ground surface as described for METRAS in Boettcher (2017). The treatment of the snow layer is based on Hirota et al. (2002). The thermal diffusivity of snow k_{snow} is given in Eq. (2.20) using the snow volumetric heat capacity $c_{v,snow}$ (Eq. 2.21). The snow thermal conductivity ν_{snow} (Eq. 2.22) and volumetric heat capacity $c_{v,snow}$ both depend on the density of the snow pack ρ_{snow} (Eq. 2.28). The snow thermal conductivity, the

snow volumetric heat capacity, and the depth of the temperature wave into the snow are given in Eqs. (2.22)-(2.23) using the specific heat capacity of ice c_{ice}, the density of ice ρ_{ice}, the thermal conductivity of ice ν_{ice}, and the period of the temperature wave $\tau = 86400\,s = 1\,d$.

$$k_{\text{snow}} = \frac{\nu_{\text{snow}}}{c_{\text{v,snow}}} \tag{2.20}$$

$$c_{\text{v,snow}} = \frac{c_{\text{ice}} \cdot \rho_{\text{snow}}}{\rho_{\text{ice}}} \tag{2.21}$$

$$\nu_{\text{snow}} = \nu_{\text{ice}} \cdot \left(\frac{\rho_{\text{snow}}}{\rho_{\text{w}}} \right)^{1.88} \tag{2.22}$$

$$h_{\text{snow}} = \sqrt{\tau \cdot \frac{\nu_{\text{snow}}}{c_{\text{v,snow}}}} \tag{2.23}$$

The snow depth z_{snow} (Eq. 2.24) is calculated using the snow water equivalent SWE (Eq. 2.29) and the density of water ρ_{w}.

$$z_{\text{snow}} = SWE \cdot \frac{\rho_{\text{w}}}{\rho_{\text{snow}}} \tag{2.24}$$

Two cases form limit value situations which are to be treated as follows: In case of a shallow snow cover, meaning, the depth of the temperature wave into the snow h_{snow} (Eq. 2.23) exceeds the snow depth z_{snow} (Eq. 2.24), the heat conduction of snow cover and snow soil heat flux can be expressed with Eqs. (2.25) and (2.26) using Eq. (2.20).

$$B^* = 2\sqrt{\pi} \frac{1}{c_{\text{v,snow}} z_{\text{snow}}} \tag{2.25}$$

$$G_{\text{soil}} = -\sqrt{\pi} \left(\frac{z_{\text{snow}}}{\nu_{\text{snow}}} + \frac{h_{\text{soil}}}{\nu_{\text{soil}}} \right)^{-1} \cdot \left(T_{\text{S}}(t) - T_{\text{h,soil}} \right). \tag{2.26}$$

In case of a very thick snow cover, the heat wave does not reach below the snow and h_{soil} becomes zero leading to a soil heat flux of Eq. (2.27) (Boettcher, 2017). The heat

conduction B^* is calculated following Eq. (2.25) but using the temperature depth in snow h_{snow} instead of the snow depth z_{snow}.

$$G_{\text{soil}} = -\sqrt{\pi}\left(\frac{h_{\text{snow}}}{\nu_{\text{snow}}}\right)^{-1}(T_{\text{S}}(t) - T_{\text{h,soil}}) \tag{2.27}$$

2.5.2 Snow density

As a snow pack ages, its density (Eq. 2.28) increases. Boettcher (2017) assumes an asymptotic solution with time from a minimum density ρ_{min} to a maximum density ρ_{max} with the empirical parameters τ_{f} and τ_1 and time step Δt following Verseghy (1991); Douville et al. (1995); Dutra et al. (2010).

$$\rho_{\text{snow}}(t + \Delta t) = (\rho_{\text{snow}}(t) - \rho_{\text{max}}) \cdot \exp\left(-\tau_{\text{f}}\frac{\Delta t}{\tau_1}\right) + \rho_{\text{max}} \tag{2.28}$$

The parameters were chosen according to Verseghy (1991) with $\rho_{\text{min}} = 100\,\text{kg}\,\text{m}^{-3}$, $\rho_{\text{max}} = 300\,\text{kg}\,\text{m}^{-3}$, $\tau_{\text{f}} = 0.24$ and $\tau_1 = 86400\,\text{s}$.

For the snow albedo (Section 2.5.5), the parameters suggested by Järvi et al. (2014) were chosen in the implementation of the obstacle-resolving microscale model over those suggested by Verseghy (1991) and Boettcher (2017), as they fit observations in an urban area better by considering anthropogenic pollution. For the snow density, however, we decided to keep the parameters suggested by Verseghy (1991). The parameterisation in MITRAS is supposed to represent a snow event in a city like Hamburg (Germany). The parameters suggested by Järvi et al. (2014) fit well for snow climate cities like Montreal or Helsinki, but they do not necessarily fit equally well for Hamburg, where larger snow packs are rare.

2.5.3 Snow water equivalent

The snow water equivalent SWE (Eq. 2.29) with the unit of metres represents the mass of snow using an equivalent water height. In contrast, the height of the snow pack is given in Eq. (2.24). The snow water equivalent is reduced by evaporation E and melting M (Eq. 2.30). The rate of snowfall Pr_{snow} adds to it (Boettcher, 2017).

$$\frac{\partial SWE}{\partial t} = Pr_{\text{snow}} - E - M \tag{2.29}$$

In Boettcher (2017), no precipitating snow is calculated. Rain reaching the ground is assumed to be snow, if the surface temperature is below the freezing point T_0. In MITRAS, precipitating snow is calculated (Section 2.6.1) and considered in the rate of snowfall. For simplicity, rain is assumed to be snow on ground for surface temperatures below the freezing point. Similarly, precipitating snow reaching the ground for temperatures above freezing point, is assumed to be rain in the calculation of the soil water content. Diffusive fluxes into the ground are only possible in the absence of a snow cover. As a consequence, for air temperatures above freezing point, with both snow and rain falling, the snow water equivalent might be overestimated, if the surface temperatures are below the freezing point.

Snow melt (Eq. 2.30) is calculated following Boettcher (2017) using the latent heat of fusion l_{32}.

$$M = \frac{\nu_{\text{snow}}}{\rho_{\text{w}} l_{32} z_{\text{snow}}} \left(T_{\text{S}} - T_0\right) \tag{2.30}$$

2.5.4 Snow roughness length

The roughness length of snow-covered areas is reduced compared to snow-free areas as a snow pack smooths a surface. The roughness length z_0 under the influence of snow (Eq. 2.31) is calculated using the snow roughness length $z_{0_{\text{snow}}} = 10^{-3}\,\text{m}$, the roughness length

of areas without snow cover $z_{0_{\text{ini}}}$, and the snow cover fraction $p_{\text{snow}_{z_0}}$ (Eq. 2.32) following Boettcher (2017).

$$z_0 = (1 - p_{\text{snow}_{z_0}}) \cdot z_{0_{\text{ini}}} + p_{\text{snow}_{z_0}} \cdot z_{0_{\text{snow}}} \tag{2.31}$$

The parameterisation of the snow cover fraction (Eq. 2.32) is based on Douville et al. (1995) with the empirical factor $\beta = 0.408$.

$$p_{\text{snow}_{z_0}} = \frac{SWE}{SWE + \beta \cdot z_{0_{\text{ini}}}} \tag{2.32}$$

For now, the influence of snow cover on the roughness length of roofs is neglected. For obstacle surfaces including roofs, the roughness length for concrete ($z_0 = 10^{-3}\,\text{m}$) is assumed regardless of snow cover.

2.5.5 Snow albedo

If there is already a snow pack present, the albedo α of the ground surface (Eq. 2.33) is increased to a maximum albedo α_{max} after one hour of snowfall with the magnitude $0.01\,\text{m}\,\text{h}^{-1}$, or an equivalent value is used, e.g. with a higher magnitude for 0.01 m of snow in a shorter time (Boettcher, 2017; Dutra et al., 2010). The amount of snowfall is represented by the change of the snow water equivalent ΔSWE.

$$\alpha(t + \Delta t) = \alpha(t) + \min\left(1, \frac{\Delta SWE \cdot 3600\,\text{s}}{\Delta t \cdot 0.01\,\text{m}}\right) \cdot (\alpha_{\text{max}} - \alpha(t)) \tag{2.33}$$

Baker et al. (1991) found that a minimum snow depth of 5 cm is required to completely mask the albedo of the underlying soil. The effect of the surface covers shining through the snow surface is included in MITRAS. However, in a city like Hamburg, which aims at black roads in winter, snow rarely remains untouched because of winter services and traffic, which

means the albedo of the underlying soil (α_{ini}) shines through for snow depths greater than 5 cm. These effects of direct human activities are included by using a basic approach. The underlying albedo is considered until a snow depth of 0.5 m is reached, then a snow cover of fresh snow is assumed. This is represented by a linear relation (Eq. 2.34) using the critical snow water equivalent $SWE_{\text{crit}} = 0.05\,\text{m}$, which corresponds a snow depth of 0.5 m (Eq. 2.24). In MITRAS, Eq. 2.33 is used for snow albedo in case of snowfall with snow water equivalent higher than SWE_{crit}. Eq. 2.34 is used for values below SWE_{crit} with and without snowfall because the impact of the underlying soil is assumed to be larger than the impact of aging of the snow pack.

$$\alpha = \alpha_{\text{ini}} + \min\left(1, \frac{SWE}{SWE_{\text{crit}}}\right) \cdot (\alpha_{\text{max}} - \alpha_{\text{ini}}) \tag{2.34}$$

Without snowfall and a snow water equivalent greater than SWE_{crit}, the albedo is simultaneously decreased due to the aging of the snow pack. For temperatures below the freezing point, a linear decrease of the albedo to the minimum albedo α_{min} is assumed (Eq. 2.35) and if it is warmer, an exponential decrease (Eq. 2.36) is assumed using the empirical factors τ_α and $\tau_{\text{f},\alpha}$ following Verseghy (1991); Douville et al. (1995).

$$\alpha(t + \Delta t) = \alpha(t) - \tau_\alpha \cdot \frac{\Delta t}{\tau_1} \qquad \text{for } T_S < 273.16\,\text{K} \tag{2.35}$$

$$\alpha(t + \Delta t) = (\alpha(t) - \alpha_{\text{min}}) \cdot \exp\left(-\tau_{\text{f},\alpha} \cdot \frac{\Delta t}{\tau_1}\right) + \alpha_{\text{min}} \qquad \text{for } T_S > 273.16\,\text{K} \tag{2.36}$$

For the mesoscale model METRAS, the parameters provided by Verseghy (1991) are applied with $\alpha_{\text{min,V91}} = 0.5$, $\tau_{\alpha,\text{V91}} = 0.008$, and $\tau_{\text{f},\alpha,\text{V91}} = 0.24$ (Boettcher, 2017). However, the albedo in urban areas is generally lower than in rural areas mainly due to pollution. Järvi et al. (2014) assessed and evaluated parameters in a snow scheme for two cold climate cities

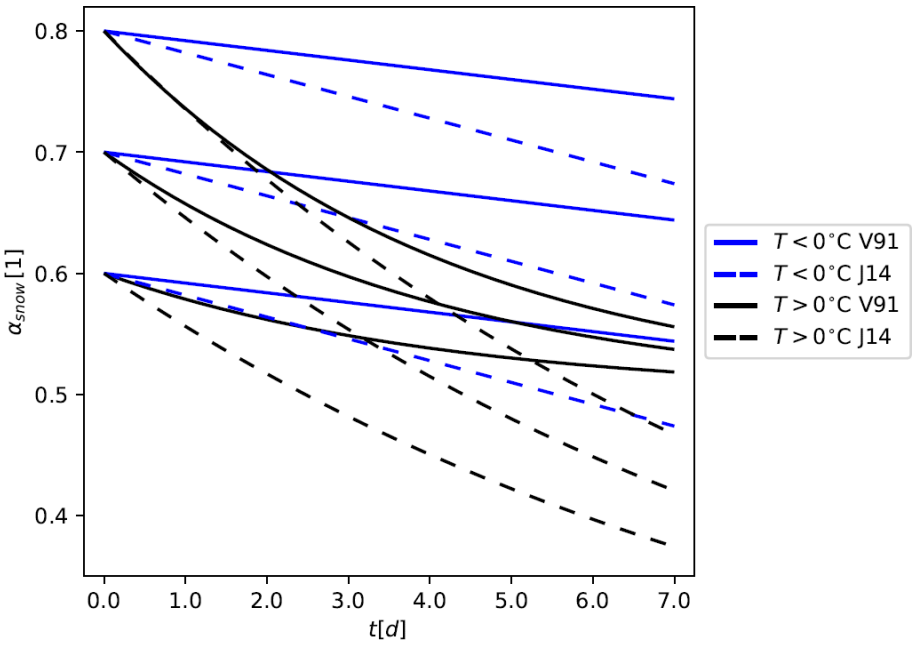

Figure 2.2: Linear (blue) and exponential (black) decrease of albedo of snow pack α_{snow} (Eqs. 2.35-2.36) as applied in METRAS ($\alpha_{\text{min}} = 0.5$, $\tau_{\text{f},\alpha} = 0.24$, $\Delta t = 5\text{s}$) after Verseghy (1991) (V91, solid lines) and as applied in MITRAS ($\alpha_{\text{min}} = 0.18$, $\tau_{\text{f},\alpha} = 0.11$, $\Delta t = 0.1\text{s}$) after Järvi et al. (2014) (J14, dashed lines).

(Helsinki and Montreal) and suggested the parameters: $\alpha_{\text{min,J14}} = 0.18$, $\tau_{\alpha,\text{J14}} = 0.018$, and $\tau_{\text{f},\alpha,\text{J14}} = 0.11$. Both Verseghy (1991) and Järvi et al. (2014) assume a maximum snow albedo of 0.85. In Fig. 2.2, the decreasing albedo as described with Eqs. (2.35) (blue lines) and (2.36) (black lines) is shown for the parameters used in METRAS after Verseghy (1991) (solid lines) and the parameters based on Järvi et al. (2014) in MITRAS (dashed lines). According to Järvi et al. (2014), their suggested parameters fit well with observations in an urban area, which is why their parameters were chosen for MITRAS as well.

2.6 Consideration of cloud microphysics in MITRAS

The aim of extending the cloud microphysics parameterisation in MITRAS is to enable the analysis of the influence of an urban area on precipitation. Due to the very short time steps needed for numerical stability (well below 1 second) in microscale models, explicitly resolving sedimentation is necessary. This also means that processes like accretion and sedimentation

have to be taken into account during the time step calculation. The representation of a winter precipitation event is significantly improved by including an ice phase in the parameterisation. Consequently, all state-of-the-art bulk parameterisations include ice processes (Khain et al., 2015). However, currently the purpose of MITRAS is not to realistically represent the processes forming a precipitating cloud, since domain sizes are small (1 to 5 km) and thus a full formation of a cloud can only be simulated for zero wind situations and small clouds. Therefore, extending MITRAS with a comparably simple one-category ice scheme as described in Doms et al. (2011) is sufficient. There, no cloud ice is defined, but it is assumed that any cloud ice is immediately transformed to snow particles (snow q_1^{3s}). The ice scheme processes are shown in blue in Fig. 2.3.

The processes of the three-category warm rain scheme used in the M-SYS model system (Schlünzen et al., 2018a; Köhler, 1990) are provided in Section 2.3.2 and shown in grey and black in Fig. 2.3. In the following, the treatment of rain on roofs for MITRAS v3.1 as well as the model extension enabling the simulation of mixed-phase clouds for MITRAS v3.3 is given.

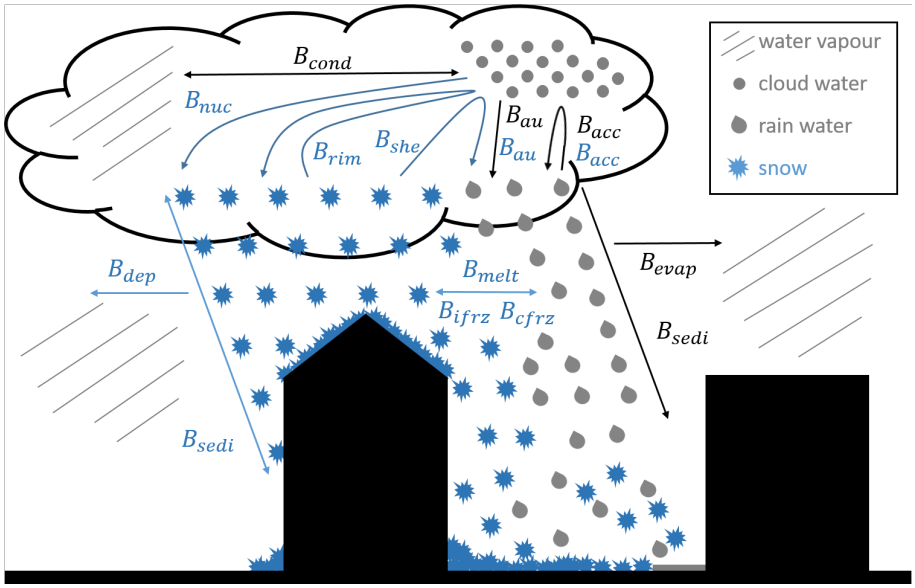

Figure 2.3: Cloud microphysics parameterisation with warm rain scheme in grey/ black and the one-category ice scheme in blue as introduced in MITRAS.

The following balance equations describe the microphysical processes in the extended cloud scheme:

$$\frac{\partial q_1^1}{\partial t} = - B_{\text{cond}} + B_{\text{evap}} - B_{\text{dep}} \tag{2.37}$$

$$\frac{\partial q_1^{2c}}{\partial t} = B_{\text{cond}} - B_{\text{au}}^{\text{c}} - B_{\text{nuc}} - B_{\text{acc}}^{\text{c}} - B_{\text{rim}} - B_{\text{she}} \tag{2.38}$$

$$\frac{\partial q_1^{2r}}{\partial t} = \frac{1}{\rho_0}\frac{\partial}{\partial z}\left(\rho_0 q_1^{2r} v_{\text{TR}}\right) + B_{\text{au}}^{\text{c}} + B_{\text{acc}}^{\text{c}} + B_{\text{she}} - B_{\text{evap}} + B_{\text{melt}} - B_{\text{ifrz}} - B_{\text{cfrz}} \tag{2.39}$$

$$\frac{\partial q_1^{3s}}{\partial t} = \frac{1}{\rho_0}\frac{\partial}{\partial z}\left(\rho_0 q_1^{2s} v_{\text{TS}}\right) + B_{\text{nuc}} + B_{\text{rim}} + B_{\text{dep}} - B_{\text{melt}} + B_{\text{ifrz}} + B_{\text{cfrz}} \tag{2.40}$$

$$\begin{aligned}\frac{\partial T}{\partial t} =& \frac{l_{21}}{c_{\text{p}}}\left(\frac{p_{\text{S}}}{p_{\text{ref}}}\right)^{-\frac{R}{c_{\text{p}}}}\left(B_{\text{cond}} - B_{\text{evap}}\right) + \frac{l_{31}}{c_{\text{p}}}\left(\frac{p_{\text{S}}}{p_{\text{ref}}}\right)^{-\frac{R}{c_{\text{p}}}} B_{\text{dep}} \\ &+ \frac{l_{32}}{c_{\text{p}}}\left(\frac{p_{\text{S}}}{p_{\text{ref}}}\right)^{-\frac{R}{c_{\text{p}}}}\left(B_{\text{nuc}} + B_{\text{rim}} - B_{\text{melt}} + B_{\text{ifrz}} + B_{\text{cfrz}}\right).\end{aligned} \tag{2.41}$$

The balance equations are given for water vapour (Eq. 2.37), cloud water content (Eq. 2.38), rain water content (Eq. 2.39), snow water content (Eq. 2.40), and temperature (Eq. 2.41) with the latent heat of sublimation l_{31}, and the reference pressure $p_{\text{ref}} = 100\,000\,\text{Pa}$ following Doms et al. (2011). Prior to the model extensions, water vapour could condensate and cloud water evaporate (Eq. 2.9). In the sub-saturated air below the cloud, evaporation of rain (Eq. 2.11) occurs and in the now extended MITRAS deposition and sublimation of snow (B_{dep}) as well (Section 2.6.4). The coagulation of cloud drops produces rain (autoconversion, B_{au}^{c}) or snow (nucleation, B_{nuc}) (Section 2.6.2). The accretion of rain ($B_{\text{acc}}^{\text{c}}$), riming of snow ($B_{\text{rim}}$), and shedding ($B_{\text{she}}$) by melting snow particles collecting cloud droplets thereby producing rain is included (Section 2.6.3). The first terms on the right hand sides of Eqs. (2.39) and (2.40) represent sedimentation with the terminal velocities of rain (Eq. 2.5) and snow (v_{TS}, Section 2.6.1). Melting (B_{melt}) as well as immersion freezing (B_{ifrz}) and contact nucleation (B_{cfrz}) of snow are now considered (Section 2.6.5). For snowflakes the Gunn-Marshall size distribution (Gunn and Marshall, 1958) is assumed.

For the radiation parameterisation in MITRAS v4.0, snow is represented as spherical droplets like rain and is added to the liquid water content within the calculation of the absorption coefficient for the long wave radiation (Section 2.3.2).

2.6.1 Sedimentation

The terminal velocity for snow of

$$v_{\mathrm{TS}} = 4.82\,\frac{\mathrm{m}}{\mathrm{s}}\left(\frac{\mathrm{m}^3}{\mathrm{kg}}\right)^{0.075} \cdot \left(10^{-3}\cdot\rho_0\cdot q_1^{3s}\right)^{0.075} \tag{2.42}$$

(Doms et al., 2011) is introduced. Smaller densities at higher altitudes again need to be taken into account (compare with Eq. 2.6). The terminal velocity of snow is lower than that of rain with a maximum value of $2.2\,\mathrm{ms}^{-1}$ (blue line in Fig. 2.4).

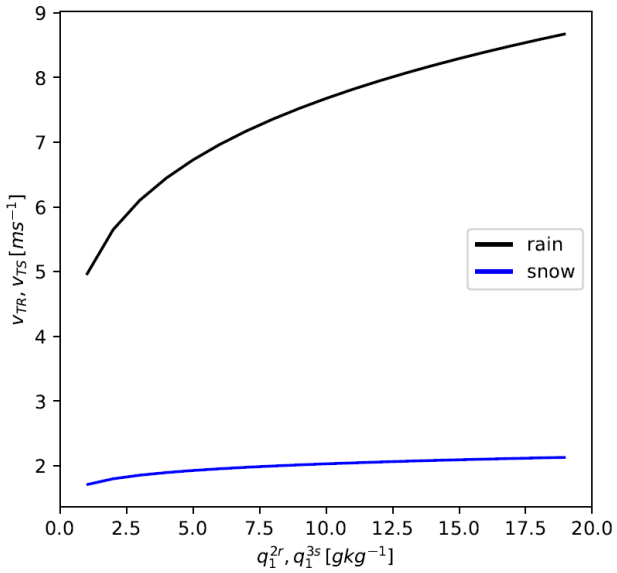

Figure 2.4: Terminal velocities of rain v_{TR} (black, Eq. 2.5) and of snow v_{TS} (blue, Eq. 2.42) as used in MITRAS.

In general, precipitation rates and amounts are only given at ground surface in atmospheric models. In MITRAS, however, these precipitation quantities should be given on roofs as well. Precipitation quantities on roofs are calculated similar to the precipitation variables on ground (Ferner et al., 2023, Section 3.3.3). For the sedimentation fluxes (first terms in Eqs. 2.39

and 2.40) in the atmosphere, the fluxes of rain and snow water content through the grid cell boundaries are calculated using the terminal velocity defined at vector points and rain and snow water content defined at grid cell centres. For the precipitation quantities at ground, a terminal velocity for the scalar point just above ground is calculated. The precipitation quantities are then derived from the flux of rain and snow above surface. In case of a roof, the terminal velocity is calculated similarly, thus using the scalar value of the terminal velocity just above the roof.

2.6.2 Autoconversion and nucleation

The development of snow from cloud water by subsequent diffusional growth is named nucleation. For the one-category ice scheme in MITRAS v3.3, a temperature dependence is considered:

$$\epsilon(T) = \begin{cases} 0 & \text{if } T \geq T_0 \\ 0.5\left[1 + \sin\left(\frac{\pi\cdot(0.5(T_0+T_2)-T)}{T_0-T_2}\right)\right] & \text{if } T_2 < T < T_0 \\ 1 & \text{if } T \leq T_2. \end{cases} \tag{2.43}$$

According to Doms et al. (2011), it is based on observations of the frequency distribution of water and ice in mixed-phase clouds. $\epsilon(T)$ is one below the minimum temperature $T_2 = 235.16\,\mathrm{K}$ and zero above the freezing point (T_0). Note that the conversion coefficient for Kelvin in MITRAS is 273.16 and not 273.15 as in (Doms et al., 2011).

The conversion rates are given as

$$B^{\mathrm{c}}_{\mathrm{au}} = \max(0, k^{\mathrm{r}}_{\mathrm{cold}} \cdot (1 - \epsilon(T)) \cdot \left(q_1^{2\mathrm{c}} - q^{2\mathrm{c}}_{1,\mathrm{cri}}\right) \tag{2.44}$$

$$B_{\mathrm{nuc}} = \max(0, k^{\mathrm{s}}_{\mathrm{cold}} \cdot \epsilon(T) \cdot \left(q_1^{2\mathrm{c}} - q^{2\mathrm{c}}_{1,\mathrm{cri}}\right) \tag{2.45}$$

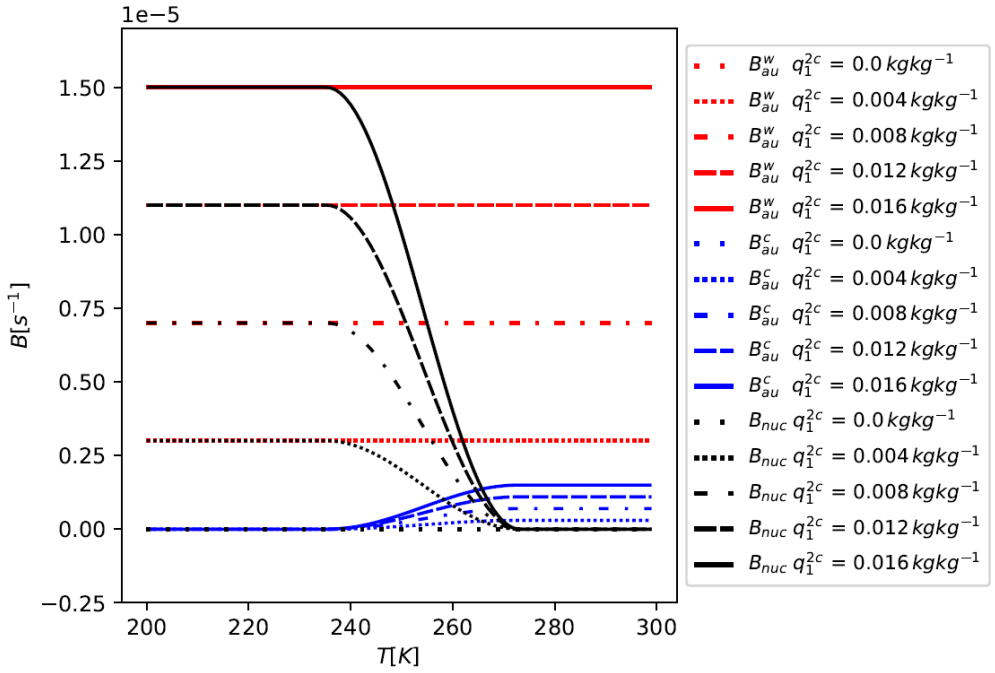

Figure 2.5: Autoconversion rates for warm clouds (red, $B_{\mathrm{au}}^{\mathrm{w}}$, Eq. 2.7) and mixed-phase clouds (blue, $B_{\mathrm{au}}^{\mathrm{c}}$, Eq. 2.44) and nucleation rates (black, B_{nuc}, Eq. 2.45) for different cloud water contents $q_1^{2\mathrm{c}}$ and temperatures T.

with the autoconversion interval for rain $k_{\mathrm{cold}}^{\mathrm{r}} = 10^{-4}\,\mathrm{s}^{-1}$ and for snow $k_{\mathrm{cold}}^{\mathrm{s}} = 10^{-3}\,\mathrm{s}^{-1}$ (Doms et al., 2011). Note that unlike in Doms et al. (2011), a nonzero value for $q_{1,\mathrm{cri}}^{2\mathrm{c}}$ is chosen in MITRAS.

In Fig. 2.5 the autoconversion rates for warm clouds (Eq. 2.7, red) and mixed-phase clouds (Eq. 2.44, blue) are shown as well as the nucleation rates (Eq. 2.45, black). All processes increase with increasing cloud water contents. While the autoconversion in the warm rain scheme only depends on the cloud water content, the other processes additionally depend on temperature. When mixed-phase clouds are assumed, less rain water is created by autoconversion than in warm clouds for the same cloud water content. Below $T_2 = 235.16\,\mathrm{K}$ the nucleation of snow is highest and the autoconversion is zero. The nucleation gradually decreases and the autoconversion increases with higher temperatures until the freezing point is reached.

2.6.3 Accretion and riming

For riming, the continuous model for particle growth by collection is applied. Snow particles have no spherical shapes. Instead, they are assumed to be rimed aggregates of crystals and they have the form of thin circular plates. The temperature dependent mass-size relation of snow is defined as

$$a_{\mathrm{m}}(T) = \begin{cases} a_{\mathrm{mc}} - a_{\mathrm{mv}} \left[1 + \cos\left\{\frac{2\pi(T - 0.5(T_0+T_1))}{(T_0-T_1)}\right\}\right] & \text{if } T_0 > T > T_1 \\ a_{\mathrm{mc}} & \text{else} \end{cases} \tag{2.46}$$

with the constant parameters $a_{\mathrm{mc}} = 0.08\,\mathrm{kg\,m^{-2}}$ and $a_{\mathrm{mv}} = 0.02\,\mathrm{kg\,m^{-2}}$ and the temperature $T_1 = 253.16\,\mathrm{K}$ (Doms et al., 2011).

For the accretion term (Eq. 2.8) in the one-category ice scheme, the temperature dependency (Eq. 2.43) is considered:

$$B^{\mathrm{c}}_{\mathrm{acc}} = (1 - \epsilon(T)) \cdot \frac{934.63}{\mathrm{s}} \left(\frac{\mathrm{m}^3}{\mathrm{kg}}\right)^{0.875} \cdot q_1^{2\mathrm{c}} \cdot \left(\rho_0 \cdot 10^{-3} \cdot q_1^{2\mathrm{r}}\right)^{0.875} \tag{2.47}$$

$$B_{\mathrm{rim,MITRAS}} = \begin{cases} \frac{1}{a_{\mathrm{m}}(T)} \cdot 3307.24\,\frac{\mathrm{kg}}{\mathrm{s\,m^2}} \left(\frac{\mathrm{kg}}{\mathrm{m}^3}\right)^{-1.075} \cdot q_1^{2\mathrm{c}} \cdot \left(\rho_0 \cdot 10^{-3} \cdot q_1^{3\mathrm{s}}\right)^{1.075} & \text{if } T < T_0 \\ 0 & \text{if } T \geq T_0. \end{cases} \tag{2.48}$$

Otherwise it remains the same as in MITRAS v3.0. Note that (Doms et al., 2011) uses different parameters for the accretion.

In Fig. 2.6, the accretion rates for the warm rain parameterisation used in MITRAS v3.0 (grey) and the mixed-phase cloud parameterisation as used in MITRAS v4.0 (light blue) is shown as well as the riming rates (dark blue). Accretion increases for rain for temperatures

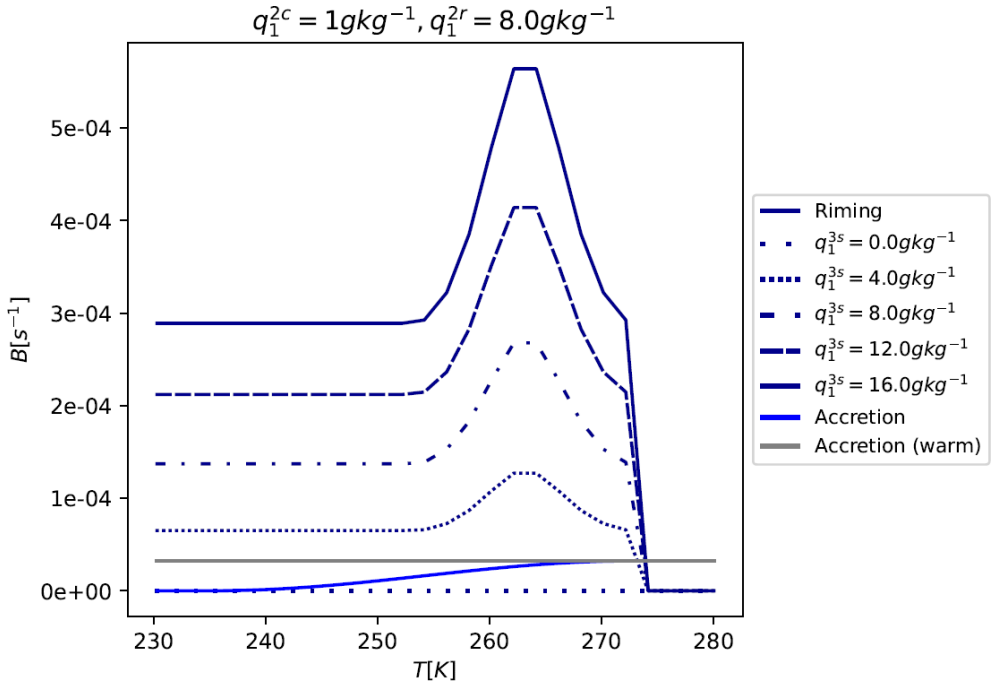

Figure 2.6: The riming rates (Eq. 2.48, dark blue) with the cloud water content of $q_1^{2c} = 1 \cdot 10^{-3}\,\mathrm{kg\,kg^{-1}}$ for various snow water contents q_1^{3s} depending on the temperature T and the accretion rates for $q_1^{2c} = 1 \cdot 10^{-3}\,\mathrm{kg\,kg^{-1}}$ and the rain water content $q_1^{2r} = 8 \cdot 10^{-3}\,\mathrm{kg\,kg^{-1}}$ for the mixed-phased cloud parameterisation as used in MITRAS v3.3 (Eq. 2.47, light blue) and warm cloud parameterisation as used in MITRAS v3.0 (Eq. 2.8, grey).

above T_2 (Eq. 2.43) reaching the same value as warm clouds at the freezing point T_0. The riming rate is highest at -10 °C, as the largest snowflakes can be found at $-10\,°C$ (Eq. 2.46). Snow production is higher than rain production for the same initial snow respectively rain amount.

At temperatures below the freezing point T_0, snow is produced by riming. If it is warmer, rain water content is produced by shedding. The equation is the same as riming (Eq. 2.48), but it produces rain water and not snow.

2.6.4 Depositional growth

With the inclusion of snow, depositional growth (diffusion growth of snow particles) and sublimation occur, which is according to Doms et al. (2011) given as

$$B_{\text{dep}} = \frac{\alpha_{\text{dep}}}{(a_{\text{m}}(T))^{0.5}} \left(1 + \frac{\beta_{\text{dep}}}{(a_{\text{m}}(T))^{0.25}} \left(\rho_0 q_1^{3\text{s}}\right)^{0.225}\right) \left(q_1^1 - q_{1,\text{sat,ice}}^1\right) \left(\rho_0 q_1^{3\text{s}}\right)^{0.625} \tag{2.49}$$

with the factors

$$\alpha_{\text{dep}} = \left(1.09 \cdot 10^{-3} - 3.34 \cdot 10^{-5} \left(T - T_0\right)\right) \tag{2.50}$$

and $\beta_{\text{dep}} = 13.0$. $q_{1,\text{sat,ice}}^1$ denotes the saturation specific humidity over ice. For better readability, the units of α_{dep} and β_{dep} are not provided here. They can be found in Doms et al. (2011).

2.6.5 Melting and freezing

The melting rate is derived similarly to the evaporation and deposition rates leading to

$$B_{\text{melt}} = \frac{\alpha_{\text{melt}}}{a_{\text{mc}}^{0.5}} \left(1 + \beta_{\text{melt}} a_{\text{mc}}^{0.25} \left(\rho_0 q_1^{3\text{s}}\right)^{0.225}\right) \left(T - T_0\right) \left(\rho_0 q_1^{3\text{s}}\right)^{0.625} \tag{2.51}$$

with the factors $\alpha_{\text{melt}} = 7.2 \cdot 10^{-6}$ and $\beta_{\text{melt}} = 13.0$ (Doms et al., 2011).

Rain drops can be activated as ice nuclei due to various drop impurities (immersion freezing), this is represented in the model as

$$B_{\text{ifrz}} = \alpha_{\text{if}} \left(\exp\left(\alpha_{\text{if}}(T_0 - T)\right) - 1\right) \left(\rho_0 q_1^{2\text{r}}\right)^{1.75} \tag{2.52}$$

with the parameter $\alpha_{\text{if}} = 9.95 \cdot 10^{-5}$ (Doms et al., 2011).

The process of falling rain drops collecting ice nuclei (contact freezing nucleation) is represented as

$$B_{\mathrm{cfrz}} = \begin{cases} \alpha_{\mathrm{cf}} E_{\mathrm{cf}} N_{\mathrm{cf},0} (270.17 - T)^{1.3} (\rho_0 q_1^{2\mathrm{r}})^{1.625} & \text{if } T < 270.17\,\mathrm{K} \\ 0 & \text{if } T \geq 270.17\,\mathrm{K} \end{cases} \tag{2.53}$$

with the parameter $\alpha_{\mathrm{cf}} = 1.55 \cdot 10^{-3}$, the collection efficiency $E_{\mathrm{cf}} = 5.0 \cdot 10^{-3}$, and the concentration of natural contact ice nuclei active at $-4°\mathrm{C}$ at sea level $N_{\mathrm{cf},0} = 2.0 \cdot 10^5$ (Doms et al., 2011). Again, the units can be found in Doms et al. (2011).

2.7 Validation

Previous versions of MITRAS are confirmed to represent well the main atmospheric features within an urban boundary layer. MITRAS v1.0 has been validated in comparison to wind tunnel data (Schlünzen et al., 2003; Grawe et al., 2013). MITRAS v2.0 (Salim et al., 2018) has been evaluated using the VDI guideline for microscale, obstacle-resolving models (Grawe et al., 2015). The model extensions concerning radiation in MITRAS v3.0 are described and validated in Fischereit (2018). As most parts of the extended model are already validated (e.g. Ferner et al., 2023, Section 3.4), an assessment of the plausibility of the model results is performed here. Furthermore, tests in comparison to measured data are challenging, because in a model domain of this size hardly any high-resolution in-situ data are available.

For a more in depth assessment of the winter parameterisations introduced in the current paper, model results achieved by using different model versions are compared using "to be expected outcomes" for an assessment. The set-ups of the simulations and corresponding model version number are listed in Tab. 2.1. MITRAS v3.0 is considered to be the initial version (index "init" in name). MITRAS v3.1 (index "wr") includes neglecting the influence of terrain steepness on horizontal diffusion terms (Section 2.4.1), changing the structure of all scalar obstacle surface variables and introduction of boundary conditions at obstacle surfaces for water content variables (Section 2.4.2), and sedimentation of rain on roofs (Section

Table 2.1: Set-up for simulations with different initial surface temperatures T (W for warm, C for cold, H for hot), cloud water contents q_1^{2c}, and development stage of the model. For details see text.

Name	T [K]	q_1^{2c}	version	extensions included	comment
Winit	280	none	3.0		
Wwr	280	profile	3.1	Horizontal diffusion terrain steepness neglected; changed array structure; water contents at building surfaces; sedimentation on roofs	no parallelisation
Wwr_np	280	profile	3.1		
Wwr_noprecip	280	none	3.1		no precipitation
Cwr	272	profile	3.1		
Hwr	288	profile	3.1		
Cice	272	profile	3.3	v3.1; snow cover; one-category ice scheme	
Wice	280	profile	3.3		
Hice	288	profile	3.3		

2.6.1). In a previous study, MITRAS v3.1 has been tested with focus on the reliability of the rain processes in comparison with in-situ rain radar data (Ferner et al., 2023, Section 3.4). MITRAS v3.3 includes the winter precipitation scheme (use denoted by index "ice" in Tab. 2.1) described in Sects. 2.5 and 2.6.

2.7.1 Model set-up

All simulations are performed for the same model domain (Section 2.7.2). For the plausibility tests in Section 2.7.4, simulations with three different initial surface level temperatures ("C" for cold, "W" for warm, "H" for hot in Tab. 2.1) are performed. In Fig. 2.7, the initial temperature profiles are provided in black. For the profile, a potential temperature gradient of $0.001\,\mathrm{K\,m^{-1}}$ is assumed. For all simulations except Winit and Wwr_noprecip, nonzero initial cloud water contents (blue solid line in Fig. 2.7) are prescribed which lead to heavy precipitation. The initial surface level pressure is 990 hPa, the initial wind at 150 m above ground is from west ($2\,\mathrm{m\,s^{-1}}$). Due to Coriolis force effects, the wind direction at 10 m height is south west with a friction reduced wind speed of $1.2\,\mathrm{m\,s^{-1}}$. The initial relative humidity is set to 60 % at ground and reduces to 30 % at the top of the model domain (5 km) yielding

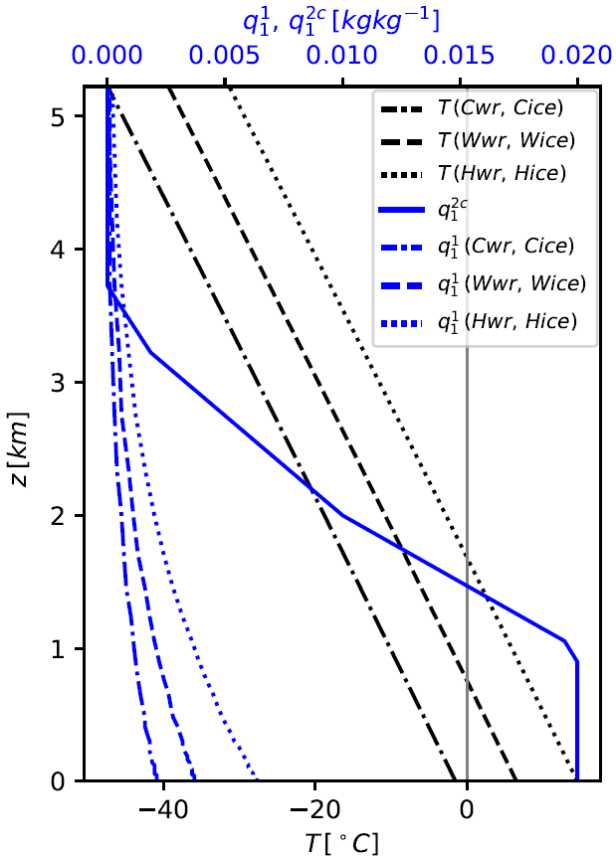

Figure 2.7: Initial temperature (black), specific humidity q_1^1 and cloud water content q_1^{2c} (both blue) vertical profiles for cold (dashdotted line), warm (dashed line), and hot cases (dotted line). The cloud water content profile (solid line) is identical for all cases, that include precipitation. The grey line denotes the freezing point.

the specific humidity profiles in Fig. 2.7 (dash-dotted, dashed, dotted blue lines).

The plausibility tests are performed using hit rates (Section 2.7.3). To determine them, allowed uncertainty ranges have to be found for the meteorological variables. This is based on published methods to asses obstacle-resolving model performance and is done for variables by comparing model results with and without parallelisation (Wwr and Wwr_np in Tab. 2.1).

2.7.2 Model domain

The model domain is small to ensure a fast integration. However, it includes orography, slanted roofs, obstacle corners and different surface cover classes to assess, if the model can represent the different features for a realistic urban area. The domain extends 240 m × 210 m

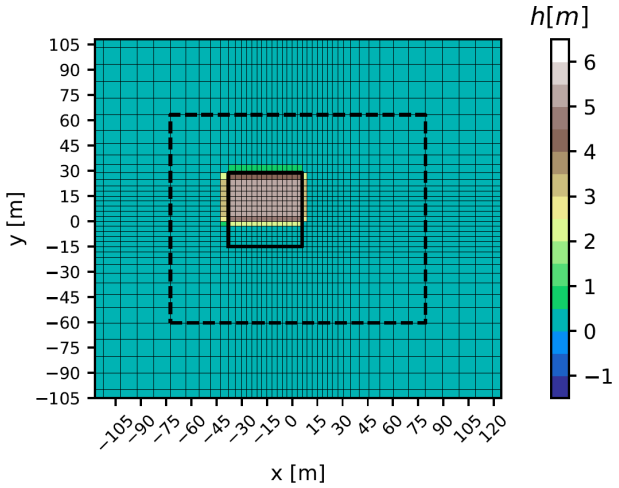

Figure 2.8: Orography height h (shaded) of model domain. The solid line denotes the contour of the building and the black dashed line the model domain taken into account in the result analyses. Thin lines illustrate the horizontal grid.

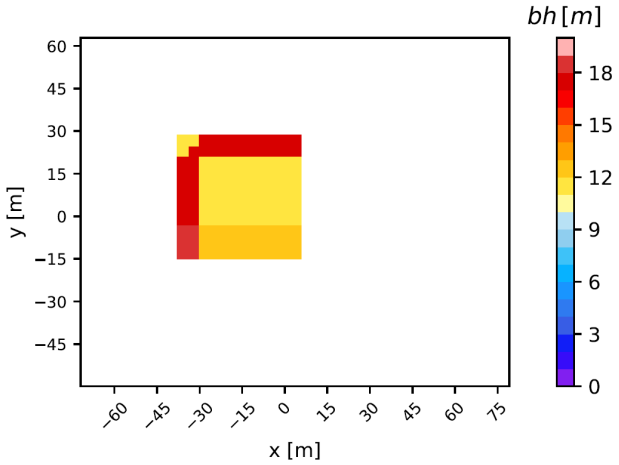

Figure 2.9: Roof height bh.

horizontally and 6400 m vertically with an equidistant area of 3 m resolution in the middle (Fig. 2.8). The grid increases towards the lateral boundaries to a maximum horizontal resolution of 10 m. The maximum vertical resolution of 500 m is achieved at 3 km above ground. Typically, domains of obstacle-resolving models extend only few hundred metres vertically (Geletič et al., 2022; Grawe et al., 2013). However, with interest in cloud and precipitation development in the influence of a building, the upper level is chosen high enough to ensure a vertical extension of clouds is not hindered by a too low model top. Grid sizes

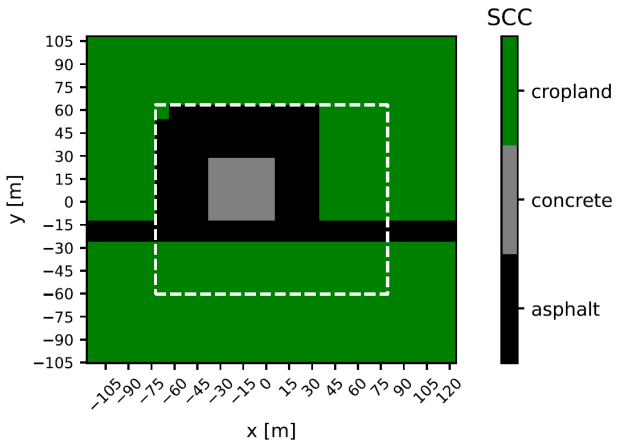

Figure 2.10: Surface cover classes. The dashed line denotes the model domain taken into account in the result analyses.

increase in horizontal as well as vertical direction by a factor of 1.175. The equidistant area ranges from −28 m to 26 m in the x-direction and −16 to 18 m in the y-direction and from the ground up to 32 m.

A single building with roof heights at 15 m and 10 m, and a size of 45 m by 45 m (Fig. 2.9) including edges and slanted surfaces is placed on top a small mound. This setup resembles a terp, which is a North European form of housing, where an artificial mound protects the building from flooding. At the boundaries is cropland. The pavement and the streets are made of asphalt. At obstacles, the surface cover class is concrete (Fig. 2.10).

The simulations start for 7:30 and finish for 8:32. Within this time span, a precipitation event takes place and the sun rises. The focus area of the analyses lies in the centre of the domain (dashed lines in Figs. 2.8 and 2.10).

2.7.3 Derivation of model uncertainty values

The assessment, whether model results are identical or different is based on a method described in VDI (2017) which uses hit rates. Hit rates have been applied in the past for assessing microscale models (e.g. Eichhorn and Kniffka, 2010; Franke et al., 2012; Grawe et al., 2013) as well as for other model scales (e.g. weather forecast (Cox et al., 1998),

mesoscale air quality and meteorology models (Schlünzen and Sokhi, 2008)). The hit rate q is defined as:

$$q = \frac{1}{N} \sum_{i=1}^{N} n_i \tag{2.54}$$

with N being the total number of compared values and n_i equal 1 (hit) or 0 (fail) depending on the deviation of model results and comparison data:

$$n_i = \begin{cases} 1 & \text{if } \left| \frac{Pd_i - O_i}{O_i} \right| \leq D \text{ or } |Pd_i - O_i| \leq W \\ 0 & \text{else.} \end{cases} \tag{2.55}$$

For every atmospheric grid cell at location i, the wind speed is assessed per component (u, v, w). The comparison results in a hit ($n_i = 1$), if the relative deviation does not exceed the threshold value, D, or the absolute deviation remains below the corresponding threshold W. When comparing model results to observational data, Pd_i denotes the predicted and O_i the observed values. In the present study, results of different model versions are compared. Pd_i denotes the newer model version and O_i the older version. Following VDI (2017) and WMO (2023a), a hit rate of $q \geq 95\,\%$ between two simulation results are considered similar. There, the threshold values for absolute and relative deviations, W and D, for the wind speed components speeds are $W_{\mathrm{VDI}} = 0.01\,\mathrm{m\,s^{-1}}$ and $D_{\mathrm{VDI}} = 0.05$. Wind speed components are normalised with the reference wind speed U_{ref} for the test cases. In the current study, the initial wind speed of $2\,\mathrm{m\,s^{-1}}$ is used as reference wind speed. As non-normalised values are compared, W has to be adjusted to $W = W_{\mathrm{VDI}} \cdot U_{\mathrm{ref}} = 0.02\,\mathrm{m\,s^{-1}}$ (Tab. 2.2). For the relative deviation, D_{VDI} is assumed for D for each of the wind speed components (Tab. 2.2). It should be noted that these values are about a factor of 10 smaller than the required measurement uncertainties for wind speed given in WMO (2023a).

In this study, not only the results for the components of the wind vector but also the results

Table 2.2: Thresholds for the absolute (W) and relative deviation (D) for hit rate calculation (q) for wind speed components u, v, w, temperature T, net long and short wave radiation LW_{net} and SW_{net}, and precipitation amount P on ground. For details on their derivation see text.

	u	v	w	T	LW_{net}	SW_{net}	P
W	$0.02\,\text{ms}^{-1}$	$0.02\,\text{ms}^{-1}$	$0.02\,\text{ms}^{-1}$	0.05 K	$0.5\,\text{Wm}^{-2}$	$0.5\,\text{Wm}^{-2}$	0.001 mm
D [%]	5	5	5	0.02	0.5	0.2	1

for temperature, long and short wave radiation, and precipitation amount on ground P are assessed. The W and D values for these meteorological variables are derived by comparing the results of MITRAS v3.0 with one running in parallel processing mode and the other one with single processor use (with and without parallelisation; Wwr and Wwr_np) after one hour of simulation. This measure is taken, since the same model might yield different results depending on compilers, installed packages, and hardware. Therefore, hit rates below 100 % can occur (e.g. 98 % for v, Tab. 2.3). As a hit rate above 95 % means the results lie within the required accuracy, Wwr and Wwr_np can be considered identical (Tab. 2.3).

With computational accuracy a strict criterion is applied for temperature, radiation, and precipitation. The resulting W and D values are consistent with the allowed uncertainty values for the wind speed components, as they also are about a factor of 10 smaller than given in WMO (2023a). For example, the achievable uncertainty for temperature suggested by WMO (2023a) is 0.2 K and here 0.05 K is chosen. For long and short wave radiation $1/10^{\text{th}}$ of the values for direct solar radiation ($4 - 6\,\text{W}\,\text{m}^{-2}$ WMO, 2023a) is used. The allowed absolute deviation of 0.001 mm for precipitation is well below the accuracy of commonly used rain gauges (0.1 mm, WMO, 2023a). This strict value is chosen because precipitation is the target value of our model extensions. Low hit rates give the impression of larger differences. It should be noted that the dependency of the hit rate on the allowed deviations is a shortcoming of this validation metric as discussed in Franke et al. (2012). On the other hand, the comparison of results of different model versions should lead to very similar

results (e.g. with/ without parallelisation, code extensions used with values of zero for the new variables), while extensions of a model with new or changed process descriptions should provide different model results.

Table 2.3: Hit rates q in percent of wind components (u, v, w), temperature (T), net surface long wave and short wave radiation (LW_{net}, SW_{net}), and precipitation amount (P) on ground after 1 hour simulation time.

Cases	u	v	w	T	LW_{net}	SW_{net}	P
Wwr - Wwr_np	100	98	100	100	100	100	100
Wwr_noprecip - Winit	93	83	92	95	100	100	-
Wwr - Wwr_noprecip	28	4	39	0	0	0	0
Cice - Cwr	39	10	33	5	3	0	100
Hice - Hwr	9	4	29	4	0	0	48
Wice - Wwr	40	7	36	4	0	0	60

2.7.4 Model plausibility and functionality

Influences of the modifications of the diffusion

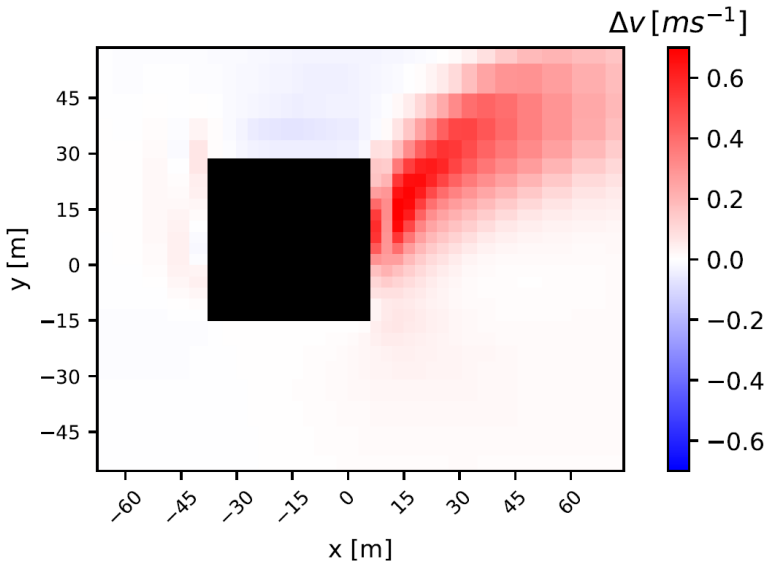

Figure 2.11: Difference of v-wind component Δv of Wwr_noprecip and Winit at 1.5 m height.

The comparison of the results from simulations using MITRAS v3.1 (Wwr_noprecip) with simulations using MITRAS v3.0 (Winit) for dry atmospheric conditions would show any

influences of changes due to the calculation of the horizontal diffusion of scalars (Section 2.4.1) and the modified structure for all scalar quantities at obstacle surfaces (Section 2.4.2). The changes of the model physics by the modifications in horizontal diffusion are small, but due to the strictness of the required accuracy, a good agreement with hit rates of 95 % is not expected for the whole domain. As the effects of slopes are largest close to the ground surface, the largest discrepancies are to be expected there. Not surprisingly, hit rates are below 95 % for the wind speed components (Tab. 2.3). The results for temperature, long and short wave radiation can be considered identical. The lowest hit rate in this comparison of 83 % is found for the lateral wind component v. Misses are only found in grid cells near the ground (Fig. 2.11), where the terrain steepness of the terrain-following coordinate system has the most effect, which is plausible.

Influences of cloud formation

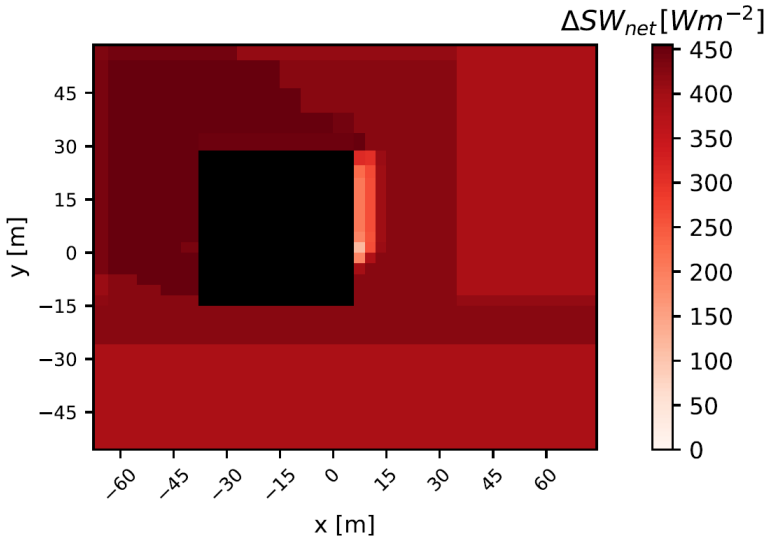

Figure 2.12: Difference of net surface short wave radiation ΔSW_{net} of Wwr and Wwr_noprecip.

The influence of the presence of atmospheric liquid water on the radiation is included in MITRAS v3.1. When liquid water is present, shading by clouds is considered using the two-stream approach instead of the vertically integrated radiation approach (Section 2.3.2). This

leads to different net surface radiations. Comparing simulations with and without precipitation (Wwr and Wwr_noprecip) therefore reveals, not surprisingly, profound differences with hit rates below 39 % for all meteorological variables with the flow field being more similar than the temperature, short and long wave radiation and precipitation (Tab. 2.3). Without precipitation, the shadow cast by the building and the reflection by the small elevation can be seen very clearly in the net surface short wave radiation (not shown). This effect is not as pronounced when cloud water is present as the cloud blocks the radiation. However, the differences still show the direct shading by building and slope (Fig. 2.12). With and without liquid water, the net surface long wave radiation is negative meaning the net flux is outward. However, the absolute values are larger without liquid water in the atmosphere (not shown) as there is less backscattering and surfaces get warmer. These results confirm Ferner et al. (2023, Chapter 3), where results of MITRAS v3.1 were compared with in-situ measurements and the model has been shown to produce plausible results.

Influences of snow cover

By including snow cover (Section 2.5) in MITRAS v3.3, the homogenising effect of snow cover on the albedo is represented in the model. The snow cover parameterisation is implemented in Cice and the temperature is sufficiently low for snow to reach the ground and remain. Without snow cover, most of the focus area is asphalt (Fig. 2.10) with an albedo of 0.09. Cropland has an albedo of 0.2. Without snow cover (case Cwr), the median of the albedo therefore is 0.09. This can be seen in Fig. 2.13, where box plots of albedo values of cases Cice (grey, MITRAS v3.3) and Cwr (blue, MITRAS v3.1) are shown. For Cwr, the box plots remain the same over time. With snow cover (Case Cice), the median increases with increasing snow cover, while the spread of the albedo data decreases. The albedo does not reach the maximal snow albedo of 0.85 (Section 2.5.5), meaning that underlying soil still slightly shines through.

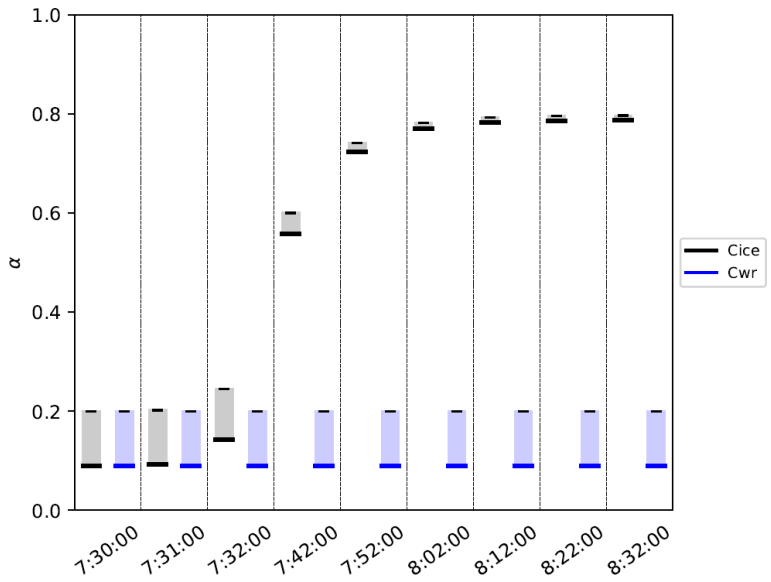

Figure 2.13: Box plots of albedo α for Cice (dark blue) and Cwr (light blue) show the median and the quartiles. The lower thick line denotes the median while the box represents the quartiles.

Influence of temperature on precipitation

The cloud microphysics parameterisation in MITRAS v3.1, which does not include snow (Cwr, Wwr, Hwr), as well as the one-category ice scheme applied in MITRAS v3.3 (Cice, Wice, Hice) are mass conserving. Therefore, the precipitation amounts on ground are expected to be similar after one hour of simulation, as they depend only on the temperature and not on the used model version (Tab. 2.3, hit rate for P 100 % for compared cases Cice and Cwr). For the other meteorological variables, more disagreement with hit rates below 95 % is expected due to the strictness of the required accuracy. Especially for radiation and temperature profound differences are found (Tab. 2.3, hit rates below 5 %). The wind field retains some common features (hit rates up to 39 %). In Fig. 2.14, the spatial mean precipitation amounts on ground over time are presented for rain (dashed lines), snow (dotted lines), and rain + snow (solid lines). As there is no snow in MITRAS v3.1 (Cwr, Wwr, Hwr), the complete precipitation amount is given in dashed lines for these cases, as it equals the rain amount. After half an hour of simulations, the precipitation curves have converged. However, the hit

rates of the precipitation amount for the comparisons of MITRAS v3.3 and v3.1 for "hot" (288 K at surface, Hice and Hwr) and warm (280 K at surface, Wice and Wwr) are below 95 % (Tab. 2.3), meaning, the results do not lie within the required accuracy. When allowing less strict required accuracies based on observational uncertainties following WMO (2023a) ($W = 0.1$ mm, $D = 5$ %), the comparison of precipitation of the different model versions yield hit rates of 100 %. This further underlines the sensitivity of the hit rate to the choice of allowed deviation.

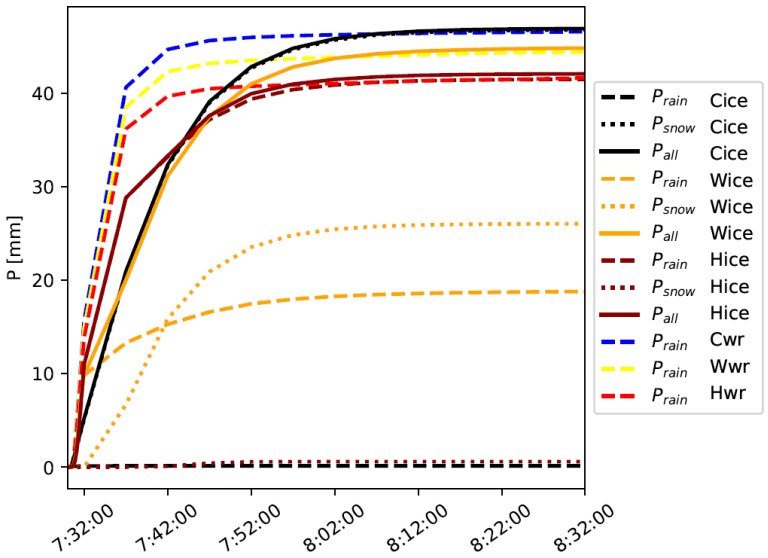

Figure 2.14: Precipitation amounts on ground for Cice (black), Wice (orange), Hice (brown), Cwr (blue), Wwr (yellow), and Hwr (red). Rain is given in dashed lines, snow in dotted lines and rain and snow together are given as solid lines.

The higher the temperature, the more water vapour the atmosphere can carry before saturation is reached resulting in less precipitation amounts. This is well represented in the model (MITRAS v3.1 and MITRAS v3.3). The final precipitation amounts are smaller for higher temperatures (from black and blue lines over yellow to red curves in Fig. 2.14). More of rain and snow water content evaporates or sublimates in the sub-saturated areas below the cloud than it would in colder cases. Simultaneously, the production of cloud water content by condensation is reduced. In this study, water vapour is prescribed using the relative humidity leading to temperature dependent specific humidity profiles (Fig. 2.7). This does

not represent that more precipitation is expected in a warming climate (e.g. Purr et al., 2021).

Influence of one-category ice scheme

The level of detail is increased in MITRAS v3.3 by extending the model with a one-category ice scheme (Section 2.6) improving the representation of precipitation in winter. During the first minutes of the simulation, the amount of precipitation on ground increases faster with time if only warm precipitation is considered (MITRAS v3.1, dashed lines in Fig. 2.14) than when also considering the ice phase (MITRAS v3.3, solid lines). In the warm rain Kessler-scheme, the sedimentation of small rain drops is overestimated leading to the calculation of too much precipitation during the process of rain formation (Schlünzen et al., 2018a). This effect is reduced with the one-category ice scheme parameterisation, because precipitation develops slower with this new parameterisation. These changes have consequences on radiation, temperature and wind field, which explains the low hit rates (Tab. 2.3).

2.8 Summary and Conclusions

The microscale and obstacle-resolving model MITRAS was extended by modifying the diffusion of scalars (Section 2.4.1) as well as including boundary conditions for cloud and rain water content at obstacle surfaces (Section 2.4.2) and a snow cover scheme (Section 2.5). The cloud microphysics scheme for warm clouds was extended with a one-category ice scheme (Section 2.6). This makes MITRAS the first obstacle-resolving atmospheric model, that includes precipitating snow.

Previous model versions of MITRAS are confirmed to represent well the main features of an urban boundary layer (Schlünzen et al., 2003; Grawe et al., 2013, 2015; Fischereit, 2018). The performance of the warm rain scheme and the newly introduced boundary conditions (v3.1) has been validated by Ferner et al. (2023, Section 3.4). The parameterisations for snow cover and the one-category ice scheme have already been applied in mesoscale models

(Boettcher, 2017; Doms et al., 2011). The modifications of the parameterisations for the characteristics of a microscale and obstacle-resolving model are validated here by testing for plausibility (Section 2.7) by comparing model results of different model versions (v3.0, v3.1, v3.3). The model features presented in this paper are included in MITRAS v4.0 as are features not relevant to this study (e.g. v3.2, Badeke et al., 2021).

For the plausibility tests, simulations were compared based on a procedure described in VDI (2017) for obstacle-resolving models, where hit rates are calculated for the wind speed components. In our study, additional hit rates for temperature, radiation, and precipitation were determined on the basis of computational accuracy. The resulting required deviations are 0.05 K (0.02 %) for temperature, 0.5 Wm^{-2} (0.5 %) for long wave radiation, 0.5 Wm^{-2} (0.2 %) for short wave radiation, and 0.001 mm (1 %) for precipitation.

Comparisons of different model versions reveal that the model produces plausible results. Neglecting terrain-steepness in the diffusion calculation for scalars in MITRAS v3.1 and extending the cloud microphysics scheme in MITRAS v3.3 causes expected differences. The plausibility tests also reveal that taking precipitation into account in a microscale obstacle-resolving model is crucial due to the profound influence of clouds on radiation. Even though state-of-the-art bulk cloud microphysics parameterisations are more complex than the one-category ice scheme applied in MITRAS (Khain et al., 2015), an improvement compared to the previously applied warm rain scheme (Köhler, 1990) has been shown. The overestimation of precipitation during the process of rain formation (Schlünzen et al., 2018a) is reduced. The homogenising effect of snow on the albedo is plausibly reproduced.

In order to increase the level of detail of MITRAS' winter parameterisation, the effects of snow on the roof's albedo or roughness length should be considered. Moreover, the effects of different isolation properties of buildings should be included for instance to study anthropogenic heat emissions on warming and snow melting as well as on the indoor building temperature. For the analyses of frost heterogeneities e.g. on roads and walkways, the

inclusion of freezing rain or refreezing snow would be useful, even though it is already possible to derive possible locations of frost from results of the extended model. Refining the crude representation of winter services would lead to further improvements.

The extended model provides the opportunity to perform more realistic simulations of a winter event, where precipitation and obstacles are explicitly resolved. The effects of snow cover and precipitation especially on radiation are better represented. The extended model allows first estimates on influence of different city characteristics on snow heterogeneities. In the future, this information can be used for analyses on frost heterogeneities or human comfort. A sensitivity study extended for an urban neighbourhood is a next step to investigate, how obstacles influence the falling of snow and urban temperature development.

3 Modelling the heterogeneity of rain in an urban neighbourhood with an obstacle-resolving Model

Preface

This chapter is published as:

Ferner, K. S. and M. Boettcher and K. H. Schlünzen (2023): Modelling the heterogeneity of rain in an urban neighbourhood with an obstacle-resolving model. *Meteorologische Zeitschrift*, 32, 67-81, https://doi.org/10.1127/METZ/2022/1149

The full manuscript of the published paper is included in this chapter. Layout and numbering within the manuscript were adopted to fit this thesis. The prefix 'RH_' (**R**ain **H**eterogeneity) was added to the simulation names in the text (not in the figures) to distinguish them from the simulation names in Chapter 4. All references are combined in References. Supporting information submitted with this manuscript can be found in Appendix B. Symbols are adjusted and included in the List of Symbols. The simulations are published at the World Data Center for Climate (WDCC): Ferner et al. (2024).

K. H. Schlünzen has contributed to the conceptualisation and contributed some ideas for the analysis. M. Boettcher developed the radar forcing, performed the evaluation and wrote Sections 3.3.4 and 3.4. All authors contributed to the discussion of the results.

3.1 Abstract

Building induced winds change the falling of rain, leading to heterogeneous patterns of rain on ground and on building surfaces. These rain heterogeneities also occur in small urban scales like an urban neighbourhood, which covers an area of a few km^2. For the investigation of rain heterogeneities within an urban neighbourhood the microscale, obstacle-resolving model MITRAS is used, which employs a microphysics parameterisation for cloud and rain processes. MITRAS has been extended by boundary conditions for cloud and rain water at building

surfaces. An initialisation with radar data is implemented and the model output is successfully compared with in-situ precipitation data. Simulations for an urban area are performed using different initial wind speeds, rain amounts, wind directions, and domain configurations. For the rain heterogeneity within this urban neighbourhood, the processes between buildings are found to be of small influence for the rain already falling. However, exchange processes from the canopy to the air above are found to influence the above-canopy rain pattern. The influence of the meteorological situation and the city's geometry on the wind field within and above the buildings are relevant to realistically represent a rain event and to create high-resolution precipitation data.

3.2 Introduction

Urbanisation locally modifies the regional climate: an urban climate develops. For instance, urban areas impact the rainfall both within and in the vicinity of a city (Zhang et al., 2022; Liu and Niyogi, 2019; Freitag et al., 2018; Shepherd, 2005). The exact processes causing rain heterogeneities and their synergetic interactions, however, are not well understood.

Within the city, the average wind speed is reduced, while gustiness is increased (Wiesner et al., 2018; Schlünzen et al., 2018c). Buildings induce vertical winds, which affect the falling of rain droplets. Heterogeneous rain patterns on ground and on building surfaces also in small urban scales like an urban neighbourhood (order of magnitude of $1\,\mathrm{km}^2$) are expected.

For measuring small-scale precipitation heterogeneities, rain gauge networks and high-resolution weather radars are commonly used. However, capturing the spatial rain variability on ground using point measurements even for small domains (e.g. $500\,\mathrm{m} \times 500\,\mathrm{m}$) is fraught with uncertainty (Jensen and Pedersen, 2005; Pedersen et al., 2010; Terink et al., 2018). High-resolution precipitation data in cities is scarce and often insufficient. In their review on urban rainfall variabilities, Cristiano et al. (2017) list the specific challenges in measuring rain in urban areas. In densely urbanised areas it is difficult to find representative locations

for rain gauges (WMO, 2008). Weather radars seem to be the alternative, but they require an unobstructed view over the surfaces in the domain, which is not given in cities due to the buildings. The scarcity of high-resolution data is a source of errors in the urban runoff estimation (Niemczynowicz, 1988).

High-resolution precipitation data can also be obtained by numerical modelling. Atmospheric models include various physical processes for a realistic representation of the urban boundary layer. For instance, the obstacle-resolving high-resolution urban climate model PALM-4U, which is based on PALM (Maronga et al., 2020), does not include precipitation, yet (Maronga et al., 2019). The Regional Atmospheric Modeling System (RAMS) (Pielke et al., 1992) includes a parameterisation for cloud processes and has also been used for flow simulations around obstacles (Castelli and Reisin, 2010), but no investigations of the heterogeneity of rain in urban neighbourhoods were performed.

Another process relevant in urban areas is horizontally advected rain, that can hit building walls. This so-called wind-driven rain is mainly investigated in building science focusing on single buildings and vertical surfaces. A review on wind-driven rain research is given by Blocken and Carmeliet (2004). Usually a steady-state 3D wind flow pattern is assumed. The trajectories of the rain drops are then calculated using, for example, Lagrangian particle tracking (Blocken and Carmeliet, 2004) or an Eulerian multiphase model (Kubilay et al., 2013). Studies on wind-driven rain usually focus on the effects of humidity on building facades. For example, Coutu et al. (2013) investigated the catch-ratio of water on building facades including the effects of surrounding buildings. The influence of wind-driven rain on thermal comfort within an isolated three-dimensional street canyon has been investigated as well (Kubilay et al., 2018).

Meteorological parameters and the urban morphology are expected to have an influence on the rain heterogeneity on ground and on roofs. However, for determining the heterogeneity of rain patterns it is unclear how detailed a model simulation needs to be. In this study this

question will be answered by focusing on the role of orography and obstacle distribution, and the influences of wind speed, rain amount, and wind direction.

The microscale, obstacle-resolving transport and stream model MITRAS (Schlünzen et al., 2003; Salim et al., 2018) is applied to analyse the rain heterogeneity in a small urban setting. The model calculates wind, temperature, humidity fields, cloud and rain water, and the transport of tracers within the urban boundary layer. It is part of the M-SYS model system (Trukenmüller et al., 2004; Schatzmann et al., 2006).

A description of the model, the newly introduced boundary conditions for rain on building surfaces, as well as of the radar forcing are given in Section 3.3. Grawe et al. (2013) have shown that wind fields in urban areas are well simulated by MITRAS when compared with wind tunnel data. Thus, the validation in this study focuses on the performance of the model with respect to rain processes. For the validation in Section 3.4, model results are compared with in-situ data at the boundary layer weather mast in Hamburg (Lange, 2021).

For the sensitivity studies in Section 3.5, the city centre of Hamburg (Germany) has been chosen, since for this neighbourhood a detailed building mask (Salim et al., 2015; Müller and Seyfert, 2000) exists. Simulations have been performed for different meteorological situations (initial wind speeds, rain amounts, wind directions), and topographies (with and without orography and buildings). Finally, conclusions and outlook will be given in Section 3.6.

3.3 Method

3.3.1 Numerical Model

The microscale, obstacle-resolving transport and stream model MITRAS is a three-dimensional, non-hydrostatic, prognostic, numerical model. MITRAS version 1 has been validated in comparison to wind tunnel data (Schlünzen et al., 2003; Grawe et al., 2013). Version 2 has been evaluated using the VDI guideline for microscale, obstacle-resolving models (Grawe et al.,

2015). It is used to simulate wind, temperature, and humidity as well as pollutant dispersion within the obstacle layer dependent on time. Since the model is well documented (Salim et al., 2018; Schlünzen et al., 2018a), only a brief description is provided here.

The model solves the Navier-Stokes equations, the continuity equation and the conservation equation for scalar quantities in flux form. A terrain-following coordinate system ($\dot{x}^1$, $\dot{x}^2$, $\dot{x}^3$) is applied. The basic equations are filtered using Reynolds averaging.

Subgrid-scale turbulent fluxes are parameterised using a first order closure. Due to the coordinate transformation, the horizontal fluxes also depend on terrain steepness and the vertical gradients of the average values; these terms are neglected due to the small slopes in the considered terrain. The resulting subgrid-scale turbulent fluxes are provided here for the rain water content q_1^{2r} in terrain-following coordinates:

$$-\rho_0\overline{u'q_1^{2r\prime}} = \rho_0 K_{\text{hor}}\left(\frac{\partial\overline{q_1^{2r}}}{\partial\dot{x}^1}\frac{\partial\dot{x}^1}{\partial x}\right) \tag{3.1}$$

$$-\rho_0\overline{v'q_1^{2r\prime}} = \rho_0 K_{\text{hor}}\left(\frac{\partial\overline{q_1^{2r}}}{\partial\dot{x}^2}\frac{\partial\dot{x}^2}{\partial y}\right) \tag{3.2}$$

$$-\rho_0\overline{w'q_1^{2r\prime}} = \rho_0 K_{\text{ver}}\left(\frac{\partial\overline{q_1^{2r}}}{\partial\dot{x}^3}\frac{\partial\dot{x}^3}{\partial z}\right) \tag{3.3}$$

with the atmospheric density ρ_0, the wind velocities (u', v', w'), the horizontal (K_{hor}) and vertical (K_{ver}) exchange coefficients, and the Cartesian coordinates (x, y, z). The exchange coefficients are related to the turbulent exchange coefficients for momentum. For the simulations, the Prandtl-Kolmogorov closure (López, 2002; Salim et al., 2018) is used.

The equations are numerically solved on an Arakawa C grid (Arakawa and Lamb, 1977). Scalar quantities such as temperature or cloud and rain water content are defined at grid cell centres (scalar points), whereas the u-wind is defined at the x-boundaries of the grid cell, the v-wind at the y-boundaries, and the w-wind at the vertical (z) boundaries; these are the vector points. Obstacle surfaces are positioned at vector grid points.

3.3.2 Cloud Microphysics

For MITRAS, the same parameterisations for cloud microphysical processes as in its sister model METRAS (Köhler, 1990; Schlünzen et al., 2018a) are used. The parameterisation has been extended by boundary conditions for cloud and rain water at obstacle surfaces.

A Kessler type parameterisation of cloud microphysics allows the simulation of clouds and rain. Atmospheric liquid water droplets are distinguished by their droplet size. Drops with a mean droplet radius of about 10 μm are considered cloud water drops, and drops with a mean radius of about 100 μm are defined as rain water. The separation radius is 40 μm (Doms, 1985).

The Kessler scheme includes condensation of water vapour to cloud water, evaporation of cloud water to water vapour, autoconversion of cloud water to rain water by collision of cloud droplets, conversion of cloud water to rain water by collection of cloud droplets (accretion), sedimentation of rain water, and evaporation of falling rain drops in sub-saturated layers below clouds. Rain drop growth by condensation and sedimentation of cloud droplets are neglected.

For the sedimentation of rain water in the model the terminal velocity

$$v_{\mathrm{TR}} = 68.81 \cdot \sqrt{\frac{\rho_{\mathrm{ref}}}{\rho_0}} \cdot \left(\rho_0 \cdot q_1^{2\mathrm{r}} \cdot 10^{-3}\right)^{0.1905} \tag{3.4}$$

(Köhler, 1990; Schlünzen et al., 2018a) is chosen, which takes the Marshall-Palmer size distribution of rain drops (Marshall and Palmer, 1948) into account and produces values, that fit the expected fall speeds of rain drops. Eq. (3.4) includes the correction factor $\sqrt{\frac{\rho_{\mathrm{ref}}}{\rho_0}}$, that accounts for the smaller atmospheric density at higher altitudes. $\rho_{\mathrm{ref}} = 1.29\,\mathrm{kgm}^{-3}$ denotes the reference atmospheric density. The factor of 10^{-3} is due to the conversion into SI-units.

The change in rain water content in a single grid cell due to sedimentation is determined as difference of the rain water flux entering and leaving the grid cell through its vertical

boundaries. It is given by

$$\Delta q_1^{2r} = \frac{\Delta t}{\rho_0} \cdot \frac{\partial}{\partial z} \left(v_{TR} \cdot \rho_0 \cdot q_1^{2r} \right) \tag{3.5}$$

with the time step Δt (Köhler, 1990).

3.3.3 Boundary Conditions at Obstacles

Obstacles are simulated by assuming impermeable grid cells at the building position. 3D fields of weighting factors contain the information whether a grid cell lies in the atmosphere or in a building. Additional weighting factors are used to define whether a grid cell's boundary corresponds to a building surface (Salim et al., 2018).

For falling rain three types of fluxes may occur at each grid cell boundary (building wall or roof): advection, diffusion, and sedimentation. Since the wind is always zero inside of buildings, there is no advection through the walls. Thus, for the advection the same internal boundary conditions were applied as for e.g. wind (Salim et al., 2018).

For the calculation of diffusion for cloud and rain water, buildings have to be taken into account. Therefore, new boundary conditions at building surfaces needed to be introduced. These boundary conditions have to also consider the effects of orography created by the terrain-following coordinate system.

It is assumed that cloud and rain water diffusing towards a building wall is removed from the atmosphere. This amount of liquid water is determined by specific subgrid-scale turbulent fluxes. Diffusion is calculated at the grid cell boundaries as shown in Fig. 3.1a with orange arrows (vertical diffusion) and red arrows (horizontal diffusion). As the values in buildings are undefined, it is not feasible to calculate the fluxes at the building surface (black arrows). Instead it is assumed that the surface flux equals the flux at the grid cell boundary in the atmosphere next to the building surface (thick orange and red arrows) and pointing in the same direction (horizontal or vertical). For each direction of the building surface, a direction specific flux is calculated. For a grid cell with two or three adjacent faces, two or three

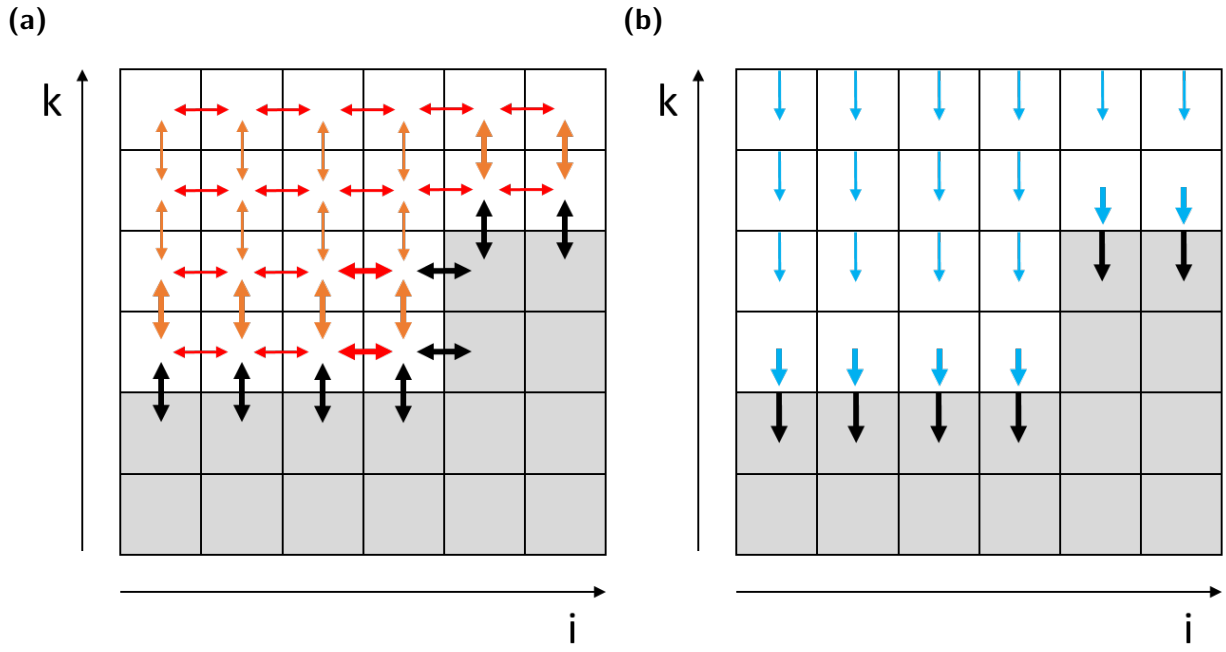

Figure 3.1: Location of a) diffusion and b) sedimentation fluxes in the model grid with building grid cells in grey. The grid cells in x-direction are represented by i and in the vertical direction by k. Orange arrows denote vertical diffusion, red arrows horizontal diffusion, and blue arrows sedimentation. Thick orange, red or blue arrows represent the fluxes, that are calculated instead of the fluxes at building surfaces (black, thick arrows).

different building surface fluxes are required.

For the sedimentation of rain on roofs, rain water reaching the close-to-surface atmospheric grid cell is extracted from the atmosphere and integrated as rain on roofs. This is similar to the collection of rain on ground. The terminal velocity v_{TR} (Eq. 3.4) and thereby the sedimentation flux (Eq. 3.5) are defined at the grid cell boundaries, as shown with thin, blue arrows in Fig. 3.1b. At roofs (black arrows), the sedimentation fluxes are calculated for the roof surface adjacent grid cells at a scalar point (thick, blue arrows). Consequently, the amount of rain on a roof or ground surface during one time step ΔP_{rain} in mm is

$$\Delta P_{rain} = \Delta t \cdot 10^3 \cdot \frac{\rho_0}{\rho_w} \cdot q_1^{2r} \cdot v_{TR} \tag{3.6}$$

with the water density ρ_w.

Rain reaching surfaces is assumed to be absorbed by drains.

3.3.4 Radar Forcing

Depending on wind speed and domain size, an air parcel passes the model domain of a microscale, obstacle-resolving model within a few minutes. The development of cloud and rain processes needs much more time. Therefore, MITRAS is not able to simulate the full development of the cloud and resulting rain within a neighbourhood size model domain although MITRAS includes all the physics needed. MITRAS needs the information about cloud and rain from the outside. For this purpose, idealised rain bands are prescribed as done for the sensitivity studies in Section 3.5 or rain information from a rain radar are used for model forcing as done for evaluation of model results in Section 3.4.

Rain radar data are given for a certain height above ground, depending on the radar location and the distance of the measurement from the radar location. The radar beam spreads with distance from the radar location. Thus, a value of the radar data at a certain place at a certain time gives information about the rain rate within an air volume with horizontal and vertical extend. Numerical models in the microscale range use grids with very small grid volumes of a few m^3 per grid cell. Typically, the grid volume of a microscale model is small compared to the volume of the rain radar beam cell.

For the vertical extend, the rain radar data are applied homogeneously to the corresponding model levels of MITRAS because the vertical structure can not be derived form the radar data. The horizontal resolution of the rain radar data used here is in the order of one-hundred meter while the horizontal grid resolution of a microscale model is in the order of few meters. For the use of radar data in the model MITRAS, the rain radar data are horizontally interpolated to the model grid using the nearest neighbour method.

Rain radar forcing is implemented with the nudging method (Schlünzen et al., 2018a). This means that model results at a specific time and at heights of the radar beam (ψ_f) are a

weighted mean of the calculated model values (ψ_m) and the observation values (ψ_o), in our case the radar values (Eq. 3.7 and Eq. 3.8, Schlünzen et al. (2018a)). To keep the impact of the MITRAS model physics on the results, a complete overwriting of the model values is avoided. The model results at the radar beam heights are calculated for each time step n_t with the time step length Δt. The weighting factor δ is derived from the characteristic time interval of the radar data. The update interval of the radar data is 30 seconds. The weighting factor is assumed as 90 % of the inverse value of 30 seconds, which corresponds to 0.03 per second.

$$\psi_\mathrm{f} = (1-\delta)\,\psi_\mathrm{m} + \delta\psi_o \tag{3.7}$$

$$\psi_\mathrm{f}^{n_t+1} = (1-\delta\Delta t)\,\psi_\mathrm{m}^{n_t+1} + \delta\Delta t\psi_o^{n_t+1} \tag{3.8}$$

3.4 Evaluation of the Model Forcing

3.4.1 Method for evaluation

As mentioned in Section 3.2, there are no sufficiently resolved measurements of rain in an urban neighbourhood available. Therefore, a direct evaluation of the model in an urban neighbourhood using in-situ data is not possible. The remaining solution is a plausibility check, that should be as quantitative as possible. As Grawe et al. (2013) showed, MITRAS fullfils the model evaluation guidline VDI 3783 part 9 (VDI, 2017). MITRAS is able to capture the main features of an urban boundary layer (Grawe et al., 2013). Hence, we focus on the reliability of the rain processes with the newly introduced rain radar forcing (Section 3.3.4).

The Meteorological Institute of the Universität Hamburg provides long-term measurements of meteorological data, including rain rate, at the boundary layer weather mast in Hamburg (Lange, 2021). These data are used for evaluating MITRAS. The same model grid size and model settings are used as for the sensitivity studies in Section 3.5.1. However, the orography, surface cover and the building distribution are adapted to the area around the

boundary layer weather mast (Fig. 3.4a) located in the centre of the model domain.

8 December 2019 is chosen, a day showing rain heterogeneities in space and time for the whole day. Before noon, the rain radar data show a short term rain event hitting the area around the boundary layer weather mast. This event is chosen for evaluation. Before the rain event arrives, the lower atmosphere has relative humidities between 90 % and 95 %. Thus, the physical pcesses of cloud and rain and even evaporation can be tested in this unsaturated atmosphere. The model simulation starts at 11:02:30 LST (10:22:30 UTC) and ends at 11:12:00 LST (10:32:00 UTC). Output is given every 15 seconds.

For the initialization, profiles for wind speed and wind direction, temperature and humidity are used. The initial profiles for the lowest 300 m of the atmosphere are derived from the meteorological measurements at the boundary layer weather mast for model start time. The profiles above 300 m are averaged from the profiles of the closest radiosonde, Bergen-Hohne (DWD meteorological measurement station 00368, roughly 83 km south of the boundary layer weather mast), at 6 UTC and 12 UTC (Deutscher Wetterdienst, 2022b). The surface pressure of 995.662 hPa measured at the boundary layer weather mast is used. For the soil and water temperatures, the soil surface temperature measurement of 8.42 °C at the boundary layer weather mast is used. The lower atmosphere is nearly neutral stratified with these values for soil surface, air temperature and relative humidity. For evaluating the simulated rain amount, the model results are compared with the measurement of the rain gauge installed next to the boundary layer weather mast.

For rain forcing, the data of the x-band radar positioned at the roof of the Meteorological Institute of the Universität Hamburg are used (Burgemeister et al., 2022). The rain radar data with 100 m horizontal grid resolution are horizontally interpolated to the model grid. Vertically, the data cover the model levels 37 to 40, counted from ground (722.3 m to 1286.3 m above ground) depending on the distance from the radar location (Fig. 3.2c). The forcing data are updated every 30 seconds. All other settings are used as described in Section

3.5.1.

3.4.2 Evaluation of simulation results

Driven by the rain radar data, the model simulates a rain event passing the model domain between 11:04:00 LST and 11:08:00 LST. 15 s before, at 11:03:45 LST, no rain water exists in the model domain (Fig. 3.2b). The forcing data from radar measurements show no rain data for this time (Fig. 3.2a). At 11:05:15 LST the rain event passes the model domain centre in the radar forcing data (Fig. 3.2c). The model calculates the rain water content maximum in a slightly lower atmosperic layer than given in the radar forcing data for this time (Fig. 3.2d). At 11:08:00 LST no rain exists in height of the radar beam (Fig. 3.2e), but a remaining signal of the event can be seen in the model results close to the ground (Fig. 3.2f).

The model calculates the physical processes like advection, diffusion, evaporation, condensation and sedimentation for the rain nudged towards the rain radar data. Because of the unsaturated atmosphere below the cloud, in the lowest 500 m, most of the rain water evaporates during sedimentation. Within the whole model simulation, 0.00365 mm of rain reaches the ground (Fig. 3.3b). The rain gauge with a precipitation resolution of 0.1 mm per minute (Lange, 2021) does not show any rain rate during this time (Fig. 3.3a). The very small rain rates simulated are not measurable by the rain gauge. Therefore, the results match within the given accuracy of measurement.

This test case shows that the rain radar forcing and the physical processes calculated in the model fit together. The model result including rain processes with rain radar forcing seems plausible. In a later step a more comprehensive evaluation will be performed.

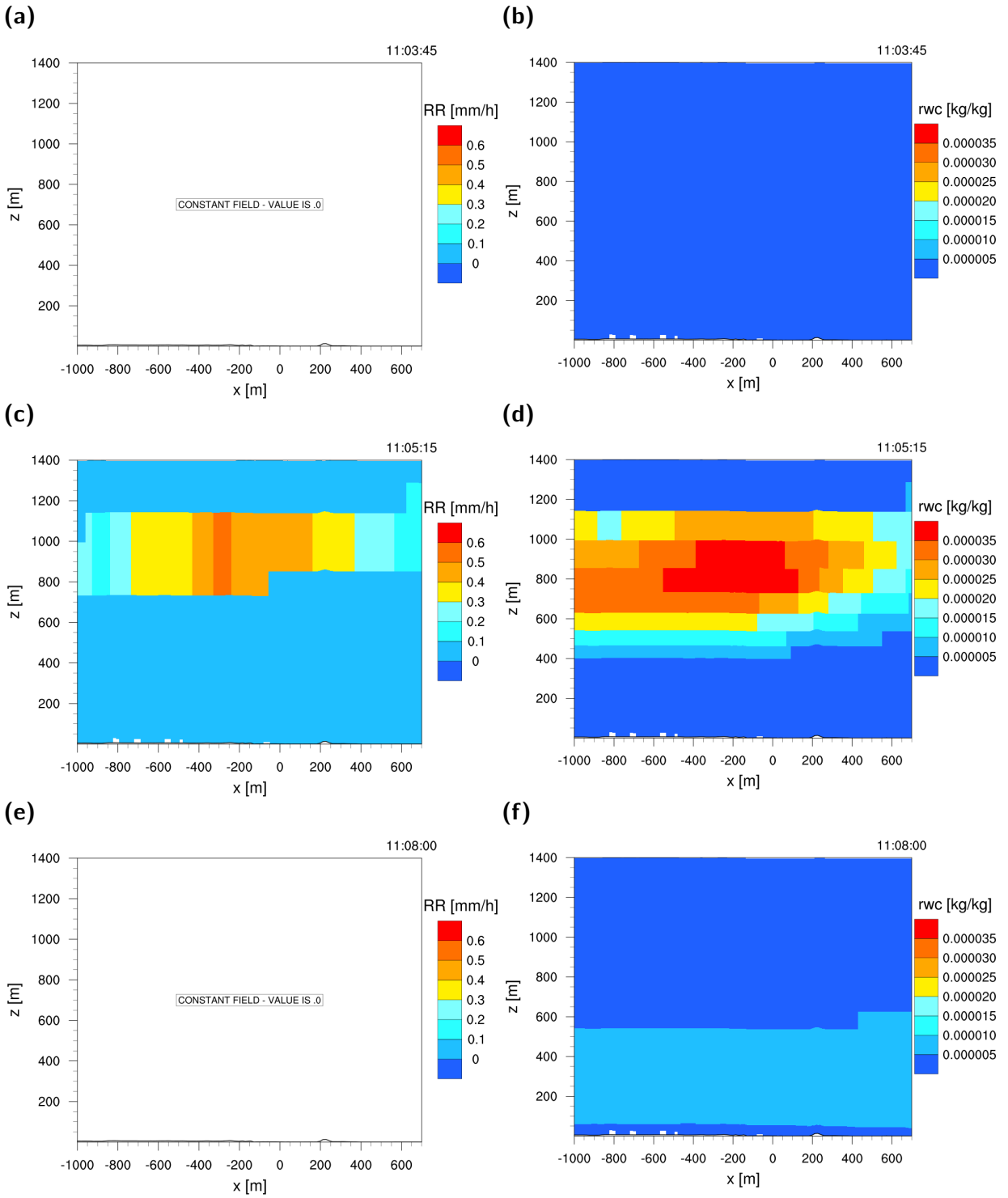

Figure 3.2: Vertical cross section with west to the left at y = 0 m (Fig. 3.4a) of (a,c,e) radar forcing rain rate RR and (b,d,f) rain water content rwc for (a,b) 11:03:45 LST (c,d) 11:05:15 LST and (e,f) 11:08:00 LST.

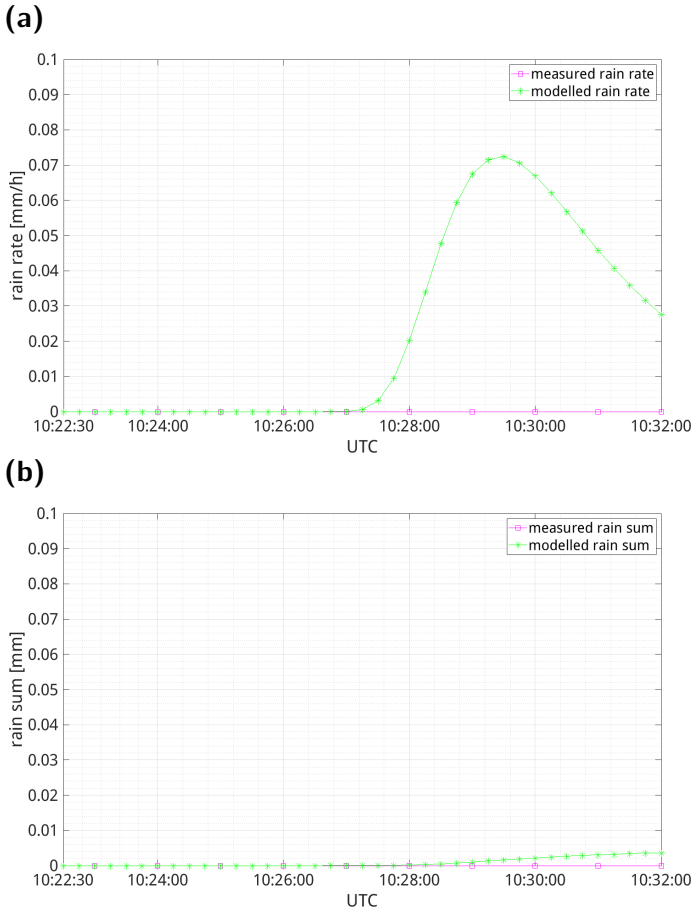

Figure 3.3: Measurements and model results for (a) rain rate and (b) rain sum.

3.5 Sensitivity Tests

3.5.1 Model setup

For the sensitivity studies, the city centre of Hamburg (Germany) was chosen to represent a realistic urban geometry (Fig. 3.4b). The domain is characterised by various street configurations, open spaces, water surfaces, orography and buildings of different heights (Fig. 3.4c).

Simulations for complex domains including the cloud processes are computationally expensive. In order to both include a reasonably high resolution without having an exceedingly high run time of the simulation, a stretched grid is used. In the area of interest obstacles should be resolved with at least three grid cells. For relevant phenomena in street canyons

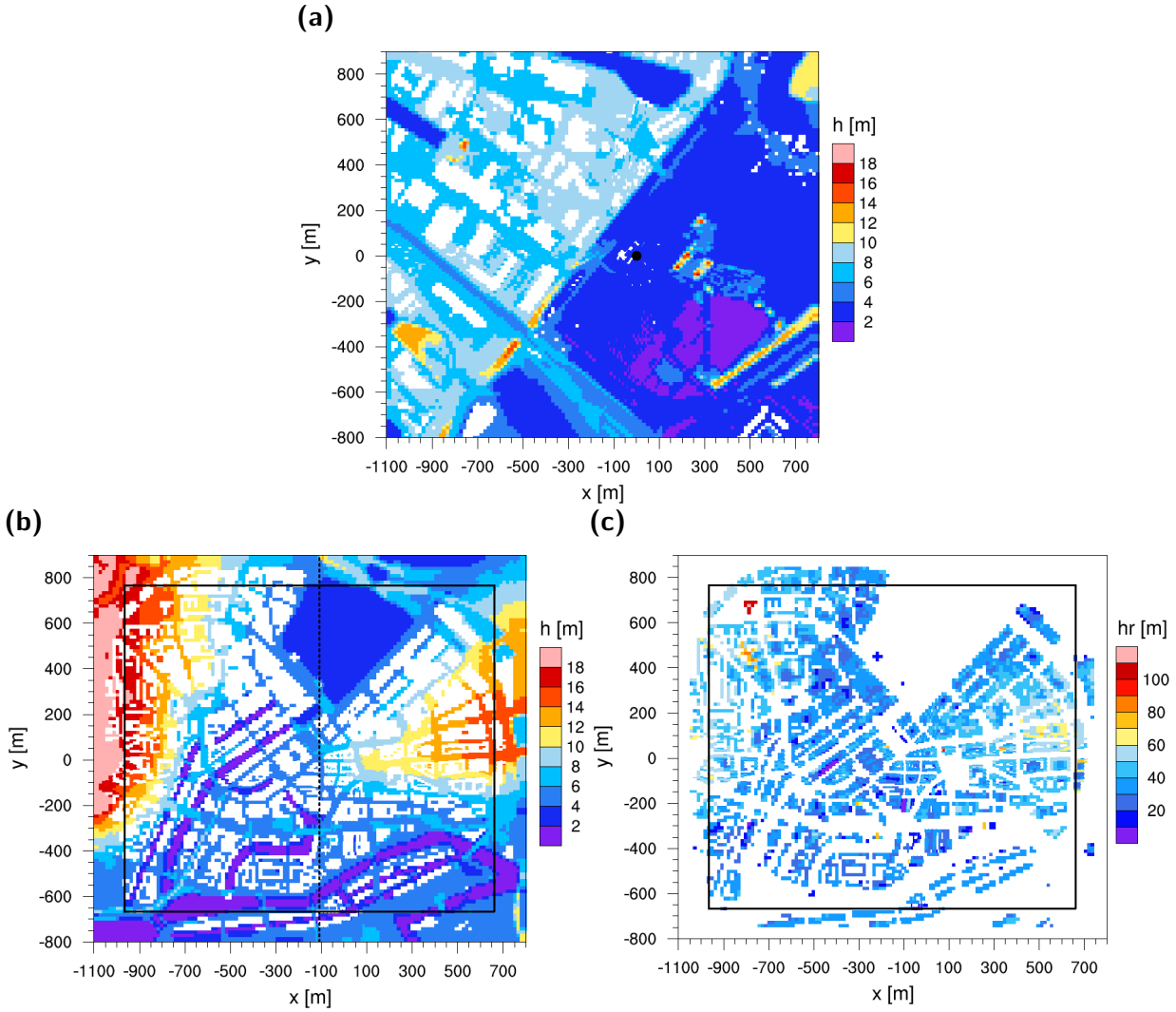

Figure 3.4: Details of the simulation domain (a) around the boundary layer weather mast (the black dot denotes the location of the boundary layer weather mast) and (b) of Hamburg city centre (the dashed line denotes the location of vertical cross sections) with buildings in white and the orography height h in m. The roof top height hr in m is shown in (c). Values outside the black box are not taken into account in the analyses.

at least five grid cells are recommended (VDI, 2017). The domain extends $1.6 \times 1.8\,\mathrm{km}^2$ around Hamburg City Hall. The grid width stretches from 3.5 m with a factor of 1.175 up to horizontally 15 m and vertically 150 m. The highly-resolved, equidistant area extends from $x = y = -100\,\mathrm{m}$ to $x = y = 50\,\mathrm{m}$ and vertically to $z = 50\,\mathrm{m}$. The domain height is 5 km. Close to the model boundaries, results become less trustworthy. Therefore, 10 grid cells at each lateral boundary are removed (black boxes in Figs. 3.4b and 3.4c) in the analyses of the sensitivity studies in Section 3.5.3.

The building data are taken from Salim et al. (2015). They are based on the Digital Terrain Model, the data of the German geo-information system ATKIS (Official Topographic-Cartographic Information System) (Müller and Seyfert, 2000), and on the 3D-urban model data (LoD 2) for building details.

The sensitivity studies are performed with the goal of assessing the influence of the meteorology as well as of the topography on the rain heterogeneity within an urban neighbourhood. Therefore, different meteorological conditions (initial wind speeds, rain amounts, wind directions), as well as different domain configurations were chosen.

Table 3.1: Simulated cases with precipitation after 10 minutes $\frac{P_{\mathrm{rain}}}{10\mathrm{min}}$ on ground, initial wind speed ff_{init}, and initial wind direction dd_{init}.

Case ID	$\frac{P_{\mathrm{rain}}}{10\mathrm{min}}$ [mm]	$\mathrm{ff}_{\mathrm{init}}$ [ms^{-1}]	$\mathrm{dd}_{\mathrm{init}}$ [°]	Notes
RH_LM27	0.5	4	270	
RH_MM27	0.9	4	270	
RH_HM27	1.7	4	270	
RH_ML27	0.9	2	270	
RH_MH27	0.9	6	270	
RH_LL27	0.5	2	270	
RH_HH27	1.7	6	270	
RH_MM23	0.9	4	230	
RH_MM27norog	0.9	4	270	no orography
RH_MM27nobuild	0.9	4	270	no buildings

The simulations cover 10 different cases (Tab. 3.1). The first letter of the case ID denotes the rain amount, the second the wind speed, and the numbers refer to the wind direction. L, M, or H refer to low, average, or high initial values for the respective variable. In case RH_MM27norog the orography was removed and in case RH_MM27nobuild the buildings were removed. An initial air temperature of 1 °C is assumed for all cases at ground. The intial potential temperature gradient is prescribed as $0.001\,\mathrm{Km}^{-1}$. The temperature is supposed to represent a realistic winter setting, where the precipitation does not necessarily have to be snow. The ground temperature is 1 °C.

The prevalent wind directions between October and January in Hamburg are west (270 °; case 27) and southwest (230 °; case 23) (Rosenhagen et al., 2011), which is represented in the simulation cases. The mean wind speed for the years 1986 to 2015 for a station located at Hamburg-Fuhlsbüttel in winter is $4\,\mathrm{ms}^{-1}$ (case M) (Meinke et al., 2014). In the simulated cases, the mean wind speed as well as a lower ($2\,\mathrm{ms}^{-1}$; case L) and higher wind speed ($6\,\mathrm{ms}^{-1}$; case H) are considered. If not stated otherwise, all values are defined at 10 m height. For a more realistic wind field, the Coriolis force is taken into account. The wind direction therefore turns clockwise and the wind speed increases with height. For example, for RH_MM27 at roughly cloud base height (365 m) the wind speed is $5.5\,\mathrm{ms}^{-1}$ and the wind direction is 288 °.

The simulations are initialised without cloud or rain water content and the relative humidity does not exceed 100 %. At surface, the humidity is 70 %, at 100 m, it is 75 %. Between 1 and 2 km height, the humidity reaches its highest value of 95 %. After that it decreases to 20 % at 5.5 km.

The simulations for the sensitivity studies start at 7:30:00 LST on 21 January 2000. The first hour of simulation is considered as model spin-up (phase I, ends 8:30:00 LST). Starting at 8:30:00 LST cloud and rain water content and a consistent relative humidity are prescribed for a duration of 5 minutes. Cloud and rain water are overwritten at every time step at the

forced grid points. No additional cloud or rain water is transported into the domain through the lateral boundaries. This is phase II of the model simulation (8:30:00-8:35:00 LST). After 8:35:00 LST, the simulation is no longer forced (phase III of model simulation: 8:35:00-8:40:00 LST). This approach is used to better identify effects of buildings on the boundary layer development (phase I), of the buildings on the falling rain (phase II) and effects of all interacting processes on precipitation (phase III).

In contrast to the evaluation simulations (Section 3.4), no radar data is used for the sensitivity studies. Instead, the rain water contents are chosen to follow the classification of the German Meteorological Service for light rain (0.5 mm in 10 minutes; case L), medium rain (0.9 mm in 10 minutes; case M) and heavy rain (1.7 mm in 10 minutes; case H) (Deutscher Wetterdienst, 2022a). The cloud water content is set to $0.001\,\mathrm{kg\,kg^{-1}}$ and the humidity is prescribed as 100 %. The forced area extends vertically from grid level 32 (345 m) to 38 (990 m) and horizontally covers the whole model domain.

3.5.2 Analyses Method

For the senstitivity studies, the integrated rain amounts are seperately analysed for phases II and III (there is no rain during phase I). To better compare the simulations, the integrated rain amounts are normalised using their weighted areal mean at 8:35:00 LST for phase II or at 8:40:00 LST for phase III. The weighted mean is chosen in order to take into account the stretched grid. 10 grid cells at each lateral boundary are removed, because of the increasing grid size towards these model boundaries (Section 3.5.1).

3.5.3 Results of Sensitivity Studies

Rain Heterogeneity on Ground

The rain heterogeneity on ground is represented by the weighted standard deviation. Tab. 3.2 shows the standard deviation of the rain amount on ground for the different cases (Tab.

Table 3.2: Variability given as the weighted standard deviation σ_n of the rain amount Pr and weighted means $\overline{P_{\text{rain}}}$ for phase II and phase III

Case ID	8:30-8:35 phase II		8:35-8:40 phase III	
	σ_n [%]	$\overline{P_{\text{rain}}}$ [mm]	σ_n [%]	$\overline{P_{\text{rain}}}$ [mm]
RH_LM27	3.2	0.18	2.1	0.31
RH_MM27	2.6	0.37	1.9	0.51
RH_HM27	2.0	0.84	1.9	0.94
RH_ML27	1.5	0.36	1.6	0.51
RH_MH27	2.7	0.37	2.8	0.50
RH_LL27	2.0	0.18	1.4	0.31
RH_HH27	2.2	0.80	2.6	0.88
RH_MM23	2.2	0.38	13.6	0.49
RH_MM27norog	2.3	0.37	1.8	0.51
RH_MM27nobuild	0.4	0.35	0.3	0.53

3.1) for phase II and III. It is by far the lowest for RH_MM27nobuild in both phases. Buildings have a strong effect on the wind field and vertical mixing up to the cloud level and they are one of the main causes of rain heterogeneity on the ground.

In contrast, the orography influence is small with case RH_MM27norog having only slightly smaller standard deviations than case RH_MM27, that includes orography and buildings. This might be different in urban areas with larger and more heterogeneous altitude differences, but the small and compared to the buildings spatially extended elevations in Hamburg (Fig. 3.4b) do have little impact on the precipitation heterogeneity on ground.

In phase II, the standard deviation increases with high initial wind speeds and low input rain amounts (prescribed values in phase I). Sedimentation transports rain downward, while the wind field transports rain drops in all directions. The sedimentation speed increases with increasing rain water content (Eq. 3.4). A higher input rain amount leads to a stronger downward transport of rain water, which means the wind field in relation becomes less influ-

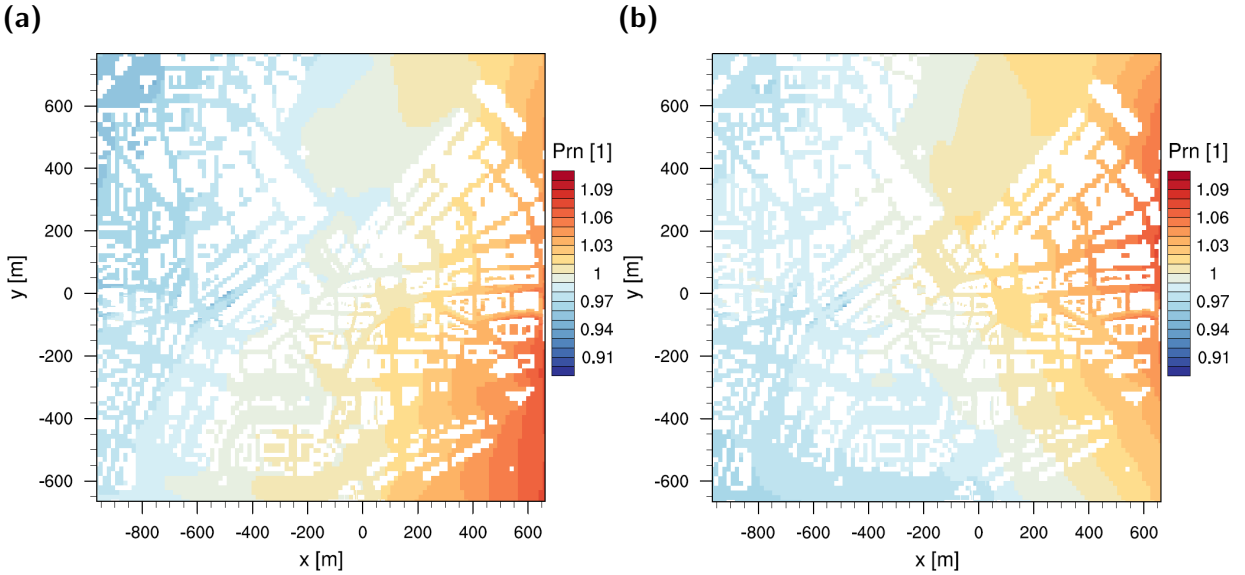

Figure 3.5: Horizontal cross section of the normalised rain amount Prn with weighted mean on ground in phase II for (a) RH_MM27 and (b) RH_MM23. [1] denotes non-dimensional values.

ential.

In phase III, the standard deviations do not vary much with changing input rain amount. Input wind speed and most importantly wind direction define the standard deviation. The more wind, the more variability for the 270 ° wind direction cases. For RH_MM23 (wind direction 230 °), the variability is exceptionally high.

The patterns of the rain amount on ground are given as deviation from the weighted area mean (Section 3.5.2). Stronger contrasts in colour indicate a higher variability. For phase II, the patterns of the deviations depend on the initial wind direction, which is defined at 10 m height. The patterns of the cases RH_MM27 and RH_MM23 are shown in Figure 3.5. Due to the influence of the Coriolis force, the wind turns clockwise with height. While the rain is transported to the south-east in case RH_MM27 (Fig. 3.5a), the maximum deviation for RH_MM23 is located east (Fig. 3.5b). For the other cases the overall pattern is similar to the one of RH_MM27.

The rain pattern on ground for RH_MM27nobuild (Fig. 3.6a) is much less hetero-

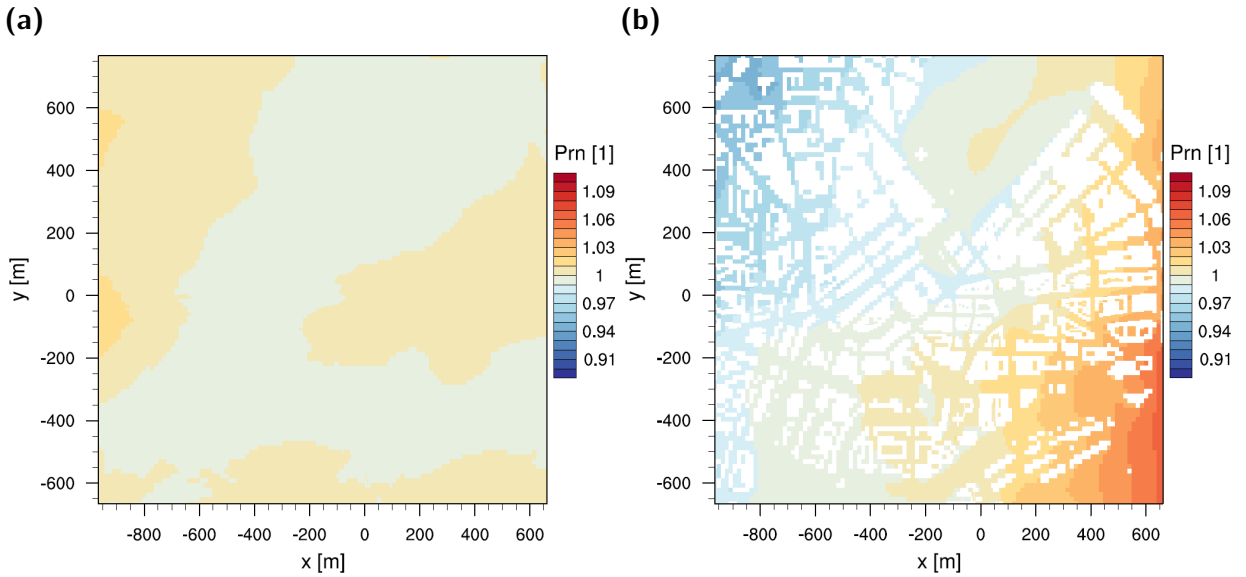

Figure 3.6: Horizontal cross section of the normalised rain amount Prn with weighted mean on ground in phase II for (a) RH_MM27nobuild and (b) RH_MM27norog. [1] denotes non-dimensional values.

geneous than the rain patterns of simulations including buildings. The rain patterns of RH_MM27norog (Fig. 3.6b) and RH_MM27 (Fig. 3.5a) are similar. However, adding the pattern of RH_MM27norog and RH_MM27nobuild would not lead to the pattern of RH_MM27, which means there are additional non-linear effects. Those additional non-linear effects become even more apparent in phase III (not shown).

In phase III the rain pattern depends on the input wind speed and direction. For RH_MM27, a maximum of the rain amount on ground develops in the southern half of the domain (Fig. 3.7a). This pattern is similar for RH_LM27 and RH_HM27 (not shown). For lighter rain (RH_LM27) it is more pronounced and further in the south. In RH_ML27, the rain amount is below the mean in the upper southern half of the domain (Fig. 3.8a). In RH_MH27, a north-south gradient develops with deviations greater 1 in the northern half of the domain (Fig. 3.8b). For RH_MM23, a strong north-south gradient develops (Fig. 3.7b).

In phase II local variations of roughly 3 % occur at $x = -500\,\mathrm{m}$ and $y = 0\,\mathrm{m}$ (Fig. 3.5), which do not appear in phase III (Figs. 3.7-3.8). This underlines that the rainfall pattern in

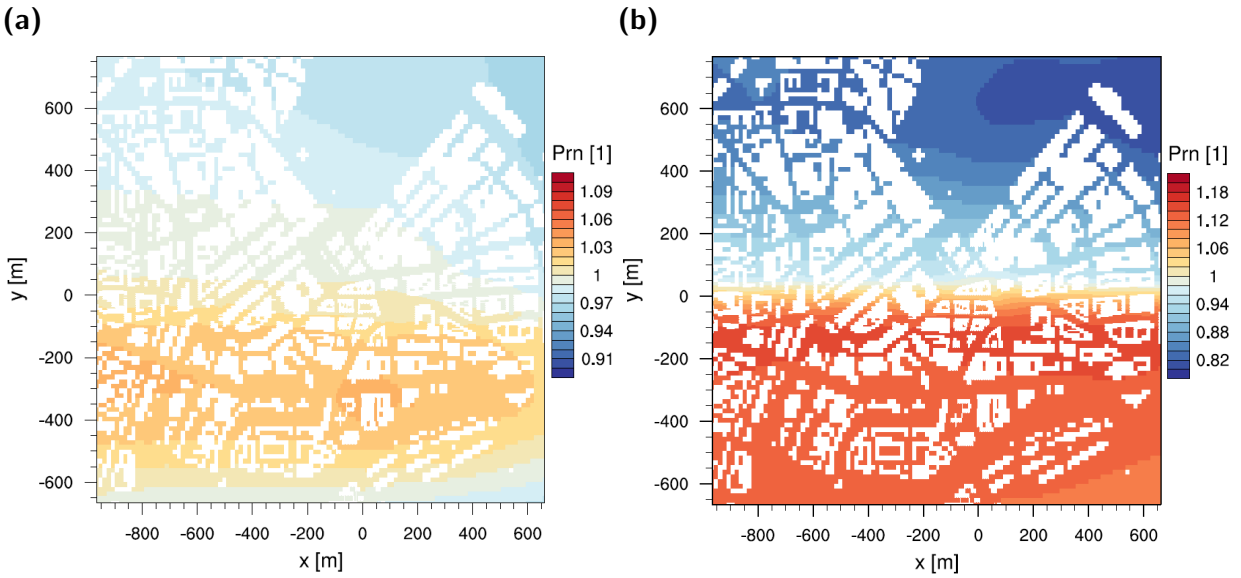

Figure 3.7: Horizontal cross section of the normalised rain amount Prn with weighted mean on ground in phase III for (a) RH_MM27 and (b) RH_MM23. Note the different scaling in (b) due to the higher values for Prn in RH_MM23. [1] denotes non-dimensional values.

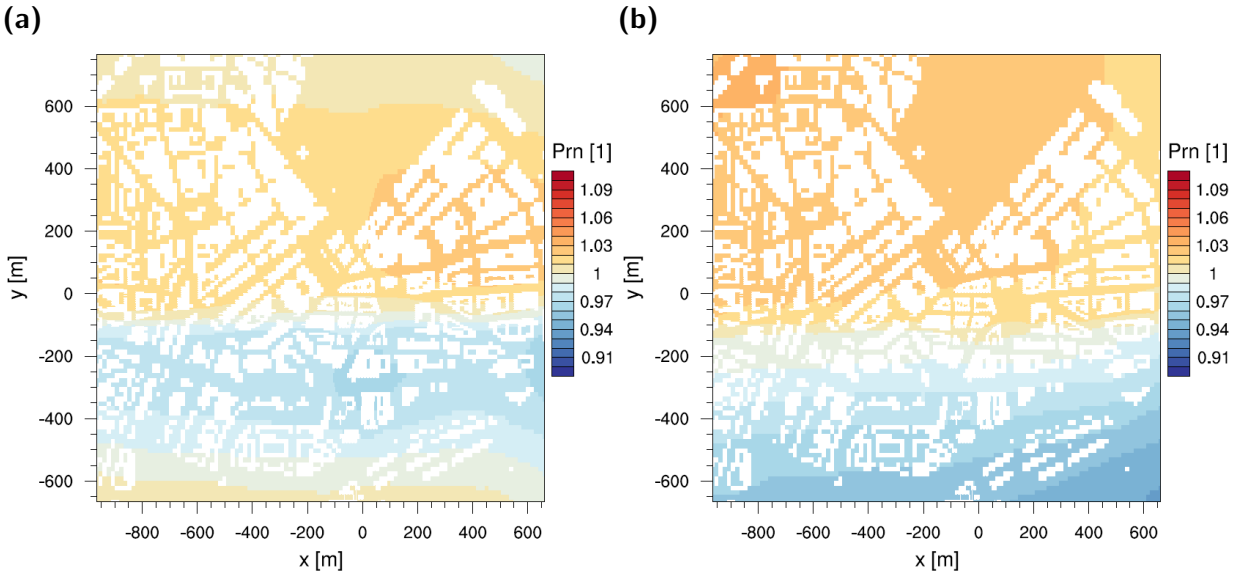

Figure 3.8: Horizontal cross section of the normalised rain amount Prn with weighted mean on ground in phase III for (a) RH_ML27 and (b) RH_MH27. [1] denotes non-dimensional values.

the neighbourhood scale is defined by the shape of the wind field above and that microscale effects of buildings are neglectable in comparison. The local variations seen in Fig. 3.5 do not occur when the orography is removed (Fig. 3.6b).

Low-level jet

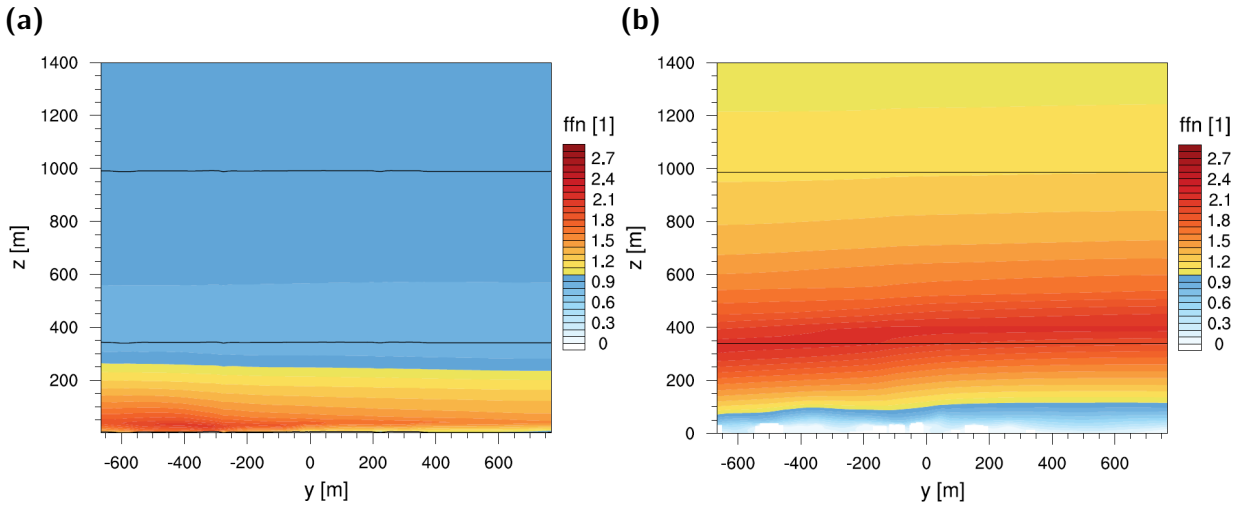

Figure 3.9: Vertical cross section with south to the left at $x = -108\,\mathrm{m}$ of the normalised wind speed ffn with initial value ff_{init} for (a) RH_MM27nobuild and (b) RH_MM27norog at 8:29:59 LST (phase I). The black lines mark the cloud's lower and upper boundary. [1] denotes non-dimensional values.

The wind field shaping the rain pattern on ground in phase III develops during phase I. It is presented at 8:29:59 LST for RH_MM27norog and RH_MM27nobuild in Fig. 3.9 and for RH_MM27 and RH_MM23 in Fig. 3.10 in vertical cross sections with south to the left at $x = -108\,\mathrm{m}$ (dashed line in Fig. 3.4b). There, the wind speed ff is normalised with the initial wind speed ff_{init} (Tab. 3.1). The cross sections are at roughly the centre of the domain. High normalised wind speeds develop above the urban boundary layer.

Wind speeds higher than in lower or higher levels at the top of the boundary layer indicate a low-level jet, which develops because momentum is accumulated above the urban boundary layer. Due to the stable stratification above the cloud base momentum is transported downward until the neutral stratification in lower heights reduces further transport downward.

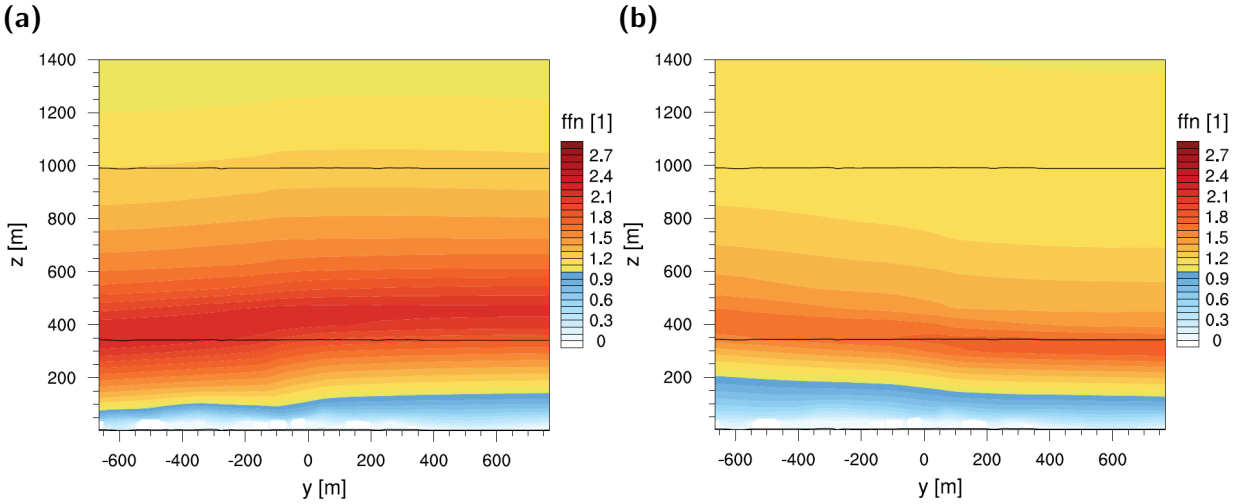

Figure 3.10: Vertical cross section with south to the left at $x = -108\,\mathrm{m}$ of the normalised wind speed ffn with initial value ff_{init} for (a) RH_MM27 and (b) RH_MM23 at 8:29:59 LST (phase I). The black lines mark the cloud's lower and upper boundary. [1] denotes non-dimensional values.

This low-level jet is not a modelling artefact.

Without buildings (Fig. 3.9a), the highest wind speeds are reached nearer to the ground. Otherwise the low-level jet is located roughly at cloud base height. With increasing initial wind speed the strength, width and height of the low-level jet increases (not shown). The shape of the low-level jet also differs depending on the initial wind direction. For RH_MM27, with a wind direction of 270 ° at 10 m height, the low-level jet is closer to the ground in the south-east and reaches its maximum wind speed in the north (Fig. 3.10a). For the initial wind direction of 230 ° used in RH_MM23 (Fig. 3.10b), the low-level jet is located closer to the ground in the north than in the south. The low-level jets of RH_MM27 (Fig. 3.10a) and RH_MM27norog (Fig. 3.9b) have a similar vertical structure supporting the hypothesis that the building induced turbulence influences the boundary layer height and thereby the cloud and rain band structure.

Rain heterogeneity on roofs

The pattern of the rain amount on roofs (Fig. 3.11) is similar to the pattern on the ground (Fig. 3.7a).

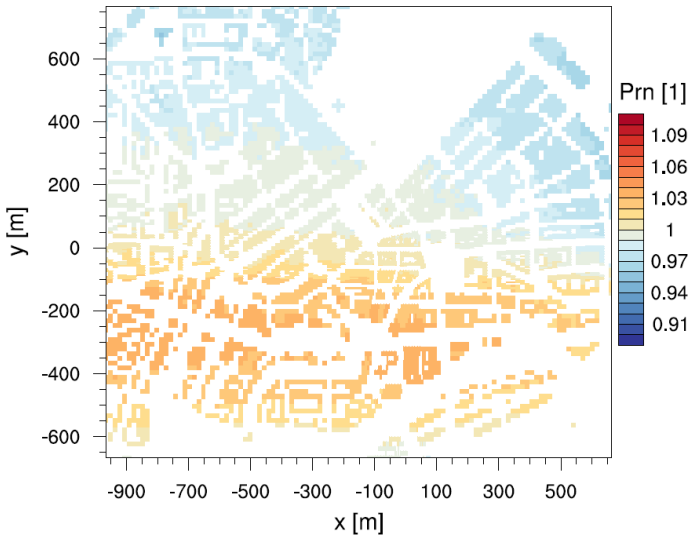

Figure 3.11: Normalised rain amount Prn with weighted mean on roofs in phase III for RH_MM27. [1] denotes non-dimensional values.

In order to assess differences of the rain amount at street and at roof heights, the building heights (Fig. 3.4c) are subdivided into portions of 10 m each. The rain amount at the portions are normalised with the weighted spatial mean of the rain amount on ground. Box plots show the 5^{th}, 5^{th}, 50^{th}, 75^{th}, and 95^{th} percentile of the resulting normalised rain amounts for phase II for RH_LM27, RH_HM27, RH_ML27, and RH_MH27 in Fig. 3.12 and for phase III for RH_ML27, RH_MH27, RH_MM27, and RH_MM23 in Fig. 3.13.

In phase II, the median value and the bandwidth of the percentiles increase with height in all four cases shown in Fig. 3.12. At 50 – 60 m height roughly 5 % more rain arrives. At higher roofs the difference even reaches 10 %, however, due to the small number of grid cells with roofs above 60 m, the results need to be treated with caution. More rain accumulates on higher surfaces, because rain is continously falling during the rain forcing. Rain arrives first on higher surfaces, which means that there is less time for water to evaporate.

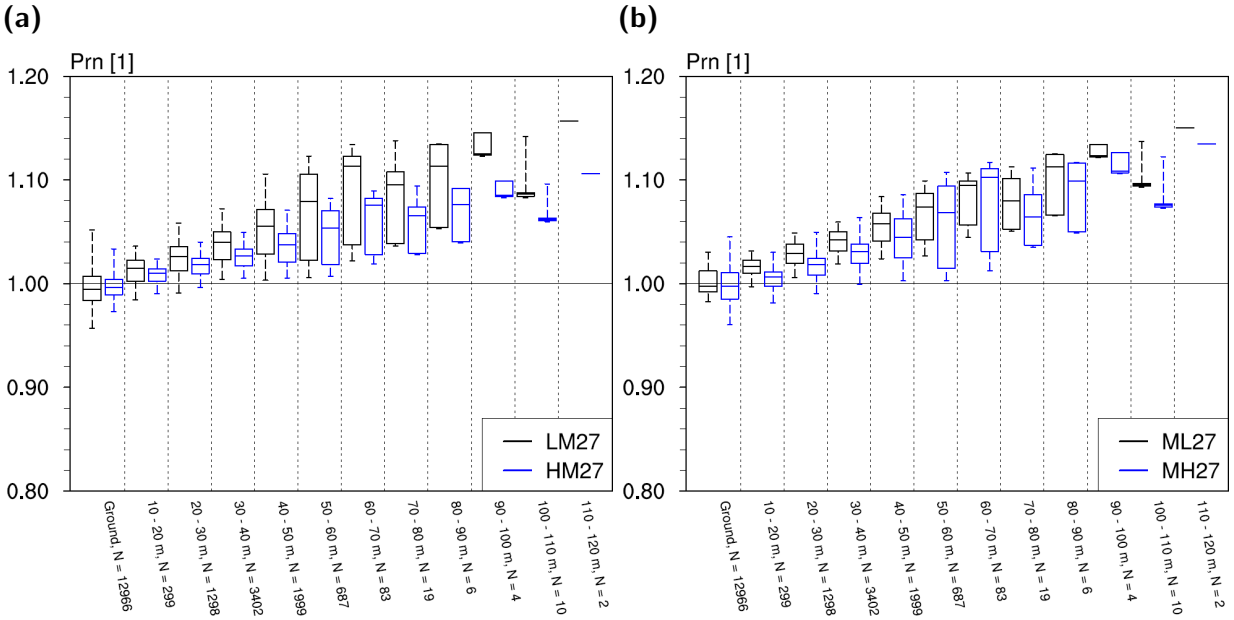

Figure 3.12: Box plots of the normalised rain amount Prn with weighted mean on ground for the rain amount on ground (two left boxes) and on roofs for different height intervals in phase II for (a) RH_LM27 (black) and RH_HM27 (blue) and (b) RH_ML27 (black) and RH_MH27 (blue). N denotes the number of grid cells. [1] denotes non-dimensional values.

More rain is accumulated on roofs than on ground for lower initial rain amounts (Fig. 3.12a). As the sedimentation speed depends on the rain amount (Eq. 3.4), rain falls faster in RH_HM27 than in RH_LM27. This means, there is less time for water to evaporate. More rain arrives on ground, which leads to smaller normalised values.

For lower wind speeds, the increase in the rain amount dependent on roof heights is steeper than for higher wind speeds (Fig. 3.12b). The rain amount on ground is similar in both cases, which means, more rain accumulates on lower roofs at low wind speeds. At lower wind speeds there is less horizontal advection.

For phase III, box plots of the rain amount at different heights are shown for RH_ML27, RH_MH27, RH_MM27, and RH_MM23 in Fig. 3.13. For RH_MM27, the maximum rain amount is located in the southern half of the domain. The corresponding box plots in Fig. 3.13b (black) show a small increase of the median for lower roof heights followed by a decrease for the higher roofs. For RH_ML27, a minimum of the rain amount is located in the southern

half of the domain. The corresponding medians in Fig, 3.13a (black) show little changes; they first decrease and then increase. The distribution of the roof heights combined with the characteristic rain patterns for the different wind speeds and wind directions explain the specific box plots. The processes within and above the rain band have a bigger influence on the distribution of rain on the surfaces than processes between buildings.

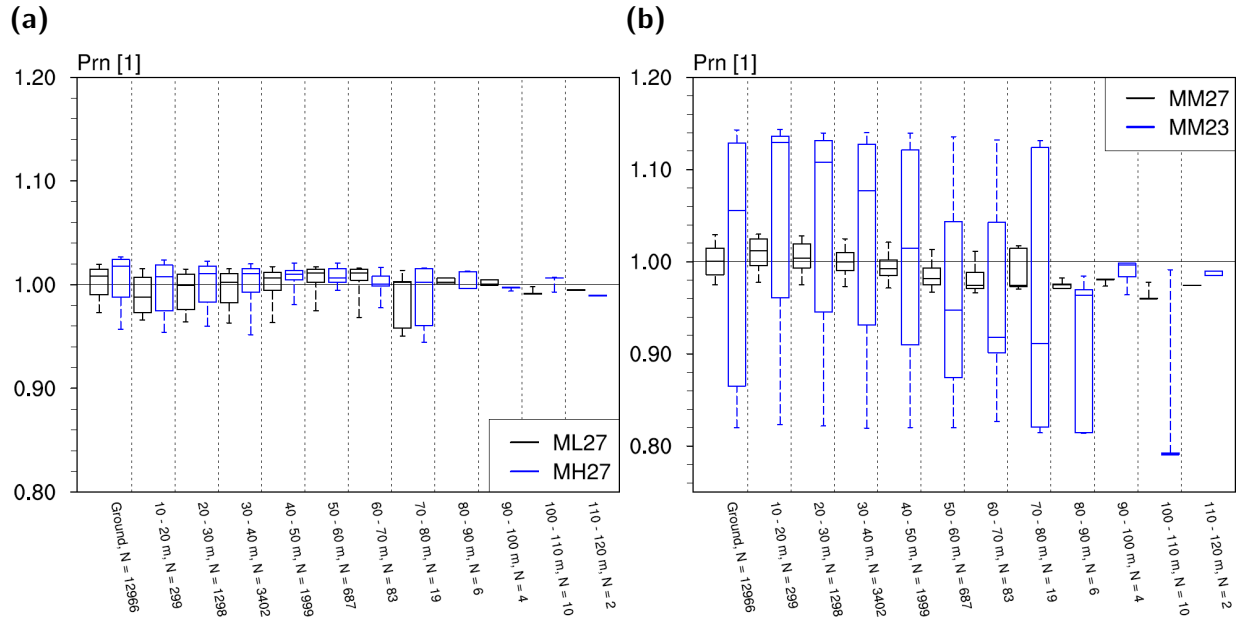

Figure 3.13: Box plots of the normalised rain amount Prn with weighted mean on ground for the rain amount on ground (two left boxes) and on roofs for different height intervals in phase III for (a) RH_ML27 (black) and RH_MH27 (blue) and (b) RH_MM27 (black) and RH_MM23 (blue). N denotes the number of grid cells. [1] denotes non-dimensional values.

3.6 Conclusions and outlook

Boundary conditions for cloud and rain water content at obstacle surfaces as well as a rain radar forcing have been implemented in the microscale, obstacle-resolving atmospheric model MITRAS. First, the extended model has been validated using in-situ measurements. Then, sensitivity studies were performed to assess the influence of different meteorological parameters and of the topography on the rain heterogeneity within an urban neighbourhood.

The validation in this study focuses on the performance of the model with respect to

rain processes. MITRAS' capability to simulate the main features of an urban boundary layer has already been shown in Grawe et al. (2013). A real rain event was simulated using the newly introduced rain radar forcing and the model produced plausible results. The results of the sensitivity studies confirmed that. Therefore, the model enhancement can be considered reasonably trustworthy.

For the sensitivity studies simulations with different initial wind speeds, rain amounts, and wind directions, as well as different domain configurations were performed. Above the urban boundary layer high wind speeds develop during phase I. These are caused by building induced heterogeneities in the boundary layer and downward momentum transport.

In order to assess the sensitivity of the rain heterogeneity solely within the urban boundary layer, the effects of the wind field and rain processes within and above the rain band were excluded during the forcing phase (phase II, 8:30:00-8:35:00 LST). It was found that the higher the initial wind speeds and the lower the input rain rate, the higher the heterogeneity. However, when the effects of all processes are included (phase III, 8:35:00-8:40:00 LST), the heterogeneity is higher with increasing initial wind speed at constant wind direction and is less sensitive towards the initial rain rate.

The pattern of rain on ground is defined by the wind field and the effects of the rain processes within and above the rain band and well above the buildings. In order to predict the rain pattern on ground, knowledge of the wind field is crucial. The impact of the urban surface geometry representation within the model on the spatial and temporal rainfall variability in the mesoscale was found evident in Li et al. (2021). Our study shows that this also applies for the scale of an urban neighbourhood. Consequently, the city has an effect on the rain pattern on ground. However, the high reaching effects of the city on the location and shape of the low-level jet and the cloud and rain band structure are far more important than the flows between single buildings.

Assuming changing the input wind direction is like turning the city and thereby changing

the city's geometry; the results indicate a strong influence of the geometry on the rain pattern on ground. This is consistent with the found relevance of the buildings on the urban boundary layer, since the flow around and above the buildings and the vortex interactions within the urban canopy layer are influenced by the building forms. However, a change of the wind direction at 10 m height from 270 ° in RH_MM27 to 230 ° in RH_MM23 is a rather huge step. According to Claus et al. (2012), for instance, changes of 45 ° in the wind direction can alter the roughness length by a factor of four. Performing simulations with smaller variations in the wind direction could be beneficial.

In phase II, 5 to 10 % more rain accumulates on roofs than on ground. With respect to the neighbourhood scale rain pattern, the influence of the processes above override the effects of those influencing precipitation within the canopy layer. The distribution of the buildings in the domain is more relevant than the height of the roofs. Still, comparably more rain accumulates on roofs for lower initial rain amounts and higher initial wind speeds. That confirms the results for the ground.

To sum up, MITRAS including the newly introduced extensions produces plausible results. MITRAS is, to our knowledge, the first microscale, obstacle-resolving atmospheric model, that employs a rain parameterisation. For the heterogeneity of rain within an urban neighbourhood, the processes between buildings are far less relevant than anticipated. The rain pattern on surfaces is defined by the wind field and processes above the urban boundary layer. For a realistic representation of a rain event in an urban neighbourhood, however, the buildings are important. Their influences impact the rain pattern; therefore knowledge of the meteorological situation and of the city's geometry is crucial.

The current model simulations were performed for relatively low clouds (winter situation in mid-latitudes) with an upper model top at $\sim$ 1290 m. Summer clouds reach much higher and it is advisable to extend the model domain up to several km, depending on cloud type even the tropopause. Otherwise the top boundary conditions might influence processes at

cloud level or might even induce reflections of vertically propagating waves at the upper model boundary. For higher reaching clouds a higher model domain is advisable.

In the future, a snow scheme will be introduced to further investigate precipitation heterogeneities in winter. Also a more comprehensive evaluation concerning the radar forcing is planned. Increasing computational power and ongoing efforts in the optimisation of the model code will reduce computing resources. Then, larger or more detailed neighbourhoods may be simulated.

4 Modelling Snow Processes in an Urban Neighbourhood Using an Obstacle-resolving Model

Preface

This chapter was submitted for publication as:

Samsel, K. S. and M. Boettcher and K. H. Schlünzen and D. Grawe and K. Sieck: Modelling snow processes in an urban neighbourhood using an obstacle-resolving model. *Meteorologische Zeitschrift*, in review.

The full manuscript of the submitted paper is included in this chapter. Layout and numbering within the manuscript were adopted to fit this thesis. The prefix 'SP_' (**S**now **P**rocesses) was added to the simulation names in the text (not in the figures) to distinguish them from the simulation names in Chapter 3. All references are combined in References. Supporting information and statements submitted with this manuscript can be found in Appendix C. Symbols are adjusted and included in the List of Symbols.

K. H. Schlünzen has contributed to the conceptualisation. M. Boettcher, K. H. Schlünzen, and D. Grawe contributed to the discussion of the results.

4.1 Abstract

The urban morphology and meteorological parameters affect patterns of snow fall and snow melt. For warm temperate climate cities like Hamburg, research on snow heterogeneities is lacking especially for small urban scales like a neighbourhood, which covers an area of a few km^2. Compared to rain, the sedimentation velocity of snow is lower, which increases the influence of building induced winds. In this study, the obstacle-resolving microscale model MITRAS is applied for simulations with different initial wind speeds, temperatures, precipitation amounts and domain configurations. The model includes a one-category ice scheme and a snow cover scheme. A city's geometry is crucial for determining precipitation distribution and

its fate (e.g. melting/freezing) within an urban neighbourhood. For the heterogeneity of the accumulated snow amounts and of snow water equivalents on ground, it is found that building induced winds are more influential for precipitating snow than for rain. Heterogeneities of snow melt induced by temperature variations are identified, which are influenced by the presence of water surfaces and by building induced circulation patterns.

4.2 Introduction

Winter precipitation events in cities of warm temperate climate may impact pedestrian comfort and traffic due to icy and snowy grounds. However, research concerning the influence of urban areas on precipitation usually focuses on large scale modifications of precipitation patterns (e.g. Liu and Niyogi, 2019; Zhang et al., 2022; Lu et al., 2024), or the effects of snow cover and snow melt in cities of snow or cold climate (e.g. Moghadas et al., 2016; Dobre et al., 2017; Järvi et al., 2017). When considering directly building induced atmospheric phenomena on a building scale (microscale γ and β following Tab. 2.1 in WMO, 2023b), the distribution of high snow loads is frequently investigated (e.g. Chen et al., 2021; Zhang et al., 2021; Zhou et al., 2021). However, such high snow loads are unusual in warm temperate climate cities like Hamburg, Germany. Nevertheless, snow events are no uncommon occurrence in Hamburg (Meinke et al., 2018).

On a neighbourhood scale (order of magnitude $1\,\mathrm{km}^2$), buildings are expected to have an effect on the heterogeneity of snow and frost due to building induced vertical winds. For rain, Ferner et al. (2023, Chapter 3) showed that processes between obstacles are of small influence for rain already falling compared to their influences above the canopy layer. The effects of the meteorological situation and the city's geometry on the wind field in higher levels are found to be more influential. With snow generally having lower sedimentation velocities than rain, snow should be more susceptible to the surrounding wind field in the canopy layer and, consequently, the influence of obstacles on the heterogeneity of snow should be larger

than for rain. Knowledge of snow heterogeneities within an urban area is a useful first step towards the analyses of frost heterogeneities.

Even for rain, high-resolution precipitation data, that captures the spatial variability within an urban neighbourhood, are not generally available. However, variabilities can be expected since even for small, rural domains, a considerable high spatial variability of rain fall has been found (Jensen and Pedersen, 2005; Pedersen et al., 2010; Bohnenstengel et al., 2011; Terink et al., 2018). Measuring precipitation using rain gauge networks and high-resolution weather radars in urban areas comes with challenges, which are listed in a review on rain fall variabilities from a hydrology perspective by Cristiano et al. (2017). Snow measurements in an urban area are even more rare than rain measurements and thus a reliable horizontal distribution and heterogeneities can not be derived.

For creating high-resolution precipitation data and assessing the influence of urban neighbourhoods on snow distribution, numerical modelling is a suitable method. There are microscale, obstacle-resolving atmospheric models which include various physical processes for a realistic representation of the urban boundary layer (e.g. PALM, RAMS; Maronga et al., 2020; Pielke et al., 1992). They include parameterisations for cloud processes, but no investigations of the heterogeneity of rain or snow in urban neighbourhoods were performed, yet. The obstacle-resolving, microscale transport and stream model MITRAS (Salim et al., 2018) includes precipitation effects (Samsel et al., 2025, Chapter 2). For rain, model results have been compared to in-situ measurements (Ferner et al., 2023, Section 3.4.2), while the snow scheme was tested for plausibility (Samsel et al., 2025, Section 2.7.4).

In this study, the influence of meteorological parameters and urban morphology on the heterogeneity of snow fall and snow amounts on ground in a small urban setting is investigated using MITRAS. An evaluation of the snow scheme at least similar as done for the cloud and rain parameterisation in Ferner et al. (2023, Section 3.4.1), where the results of simulations forced with radar data were compared to in-situ precipitation, is not possible because of a

lack of snow measurements. For instance, radar data as input for the model are not available because the high resolution radar is not able to measure snow fall correctly. Radar data with coarser horizontal resolution, e. g. from DWD (German weather service), may include the dualpol data necessary for snow measurements, but the data are not processed yet and radar data with a coarse horizontal resolution do not include snow heterogeneities in the resolution of a neighbourhood.

A brief description of the model and the representation of winter precipitation are given in Sections 4.3.1 and 4.3.2. The setup and analyses methods for the sensitivity studies are provided in Section 4.3.3. For the sensitivity studies, the city centre of Hamburg (Germany) has been chosen, since for this neighbourhood a detailed building mask (Salim et al., 2015) is available and has been applied for investigations on rain heterogeneity (Ferner et al., 2023, Section 3.5.3). Simulations have been performed for different meteorological situations (initial wind speeds, snow amounts, wind directions), and topographies (with and without orography and buildings). The results are qualitatively assessed in Section 4.4 and conclusions are presented in Section 4.5.

4.3 Method

4.3.1 Numerical model

The microscale, obstacle-resolving transport and stream model MITRAS is a three-dimensional, non-hydrostatic, prognostic, numerical model and is part of the M-SYS model system (Trukenmüller et al., 2004; Schatzmann et al., 2006). MITRAS has been validated in comparison to wind tunnel data (Schlünzen et al., 2003; Grawe et al., 2013) and evaluated using the VDI guideline for microscale, obstacle-resolving models (Grawe et al., 2015). Model documentations can be found in Salim et al. (2018) and Schlünzen et al. (2018a).

4.3.2 Representation of winter precipitation in MITRAS

As a comprehensive description of the inclusion of snow in MITRAS is provided in Samsel et al. (2025, Sections 2.5 and 2.6), only a brief summary will be given here. For the snow cover scheme, the approach by Boettcher (2017) as used in MITRAS' mesoscale sister model METRAS (Trukenmüller et al., 2004; Schatzmann et al., 2006; Schlünzen et al., 2018a) is adjusted for considering obstacles and microscale time spans as used in MITRAS model runs. Snow on ground is either represented as the accumulated snow amount P_{snow} [mm] or as the snow water equivalent SWE [m] (Eq. 4.1), which both denote the water amount available in the snow. With P_{snow} the amount of snow resulting from the precipitation rate P_{rate} is provided, wheras SWE takes also the evaporation rate E [ms^{-1}] and melting rate M [ms^{-1}] into account:

$$\frac{\partial SWE}{\partial t} = \frac{10^{-3}}{3600} \cdot P_{\text{rate}} - E - M. \tag{4.1}$$

To calculate the height of snow, z_{snow} [m], the density of water ρ_{w} and of the snow pack ρ_{snow} is needed:

$$z_{\text{snow}} = \frac{\rho_{\text{w}}}{\rho_{\text{snow}}} \cdot SWE. \tag{4.2}$$

In the model, ageing of a snow pack is represented by increasing ρ_{snow} from a minimal snow density of $\rho_{\text{min}} = 100\,\text{kg}\,\text{m}^{-3}$ to $\rho_{\text{max}} = 300\,\text{kg}\,\text{m}^{-3}$ (Verseghy, 1991; Douville et al., 1995; Dutra et al., 2010). In this study, only short time spans of 1.5 hours are considered, therefore the new snow on ground can be assumed to remain fresh ($\rho_{\text{snow}} = \rho_{\text{min}}$). Consequently, following Eq. (4.2) the snow pack height can be assumed to be ten times the snow water equivalent.

The cloud microphysics parameterisation in MITRAS is based on the implementation in METRAS (Köhler, 1990; Schlünzen et al., 2018a). A one-category ice scheme as described in

Doms et al. (2011) is added. The cloud microphysics parameterisation includes condensation and evaporation as well as evaporation and sublimation in the sub-saturated areas below the cloud, autoconversion and nucleation of cloud water to rain water or snow, accretion or riming of cloud droplets, shedding of snow particles, as well as melting and freezing. For rain, a Marshall-Palmer size distribution (Marshall and Palmer, 1948) and for snowflakes, a Gunn-Marshall distribution (Gunn and Marshall, 1958) is assumed. For the sedimentation of rain and snow, terminal velocities, v_{TR} and v_{TS}, are calculated. The terminal velocity of rain is given as

$$v_{TR} = \sqrt{\frac{\rho_{\text{ref}}}{\rho_0}} \cdot 68.81 \cdot \left(10^{-3} \cdot \rho_0 q_1^{2r}\right)^{0.1905} \tag{4.3}$$

with the reference atmospheric density $\rho_{\text{ref}} = 1.29\,\text{kgm}^{-3}$, the basic state atmospheric density ρ_0, and the rain water content q_1^{2r} (Köhler, 1990; Schlünzen et al., 2018a).

The terminal velocity of snow is similarly given as

$$v_{TS} = \sqrt{\frac{\rho_{\text{ref}}}{\rho_0}} \cdot 4.82 \cdot \left(10^{-3} \cdot \rho_0 q_1^{3s}\right)^{0.075} \tag{4.4}$$

with the snow water content q_1^{3s} (Doms et al., 2011). Both Eqs. (4.3) and (4.4) include a correction factor $\sqrt{\frac{\rho_{\text{ref}}}{\rho_0}}$, that takes smaller atmospheric densities at higher altitudes into account. The factor of 10^{-3} results from the conversion of the equation originally given in $\text{g}\,\text{cm}^{-3}$ units to SI units.

4.3.3 Sensitivity studies

Model setup

The domain for the sensitivity studies represents a realistic urban geometry including various street configurations, open spaces, water surfaces, orography and buildings of different heights. The city centre of Hamburg (Germany) was chosen (Fig. 4.1). The building data

are taken from Salim et al. (2015). They are based on the Digital Terrain Model, the data of the German geo-information system ATKIS (Official Topographic-Cartographic Information System; Müller and Seyfert, 2000), and on the 3D-urban model data (LoD 2) for building details.

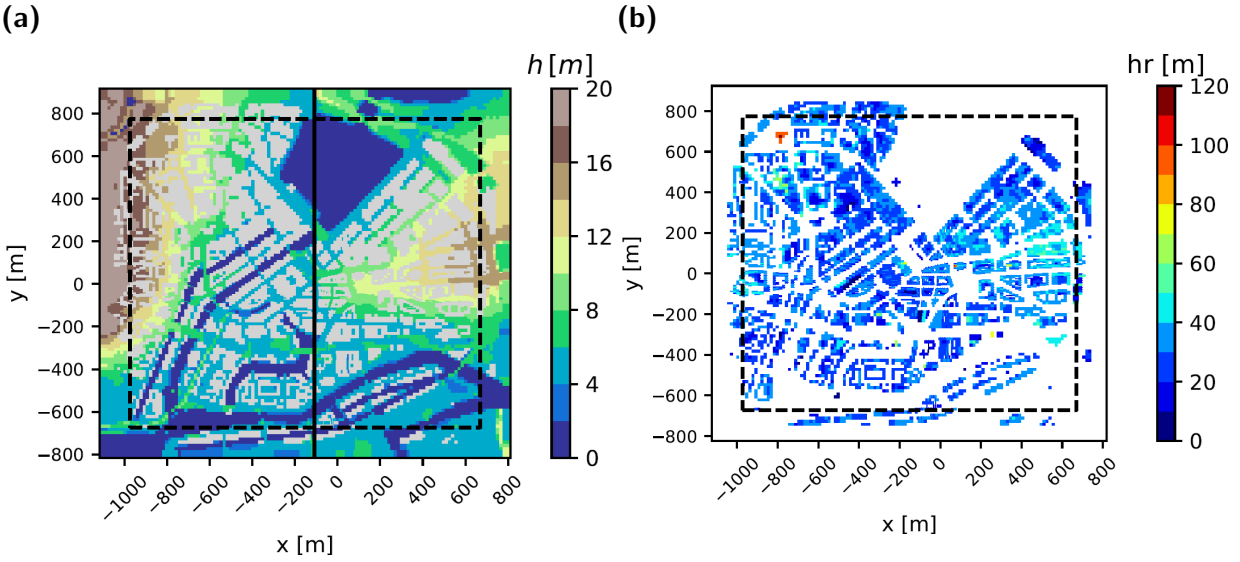

Figure 4.1: Details of the simulation domain with (a) the orography height h (in m, coloured) with buildings in grey, water surfaces in dark blue, and a solid line denoting the location of vertical cross sections and (b) roof top heights hr (in m, coloured). Values outside the dashed box are not taken into account in the analyses.

High resolution obstacle-resolving modelling of complex domains including cloud microphysics is computationally expensive. Yet, the places of interest should be resolved with at least three grid cells. For the representation of relevant phenomena in street canyons at least five grid cells are recommended (VDI, 2017). This necessitates the usage of a fine grid resolving the area of main interest embedded in a stretched grid to reduce the number of grid cells without losing too much accuracy. The resulting domain horizontally extends $1.6 \times 1.8\,\mathrm{km}^{-2}$ around Hamburg City Hall and vertically up to 5 km to allow for simulation of changes in cloud development. The grid stretches from a resolution of 3.5 m in all directions to horizontally 15 m and vertically 150 m with a stretching factor of 1.175. The highly-resolved, equidistant area extends from $x = y = -100\,\mathrm{m}$ to $x = y = 50\,\mathrm{m}$ and vertically to $z = 50\,\mathrm{m}$. The

Table 4.1: Simulated cases with initial close-to-ground air temperature T_{init} in °C, initial wind speed ff_{init} at 10 m height in $\mathrm{m\,s^{-1}}$, and the mean area densities of the vertically integrated water vapour $\overline{\rho_A^1}$, cloud, snow and rain water content $\overline{\rho_A^{2c}}$, $\overline{\rho_A^{2r}}$, $\overline{\rho_A^{3s}}$ in $\mathrm{kg\,m^{-2}}$ after the forcing phase.

Case ID	T_{init}	ff_{init}	$\overline{\rho_A^1}$	$\overline{\rho_A^{2c}}$	$\overline{\rho_A^{2r}}$	$\overline{\rho_A^{3s}}$	Notes
SP_ML27	1	2	6.1	0.8	0.0	0.9	
SP_LL27	−1	2	5.2	0.8	0.0	0.9	
SP_HL27	11	2	12.7	0.7	2.1	0.7	
SP_MS27	1	4	5.7	0.8	0.0	0.9	
SP_LS27	−1	4	4.9	0.8	0.0	0.9	
SP_HS27	11	4	11.7	0.8	2.2	0.8	
SP_LM27	−1	6	4.6	0.8	0.0	1.0	
SP_LL27_norog	−1	2	5.3	0.8	0.0	0.9	no orography
SP_LL27_nobuild	−1	2	5.9	0.8	0.0	1.0	no buildings
SP_LS27_norog	−1	4	4.9	0.8	0.0	0.9	no orography
SP_LS27_nobuild	−1	4	5.8	0.8	0.0	1.0	no buildings
SP_LL27_light	−1	2	5.2	0.8	0.0	0.5	light precipitation
SP_LL27_heavy	−1	2	5.3	0.8	0.0	2.0	heavy precipitation

area considered for the analyses of the sensitivity studies covers the whole domain excluding 10 grid cells at each lateral boundary (Fig. 4.1a).

The sensitivity studies are performed with the goal of assessing the influence of the meteorology as well as of the topography (orography and buildings) on the snow heterogeneity within an urban neighbourhood and include 13 simulations (Tab. 4.1). The first letter of the case ID denotes the temperature (Low, Medium, High), the second the wind speed (Light, Soft, Moderate breeze), and the number refers to the wind direction 10 m above ground (270 °). The wind direction 270 ° is a prevalent wind direction between October and January in Hamburg (Rosenhagen et al., 2011). The wind speed soft breeze ($4\,\mathrm{m\,s^{-1}}$) is based on the mean wind speed at 10 m above ground for the years 1986 to 2015 for a station located at Hamburg-Fuhlsbüttel (Meinke et al., 2014). The suffix norog stands for not considering orography, nobuild for not considering buildings, light and heavy for less or more intense

precipitation compared to the cases without suffix.

The initial surface pressure is prescribed with 990 hPa and the initial potential temperature gradient with $0.001\,\mathrm{K\,m^{-1}}$. The soil and water temperatures are given with 1 °C for all cases. At surface, the humidity is 70 % with a linear increase to 75 % at 100 m above ground. A further increase to 95 % at 1000 m above ground is initially prescribed. The values remain constant to a height of 2000 m above ground. Above, the relative humidity is initialised to decrease to 20 % at the upper model boundary. Using the initial values, balanced vertical profiles are calculated solving the same equations as used in the 3D model simulations, but assuming horizontal homogeneity. The Coriolis force is taken into account, but no cloud, rain or snow water contents are initialised and the relative humidity does not exceed 100 %. Compared to the initial values close to ground, the wind direction is turned clockwise and the wind speed increases at higher levels. For example, for SP_LL27 with an initial wind speed of $2\,\mathrm{m\,s^{-1}}$ and direction 270 ° at 10 m above ground, the wind speed is $2.6\,\mathrm{m\,s^{-1}}$ and the wind direction is 288 ° at cloud base height (340 m).

The simulations for the sensitivity studies start for 7:30:00 LST (Local Solar Time) on 21 January 2000 with the first simulation hour being considered as model spin-up time. Starting for 8:30:00 LST, cloud and snow water content as well as a relative humidity of 100 % are prescribed for a duration of five minutes (8:30:00-8:35:00 LST; forcing phase) for all simulations. No rain water content is forced. The forcing is used from grid level 32 (345 m) to 38 (990 m) covering the whole horizontal extension of the model domain. During the forcing phase, simulated water vapour, cloud and snow water contents are overwritten at the forced grid points at every time step. The forcing ends at 8:35:00 LST.

Constant values are prescribed for cloud and snow water content. For cloud water content, the critical value for autoconversion ($q^{2c}_{1,cri} = 10^{-3}\,\mathrm{kg\,kg^{-1}}$, Samsel et al., 2025, Section 2.3.2) is chosen. For all simulations except SP_LL27_light and SP_LL27_heavy, the same initial values for snow water content is prescribed. For lighter precipitation half the value and

for heavier precipitation the double value of snow water content is taken. In Tab. 4.1, the mean area densities for 8:35:00 LST are provided to show how much water is available for the simulation after the forcing phase, when water variables are no longer overwritten. For the mean area densities, the water vapour, cloud, rain and snow water contents are summed up and the weighted spatial mean is taken. The higher the temperature, the higher the saturation specific humidity and thus the more water vapour is contained in the atmosphere for similar relative humidities. Significantly more water vapour is initialised in the warm cases SP_HL27 and SP_HS27 compared to the other cases.

Analyses method

The integrated precipitation amounts are separately analysed for the forcing phase (8:30:00 to 8:35:00 LST) and thereafter (8:35:00 to 9:00:00 LST). The heterogeneity of precipitation is represented using the standard deviation σ_n in percent of the normalised snow or rain amounts on ground $Pn_$snow and Prn. The precipitation amounts are normalised with the areal mean accumulated precipitation amounts of the respective time of interest (8:30:00 to 8:35:00 LST or 8:35:00 to 9:00:00 LST). The stretched grid is taken into account by calculating area weighted means. The area of interest excludes the 10 grid cells close to the lateral boundaries (cells outside the box marked by dashed lines in Fig. 4.1). If the mean precipitation is below 0.1 mm, it is considered zero as commonly used rain gauges are not more accurate than that (WMO, 2023a). Note that the snow precipitation amount P_{snow} is a water equivalent value and does not represent the accumulated snow height (see Section 4.3.2).

4.4 Results

For all cases except the high temperature cases (SP_HS27, SP_HL27) precipitation occurs as snow. For the high temperature cases, snow is formed in the higher levels, where temperatures

are below zero. Small amounts reach the ground (Tab. 4.2). In cases SP_HL27 and SP_HS27 for the same relative humidity profiles as in the other cases more water vapour is initialised (Tab. 4.1), leading to larger rain amounts than snow amounts (Tab. 4.2). No rain but only snow is produced in the low temperature cases and small amounts of rain are produced for the medium temperature cases (SP_ML27, SP_MS27).

Table 4.2: Precipitation heterogeneity on ground given as the weighted standard deviation σ_n in % of the amount of rain P_{rain} or snow P_{snow} and the corresponding weighted areal mean ($\overline{P}_{rain}$ or $\overline{P}_{snow}$). The values for the standard deviation are colour coded with grey for $0-3\,\%$, blue $3-6\,\%$, orange $6-9\,\%$, and red $10-12\,\%$.

Case ID	8:00-8:35			8:35-9:00		
	$\overline{P}_{snow}$ [mm]	$\overline{P}_{rain}$ [mm]	σ_n [%]	$\overline{P}_{snow}$ [mm]	$\overline{P}_{rain}$ [mm]	σ_n [%]
SP_ML27	0.2	0.004	8.8	1.6	0.007	3.0
SP_LL27	0.2	0	8.9	1.6	0	2.6
SP_MS27	0.2	0.004	11.2	1.4	0.004	3.3
SP_LS27	0.2	0	11.3	1.5	0	2.0
SP_LM27	0.2	0	10.5	1.6	0	1.7
SP_LL27_norog	0.2	0	6.7	1.6	0	0.7
SP_LL27_nobuild	0.2	0	2.0	1.7	0	2.1
SP_LS27_norog	0.2	0	10.1	1.6	0	1.3
SP_LS27_nobuild	0.2	0	3.0	1.7	0	2.0
SP_LL27_light	0.1	0	–	1.1	0	2.8
SP_LL27_heavy	0.4	0	7.4	2.7	0	1.6
SP_HL27	0.02	3.7	0.9	0.05	3.4	2.6
SP_HS27	0.03	3.6	0.8	0.05	3.4	3.1

4.4.1 Precipitation heterogeneities during the forcing phase

Snow has smaller sedimentation speeds than rain (compare Eq. 4.4 with Eq. 4.3), which should make it more susceptible to the wind field. This is especially true during the forcing phase, where only the processes below the prescribed precipitation band are taken into account and the amounts of snow or rain water content are small (Section 4.3.3). For rain it has been shown by Ferner et al. (2023, Chapter 3) that the lower the sedimentation speed (i.e.

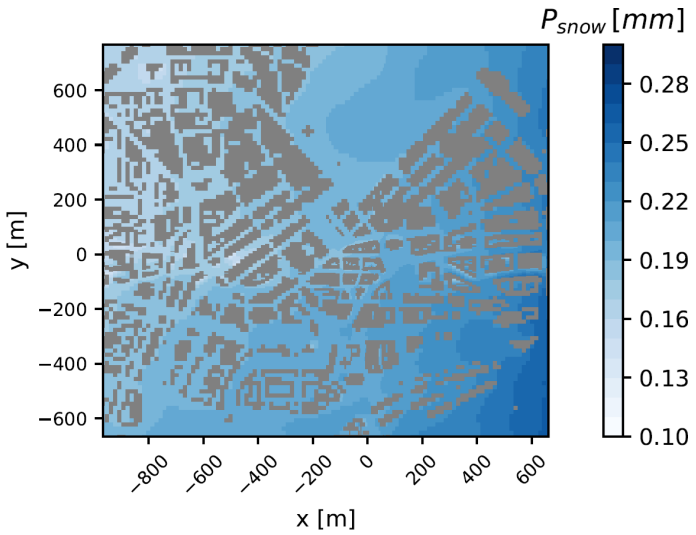

Figure 4.2: Horizontal cross section of the accumulated snow amount P_{snow} on ground at 8:35:00 LST for SP_LS27.

the smaller the initial rain amount), the higher the influence of the surrounding wind field on the rain distribution during the forcing phase. The precipitation heterogeneity on ground described by σ_n (Section 4.3.3) decreases with increasing initial snow amount (SP_LL27 and SP_LL27_heavy, Tab. 4.2). For the light precipitation case SP_LL27_light, no heterogeneity could be calculated as not enough snow has arrived on the ground after five minutes.

During the forcing phase, the snow heterogeneity increases with increasing initial wind speed (e.g. SP_ML27 and SP_MS27). In comparison with the rain heterogeneities (cases SP_HL27, SP_HS27 and the heterogeneities provided in Ferner et al. (2023, Tab. 3.2)), the snow heterogeneities are generally higher, which underlines the increased sensitivity of the snow distribution on ground to the wind field due to its lower sedimentation speed. In case SP_LM27 the heterogeneity is lower than for SP_LS27 even though the initial wind speed is higher. There is only a single case with comparably high wind speed, so no regularity for the relation of heterogeneity and wind speed can be derived.

Due to the susceptibility of precipitating snow to the wind field, we expect to find building scale variations of the snow amount on ground near buildings. For SP_LS27, the accumulated snow amount P_{snow} is shown in Fig. 4.2 for 8:35:00 LST at the end of the forcing phase.

Besides a neighbourhood scale North-West to South-East gradient of snow amount related to the incoming flow direction, building scale heterogeneities appear at $x = -500\,\mathrm{m}$ and $y = 0\,\mathrm{m}$ (Alsterfleet), $x = 400\,\mathrm{m}$ and $y = 0\,\mathrm{m}$ (Altstädterstraße), or $x = -200\,\mathrm{m}$ and $y = -350\,\mathrm{m}$ (office building at Willy-Brandt-Straße). Those building scale variations generally occur in parts of the model domain, where e.g. street canyon or canals between buildings are well resolved and in general a high model resolution at least in one direction (Section 4.3.3) is used. Building scale variations are also visible around the Emporio building ($x = -750\,\mathrm{m}$, $y = 700\,\mathrm{m}$), where the resolution is coarser, but sufficient to resolve flow and snow transport differences around the large building.

4.4.2 Influences of canopy layer induced processes on precipitation

Obstacles are expected to have a strong effect on the wind field and therefore on the precipitation heterogeneity on ground. After the forcing phase, the building scale heterogeneity becomes less visible and the neighbourhood scale gradient dominates, with maximum values at about $y = -200\,\mathrm{m}$ in case SP_LL27 (Fig. 4.3a). This general pattern seems to be influenced by buildings, since for the case SP_LL27_norog (Fig. 4.3b) without orography but including buildings the pattern is similar, but the gradients are smaller and the pattern is more smooth. If buildings are not considered (case SP_LL27_nobuild, Fig. 4.3c), the North-South gradient divides the pattern in two regions.

The differences in the pattern of snow on ground can be partly explained by the height of the low-level jet. The low-level jet develops at the top of the boundary layer, because momentum is accumulated there (Ferner et al., 2023, Section 3.5.3). Buildings induce vertical mixing, which enhances the boundary layer and affect the vertical location of the low-level jet. Its direction and intensity depends also on the incoming flow. In Fig. 4.4, the low-level jet is shown for SP_LL27, SP_LL27_norog, and SP_LL27_nobuild by depicting the normalised wind speed using the initial wind speed for normalisation (Tab. 4.1). Without

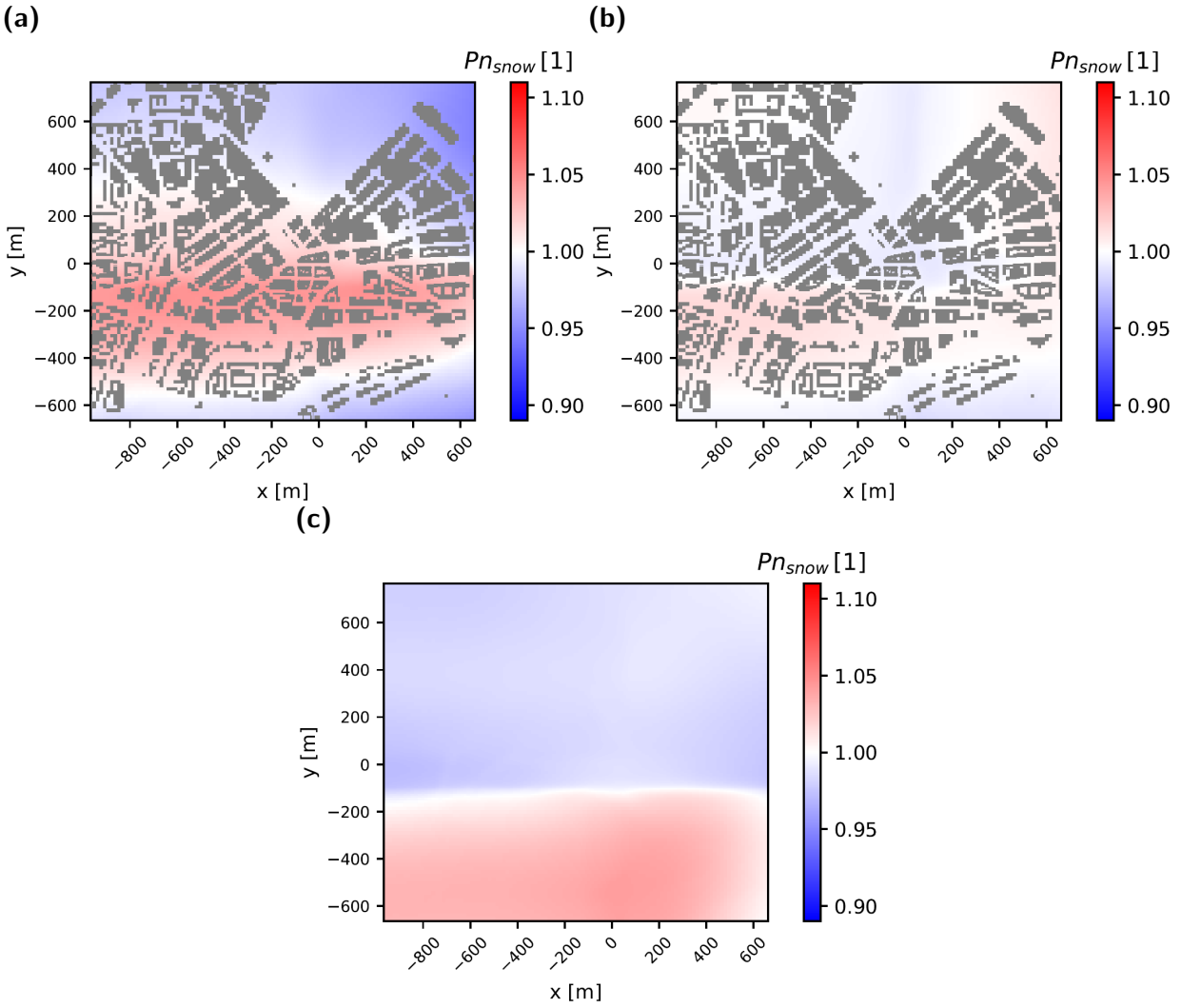

Figure 4.3: Horizontal cross sections of the normalised snow amount on ground accumulated between 8:35:00 and 9:00:00 LST for (a) SP_LL27, (b) SP_LL27_norog, and (c) SP_LL27_nobuild. *Pn*_snow is calculated as deviation from the area weighted mean of the snow amount.

building induced turbulences and resulting vertical mixing, the low-level jet develops differently as can be seen for SP_LL27_nobuild (Fig. 4.4c), where the low-level jet is located near the ground surface. For SP_LL27_norog, the low-level jet is located right below cloud base height at 250 m (Fig. 4.4b), while for SP_LL27, the low-level jet reaches the cloud base (Fig. 4.4a).

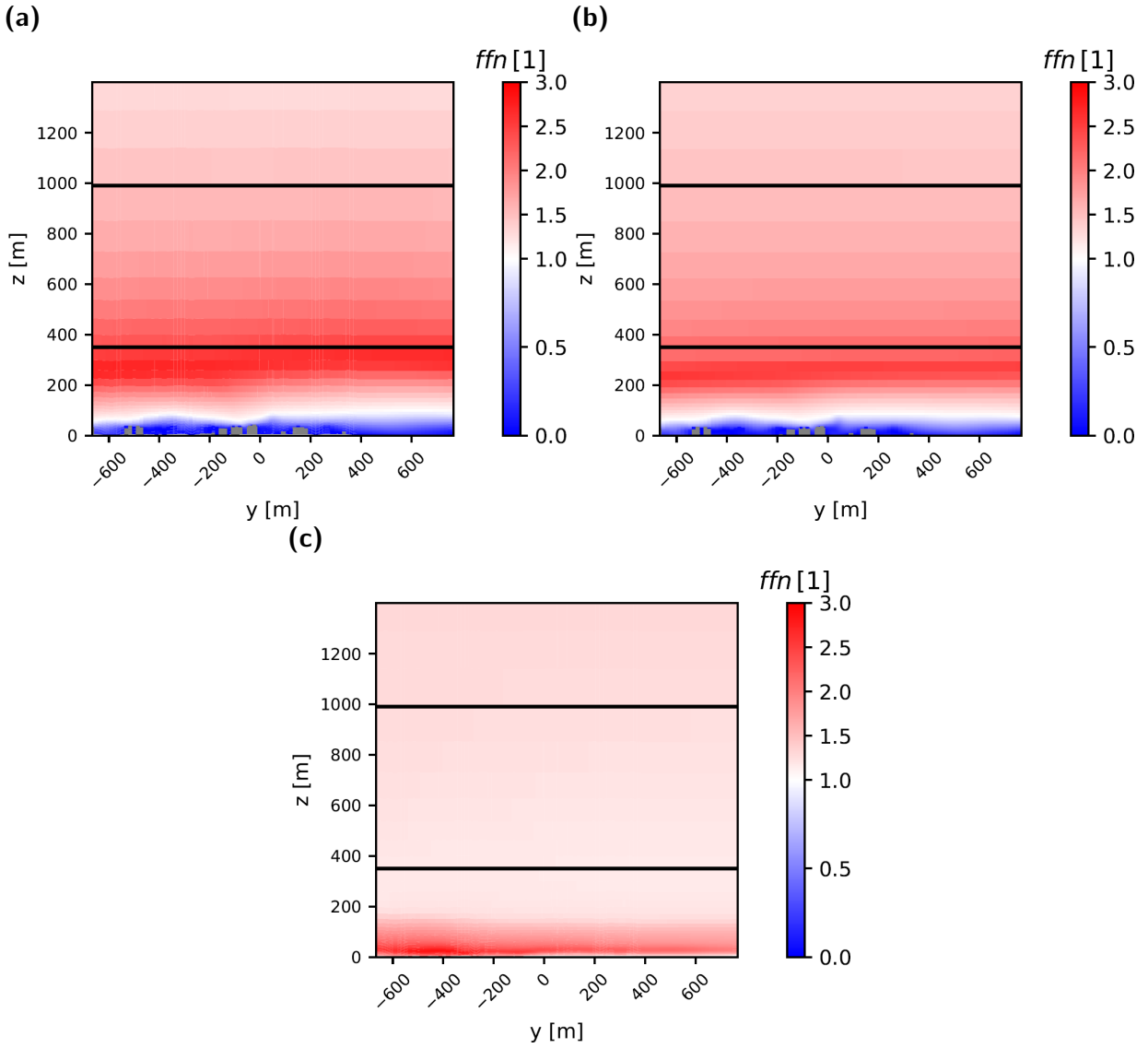

Figure 4.4: Vertical cross sections with south to the left at $x = -108$ m of the normalised wind speed ffn with initial value ff_init at 8:29:59 LST for (a) SP_LL27, (b) SP_LL27_norog, and (c) SP_LL27_nobuild. The black lines denote the location of the cloud base and cloud top height.

The effect of building induced vertical winds on precipitating snow is stronger than on rain,

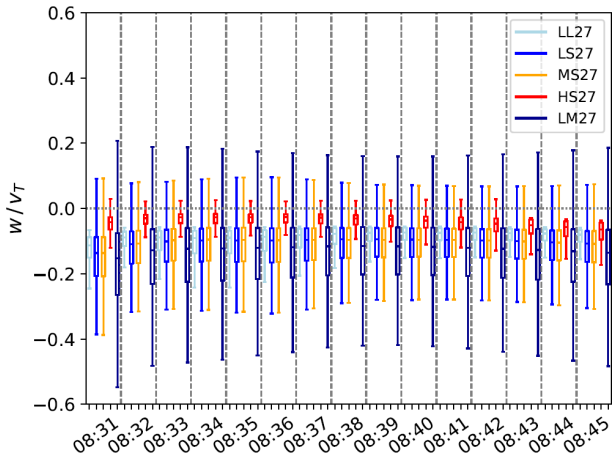

Figure 4.5: Vertical wind velocity w divided by the sedimentation velocity v_T (v_{TR} or v_{TS}) for the obstacle layer (from surface to 150 m) for SP_LL27, SP_LS27, SP_MS27, SP_HS27 and SP_LM27.

due to the different sedimentation speeds. For both, sedimentation remains more influential than vertical winds as can be seen for SP_LL27, SP_LS27, SP_MS27, SP_HS27 and SP_LM27 in the quotients of the vertical wind velocity and the sedimentation velocity (Fig. 4.5). The quotients are calculated for the obstacle layer from surface to 150 m above ground. They are positive for upward vertical winds and negative for downdraughts. Only quotients between -0.6 and $+0.2$ occur, which means that the sedimentation velocity reaches higher values than the vertical wind velocity. Note that the sedimentation velocity is always positive, even though it is always directed downward. An upward transport of rain droplets or snow does not occur in the spatial average as no quotients above one are found in Fig. 4.5. Positive values below one indicate an updraught, but rain and snow is still transported downwards. Precipitation is usually pushed downwards by the vertical wind as shown by the negative values of the quotient (Fig. 4.5). This is especially true for cases, where the sedimentation speed is smaller as found for snow (SP_LL27, SP_LS27, SP_MS27, SP_ML27) compared to the higher values for rain (SP_HS27). The extend to which rain is pushed down by the vertical wind is lower than for snow due to the larger sedimentation velocity yielding smaller absolute values of the quotients (compare SP_HS27, red, with the other cases). With larger

initial wind speeds, stronger vertical winds are induced leading to more occurrences of higher absolute quotient values as well as to a greater spread of values in case SP_LM27 compared to SP_LS27 and SP_LL27.

4.4.3 Surface influences on snow patterns

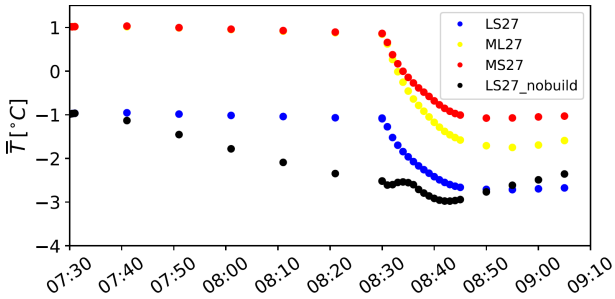

Figure 4.6: Time series of the spatial mean of the absolute temperature above ground $\overline{T}$ for SP_LS27, SP_ML27, SP_MS27, and SP_LS27_nobuild.

In cases with a medium initial temperature of 1 °C (SP_ML27, SP_MS27), it is warm enough for snow on ground to melt and evaporate but also cold enough for precipitating snow to form in the atmosphere. Due to temperature heterogeneities caused by obstacles and water surfaces, heterogeneities of snow melt are expected. The temperature above ground is influenced by the wind as well as processes related to precipitation. The latter can be seen in Fig. 4.6, which is the time series of the mean temperature at the lowest model level (1.75 m above ground) for cases SP_LS27, SP_ML27, SP_MS27, and SP_LS27_nobuild. Before the onset of precipitation at 8:30:00 LST, the temperature slightly decreases. The decrease is more pronounced for SP_LS27_nobuild (black circles), because the vertical mixing is smaller without buildings, the surface cooling is thus more pronounced resulting in lower temperatures and higher wind speed near ground without buildings (see the normalised wind speed for SP_LL27_nobuild in Fig. 4.4c). After the onset of precipitation at 8:30:00 LST, the temperature drops due to evaporation. This temperature drop is more pronounced for warmer cases (red and yellow circles) as a warmer atmosphere can take up more water. For

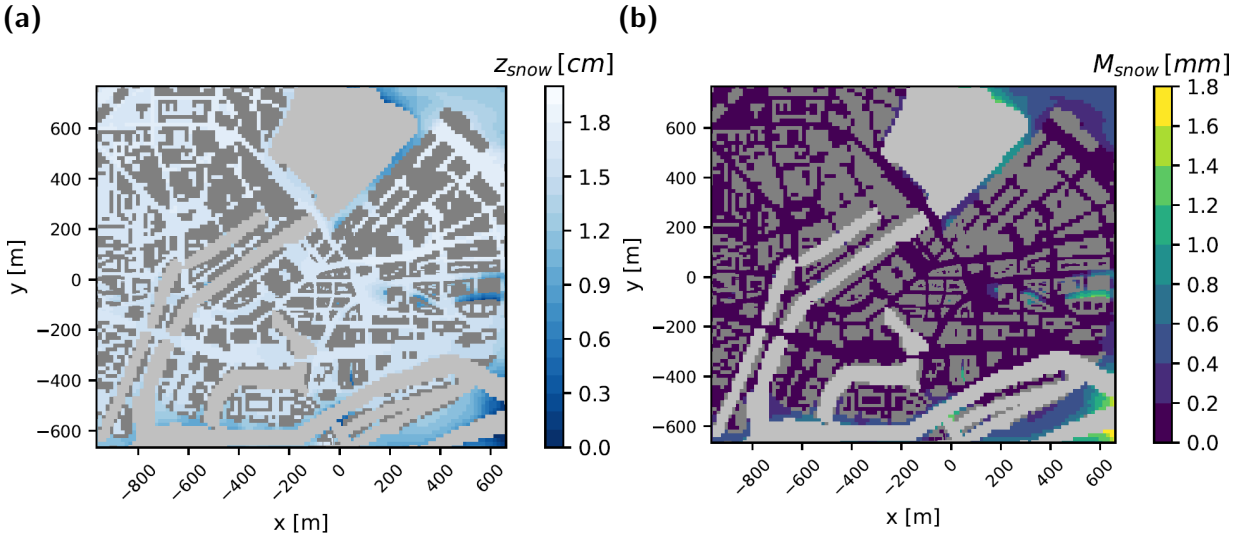

Figure 4.7: Horizontal cross sections of (a) the snow height z_{snow} and (b) the amount of melted snow water equivalent M_snow at 9:00:00 LST for SP_MS27. Light grey denotes water surfaces and dark grey denotes buildings.

the medium temperature cases (SP_MS27 and SP_ML27), where the initial temperature is 1 °C, the temperature drops from +0.9 °C to below the freezing point (−1.0 °C and −1.9 °C).

With temperatures around freezing point, heterogeneities in snow melt are expected. The accumulated snow amount (P_{snow}) does not include melted or evaporated snow. Those processes are considered in the snow water equivalent SWE (Eq. 4.1), which is the amount of snow left. Both P_{snow} and SWE are water equivalents. The snow height z_{snow} can be assumed as 10 times SWE (Eq. 4.2) and is given for SP_MS27 at 9:00:00 LST in Fig. 4.7a. The snow height is minimal near water surfaces and in a few street canyons, for instance at at $x = 511\,\text{m}$ and $y = -70\,\text{m}$ (Altstädter Straße). The snow height heterogeneities are mainly caused by snow melt. The amount of snow water equivalent, that has melted, can be estimated by calculating the difference of P_{snow} and SWE and is provided in Fig. 4.7b. High values of snow melt can be found at the locations with low snow heights.

The temperature drop due to evaporation occurs near ground causing a surface cooling except on water surfaces. As a consequence, the temperature drop is less pronounced above water surfaces. In cases with air temperatures around the freezing point (MS27 and ML27),

this leads to snow melt near water surfaces (Fig. 4.7b).

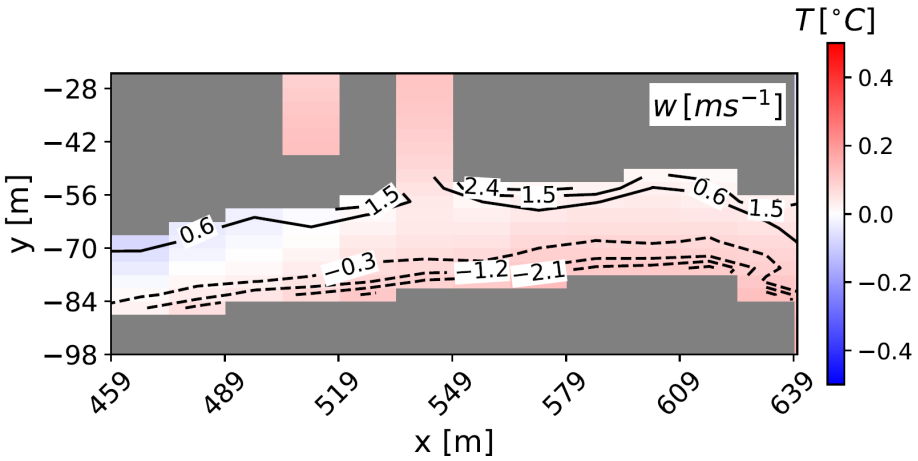

Figure 4.8: Horizontal cross section of the temperature T (colours) and vertical velocity w (upwinds solid lines, downwinds dashed lines) at Altstädterstraße for SP_MS27 at 14 m height at 8:40:00.

Warmer air can be transported to the ground by street canyon circulations causing snow melt. In case SP_MS27, the snow melt at the Altstädterstraße ($x = 511\,\text{m}$, $y = -70\,\text{m}$ in Fig. 4.7a) is caused by such a phenomenon. The circulation pattern and temperature transport for this street is shown in Fig. 4.8 for SP_MS27 at 14 m above ground at 8:40:00. The colours denote the temperature, which is mostly above freezing point. The vertical wind velocity is plotted with downdraughts as dashed lines. At the northern side of the street, cold air is transported upward and on the southern side warm air from above downward causing snow melt in this street in cases SP_MS27 and, because of the lower initial wind speed, to a lesser extend in SP_ML27 (not shown). Both water surfaces and circulation patterns on the building scale have an effect on the local temperature and consequently on snow melt and should therefore be taken into account, when investigating frost heterogeneities.

4.5 Conclusions

In this study, the influence of the topography on the heterogeneity of snow was investigated using the microscale, obstacle-resolving atmospheric model MITRAS (Salim et al., 2018)

using the one-category ice scheme and a snow cover scheme by Samsel et al. (2025, Chapter 2). Numerical simulations with different initial wind speeds, temperatures, precipitation amounts were performed for the city centre of Hamburg, Germany. The heterogeneity of the accumulated snow amount and the snow water equivalent and reasons for differences were assessed.

For rain, Ferner et al. (2023, Chapter 3) already found that consideration of a city's geometry and initial meteorology are crucial for a realistic simulation of precipitation within urban areas. In the current study, findings previously derived for rain are confirmed for snow. There are nonlinear effects induced by buildings and orography, that are only resolved when considering both orography and buildings. It has furthermore been shown that distinguishing between snow and rain improves model realism by considering the different sedimentation speeds. Furthermore, even at the short time scales considered here, melting and freezing play a role, especially for temperatures around 0 °C. The temperature differences are a result of building induced vertical advection which causes warmer air from above the canopy to reach the surfaces and start a melting process. Due to the circulation within a street canyon the resulting cooler air is advected to the other side of the canyon and with the updraught it is transported to above the canopy. This underlines that the city's geometry as well as melting and freezing processes should be taken into account when investigating heterogeneities in rain and snow patterns in urban areas. This confirms on the obstacle resolving scales results for impacts of the city's geometry on rain patterns (Zhang et al., 2022; Lu et al., 2024).

Local influences by buildings on the precipitation pattern were mostly recognisable in parts of the model domain, where the buildings are well resolved and during the forcing phase (i.e. when only the wind field below cloud base height is considered and the snow amount is low). To limit the computational demands, the model domain used in this study features a non-uniform grid with decreasing resolution towards the edges. Precipitation heterogeneities due to building induced winds were found in areas with high resolution but also in areas with

coarser resolution.

Identifying heterogeneities of snow melt is a first step towards determining frost heterogeneities within an urban neighbourhood, which could in a next step allow for planning precautionary measures to increase pedestrian comfort and traffic safety. It has been shown that temperature variations between and close to buildings are caused by both the presence of water surfaces and building induced wind fields close to and between buildings. Performing simulations with common meteorological conditions for urban neighbourhoods can contribute to, for instance, identifying icy conditions.

Detailed data on the urban meteorological conditions within the canopy layer are still not available but needed for a quantitative evaluation of such complex obstacle-resolving models. Currently, the effects of human activity such as winter services and traffic are only included rudimentary in the model (Samsel et al., 2025, Section 2.5) but are shown to have an impact on the ability of models to represent snow on roads (Lemonsu et al., 2010). If information is available, the effects of e.g. winter services could be considered in the model. Furthermore, there is an effect of snow cover on roofs on urban surface air temperature (Mori and Sato, 2015), which is not represented in the model as only the snow amounts on roofs are calculated without its effect on its surroundings.

5 Conclusions

In this thesis, the microscale, obstacle-resolving atmospheric model MITRAS was extended with a winter precipitation scheme to enable investigations of urban effects on winter precipitation for a warm temperate climate city. The model was applied for the first time for analyses of precipitation heterogeneities within an urban neighbourhood. The aim was to assess **what model complexity is needed for a realistic representation of a winter event within a warm temperate climate city** – the guiding research question of this work. Before the guiding research question is addressed in Section 5.4, the three subsidiary research questions are discussed:

RQ 1: What model complexity is needed for a winter precipitation scheme in a microscale obstacle-resolving model? (Section 5.1)

RQ 2: How to validate a winter precipitation scheme without high-resolution measurement data? (Section 5.2)

RQ 3: How do obstacles influence precipitation heterogeneities within an urban neighbourhood? (Section 5.3)

5.1 A winter precipitation scheme for a microscale, obstacle-resolving model

Based on the scale of the model, the intended use cases, and the already existing parameterisations, suitable methods for the inclusion of cloud microphysics processes and of snow cover were chosen for MITRAS. The model uses a fine grid of $\mathcal{O}(1\,\mathrm{m})$ to resolve obstacles with resulting time steps of $\mathcal{O}(10^{-2}\,\mathrm{s})$. The high spatial and temporal resolution necessitates

to explicitly resolve the sedimentation of rain and snow. The intended use cases do not include the realistic representation of cloud formation, which would be necessary for weather forecasting or the analysis of precipitation modification by large urban areas. Instead, the goal of this thesis was to analyse urban effects on a building to neighbourhood scale for model domain sizes of $\mathcal{O}(1\,\mathrm{km}^2)$ and for precipitation from clouds, that were already present. This allowed for the implementation of a comparably simple cloud microphysics parameterisation. A mesoscale counterpart to MITRAS called METRAS exists, which already includes a Kessler-type three-category bulk water-continuity model designed for warm clouds (Köhler, 1990; Schlünzen et al., 2018a) as well as a snow cover scheme (Boettcher, 2017), where a single snow layer is assumed without the consideration of snowdrift. Therefore, the pre-existing parameterisations of METRAS were adjusted for MITRAS to take into account the specific scales and resolved obstacles as well as the urban effects and precipitating snow.

Since clouds in winter include an ice phase, applying a scheme designed for warm clouds does not seem fitting. But, with considering only warm clouds for a winter situation, the profound influence of clouds on radiation is represented. This can be seen when comparing simulations with and without precipitation applying the warm rain scheme. The comparison yielded no agreement (hit rates of 0 %) for temperature and radiation. The level of detail is further increased by applying a one-category ice scheme, where the one ice category is snow water content and the cloud microphysics processes are adjusted to better represent mixed-phase clouds. The overestimation of precipitation which occurs in the warm rain scheme (Schlünzen et al., 2018a) has been shown to be reduced by using this one-category ice scheme.

The urban impact on snow cover was included by adjusting the albedo of snow and by including snow removal practices by assuming that below 50 cm snow height, the underlying soil shines through using a linear relation. The homogenising effect of snow on the albedo on ground is well represented, which was shown by comparing simulations with and without

snow. The median of the albedo of a domain increases in case of snow cover while the spread of the albedo values decreases compared to a simulation without snow.

5.2 Validation of the winter precipitation scheme

The performance of the winter precipitation scheme is tested for plausibility by comparing model results of different model versions. The assessment using different model versions is suitable, because results of previous model versions have already been validated and the parameterisation schemes are well established. To compensate for the fact that no measurement data, physical model results or results from other numerical models than MITRAS are available for the comparison, and to better detect programming errors, a strict criterion for the comparison was applied. As validation metric, hit rates are chosen following a well-established guideline for the assessment of microscale, obstacle-resolving models (VDI, 2017). For each quantity, threshold values for compared data values to be considered a hit are defined. For the wind components, the values are based on VDI (2017) yielding a threshold of $0.02\,\mathrm{ms}^{-2}$ (5 %). For temperature, long wave and short wave radiation, and precipitation, threshold values were derived based on computational accuracy, which leads to a similarly strict criterion: 0.05 K (0.02 %), $0.5\,\mathrm{Wm}^{-2}$ (0.5 %), $0.5\,\mathrm{Wm}^{-2}$ (0.2 %), and 0.001 mm (1 %).

The comparisons yield plausible results with expected differences caused by the new parameterisations or the neglect of other influences. For instance, neglecting the terrain steepness leads to differences in grid cells near ground, where the largest orographic effects occur. The hit rate for the wind field components therefore is below 95 %, meaning, both results are not identical. However, the smallest hit rate is 83 %, which is still quite high considering the strictness of the criterion. The strict criterion emphasises small differences, which can be seen in the comparison of the precipitation amounts on ground using the ice and warm rain scheme. The hit rates for precipitation for the comparison of cases Hice and Hwr and Wice

and Wwr are 48 % and 60 %, meaning, they are not identical. Basing the required accuracies on WMO (2023a), however, would yield hit rates of 100 %.

5.3 Influence of urban areas on precipitation heterogeneities within an urban neighbourhood

Sensitivity studies were performed for various meteorological situations and topographies using the warm rain scheme (Chapter 3) and the winter precipitation scheme (Chapter 4). Regardless which precipitation scheme was applied, the precipitation pattern on ground is heavily influenced by buildings and orography. High-reaching effects of the buildings alter the low-level jet, that developed due to momentum accumulation above the urban boundary layer. The shape and location of the low-level jet then influence the precipitation pattern on ground leading to, at first glance, contradicting findings. A higher heterogeneity of the accumulated precipitation amount on ground is expected in simulations, that consider buildings. For instance, the heterongeneity of case RH_MM27nobuild, that does not consider buildings, is 0.3 %. The corresponding cases, that consider buildings (RH_MM27norog) and orography and buildings (RH_MM27) both achieve higher heterogeneity values (1.8 % and 1.9 %). However, in cases of SP_LL27, SP_LL27_norog, and SP_LL27_nobuild, a case that considers buildings, yielded the lowest heterogeneity value (0.7 % for SP_LL27_norog vs. 2.6 % for SP_LL27 and 2.1 % for SP_LL27_nobuild). The found higher heterogeneity in case SP_LL27_nobuild was the result of a higher gradient in the precipitation pattern, which was caused by the shape and location of the low-level jet. The comparison of cases with and without buildings and orography revealed non-linear effects, that are only represented when both buildings and orography are considered. Not only the presence of buildings but also the position of buildings is influential. This is shown by comparing cases RH_MM27 and RH_MM23, which differ by their initial wind directions (270 ° and 230 °, respectively). Rain patterns at ground are considerably different.

Urban effects on precipitation heterogeneity are more pronounced for snow due to the lower sedimentation speed of snow compared to rain. On a building scale, variations of the snow pattern on ground were recognisable in areas, where the flow and snow transport was resolved.

For rain, variations on a building scale were only visible during the forcing phase, i.e. when only the processes below cloud base height were considered. Urban effects on snow cover became most visible in the form of snow melt heterogeneities. The initial temperature in cases SP_MS27 and SP_ML27 was low enough for snow to develop and high enough to allow snow melt, which was especially pronounced in areas influenced by water surfaces and within a street canyon. A street canyon circulation developed, transporting warmer air downward from above the buildings, which reduces the surface cooling by evaporation during precipitation.

5.4 Necessary model complexity for a realistic representation of a winter event

The representation of a winter event of a warm temperate climate city requires a numerical model to simulate rain and snow heterogeneities, that are caused by urban impacts on a building to neighbourhood scale. For instance, urban heat affects the phase of precipitation (i.e. solid or liquid) and buildings influence the surface roughness, which modifies the precipitation pattern on ground. Snow cover within urban areas tends to be more patchy and darker compared to rural areas. In order to represent these features in a numerical model, the building structure and orography should be resolved and a cloud microphysics parameterisation should be applied, that considers the sedimentation speeds of precipitation in liquid and solid phase. Furthermore, the effects of water surfaces should be considered.

It was shown that high-reaching effects of buildings are of greater influence on the precipitation pattern on ground than the effects of building induced winds on a building scale especially in case of rain. Buildings should be considered mainly due to their effect on the

height and shape of the boundary layer. Therefore, buildings should be resolved in order to capture the effect of city structure on the cloud. The cloud formation processes can be neglected for simulations on a neighbourhood scale. It is sufficient to prescribe clouds as has been done for the sensitivity studies in this thesis. Studies have shown that there are synergetic effects of orography, buildings and meteorological conditions (Zhang et al., 2022; Lu et al., 2024). In this work, those non-linear effects are confirmed for the neighbourhood scale. This underlines the importance of taking the city structure into account when investigating urban impacts on precipitation – also when urban areas are parameterised in applications on a larger scale.

Variations in the rain and snow distribution on ground on the building scale were simulated and occur more often in case of snow than in case of rain. Resolving the different sedimentation speeds for snow and rain allows for the simulation of the effects of building induced winds on the building scale. Mainly, snow heterogeneities are caused by the effect of local circulation patterns and of water surfaces on snow melt. Considering snow melt heterogeneities is a first step towards the representation of frost heterogeneities.

Limitations of this winter parameterisation are that human activities are only crudely included. The albedo on roofs is not adjusted to the presence of snow and snow clearing is not explicitly resolved. Both are shown to be relevant factors for the albedo in a city (Shui et al., 2019). It would furthermore be advisable to include additional urban effects on temperature. For instance, considering the effect of traffic has been shown to improve the simulation of road surface temperatures (Khalifa et al., 2016). Also the heat emission of buildings (Dobre et al., 2017) or of infrastructure below ground (i.e. pipes) could affect temperature heterogeneities on ground.

With this work, the foundation was build for creating high-resolution numerical model data suitable for various investigations of climate change related impacts in urban areas in winter. In the future, questions concerning human comfort or the performance of adaptation

measures designed for summer in winter can be addressed for the building and neighbourhood scale.

Acknowledgements

Nach fast sieben Jahren habe ich es endlich geschafft und diese Doktorarbeit eingereicht. Das ging nicht ohne die tatkräftige Unterstützung vieler Menschen, denen hier gedankt werden soll.

Als erstes möchte ich Prof. Dr. Heinke Schlünzen für ihre exzellente Betreuung danken. Danke, dass du den gesamten Weg begleitet hast. Jedes Treffen hat mich weitergebracht und deine Ratschläge waren jedes Mal wertvoll. Sogar in deinem wohlverdienten Ruhestand kümmerst du dich noch rührend um deine Doktorandinnen.

Auch meinem Zweitbetreuer, Dr. Kevin Sieck, und meinem Panel Chair, Prof. Dr. Bernd Leitl, möchte ich danken. Mit eurer Unterstützung war es mir möglich, dieses umfangreiche Projekt doch zu meistern und zu Ende zu bringen.

Im Anhang befinden sich zu jedem Paper Acknowledgements, die den Satz beinhalten, dass diese Arbeit als Teil des WINTER Projekts durch das HICSS finanziert wurde. Während ich also dem Modell das Schneien beigebracht habe, hat sich Dr. Louisa Bell das winterliche Klima in Hamburg mal genauer angesehen und Dr. Alexander Voigt hat das Modell beschleunigt. Louisa, liebe WINTER-Schwester, den Dank für zahlreiche Kaffeepausen und wertvollen Austausch gebe ich gerne zurück! Alex, ich habe gerne die Büros mit dir geteilt!

Ich bedanke mich auch bei den Mitarbeiterinnen und Mitarbeitern des GERICS, die ich lange Zeit als meine Kolleg*innen bezeichnen durfte. Es war mir eine Ehre, Teil dieses Instituts sein zu dürfen.

Danke auch an die aktuellen und ehemaligen MeMis der Uni Hamburg: Dr. Ronny Badele, Dr. Marita Boettcher, Dr. Ge Cheng, Christian Dix, Dr. David Grawe, Dr. Jana Fischereit, Dr. Franziska Hanf, Mailin Samland, Dr. Malte Uphoff, Dr. Alexander Voigt und Vivien Voss. Marita hat mich fachlich so sehr unterstützt, eigentlich müsste ihr Name oben bei den Betreuenden aufgeführt werden. Ähnliches gilt für David. Seine technische und inhaltliche

Unterstützung haben maßgeblich zum Erfolg dieser Arbeit beigetragen.

Besonderer Dank gilt Vivien, die nicht nur eine MeMi ist, sondern auch eine meiner engsten Freundinnen. Vermutlich muss ich an dieser Stelle auch der Doktorarbeit danken, denn ohne sie hätte ich mich nicht in zahlreichen Mittagspausen so sehr mit Vivien angefreundet, dass ich sie zu meiner Trauzeugin gemacht habe. Vivien, danke für die schöne gemeinsame Zeit!

Generell muss meinem sozialen Umfeld gedankt werden, denn – das ist kein Scherz – eine Doktorarbeit zu schreiben ist manchmal ein bisschen stressig. Deswegen bedanke ich mich und bitte um Entschuldigung bei Matthias Samsel, meinem Mann (ich muss da immer noch kichern $\wedge\wedge$). Nicht nur hat er Teile dieser Fan Fiction über Schneemodellierung beta gelesen, er hat mich auch geheiratet. Wie wird unsere Ehe wohl laufen ohne die Dissertation im Nacken? Dank geht auch an meine Eltern, Christa und Jürgen, weil sie immer für mich da sind. Meinen Verstand habe ich von euch! Meine Großeltern möchte ich an dieser Stelle auch dankend erwähnen, allen voran meinen Opa Willy, der einen großen Teil der Arbeit noch miterlebt hat. Vielen Dank an meine Schwiegereltern, Kathrin und Holger, dass ihr mich in die Familie aufgenommen habt. Zuletzt möchte ich dem Pfadfinder*innenstamm Santa Lucia danken. Unsere jährlichen Sommerlager sind – ähnlich wie die Doktorarbeit – anstrengend und organisatorisch aufwändig, bringen aber auch viel Freude und sorgen dafür, dass man sich stetig weiterentwickelt. Der Pfadfinder ist allzeit bereit: gut Pfad!

A Supporting information to Chapter 2

A.1 Statements on submitted manuscript

A.1.1 Code availability

Currently the MITRAS source code is distributed upon request under the terms of a user agreement with the Mesoscale and Microscale Modeling (MeMi) working group at the Meteorological Institute, University of Hamburg (https//www.mi.uni-hamburg.de/memi). A copy of the user agreement is available upon request. Due to current copyright restrictions, users are requested to contact the corresponding authors to obtain access to the code free of charge for research purposes under a collaboration agreement (metras@uni-hamburg.de).

Documentation for the M-SYS model system (Schlünzen et al., 2018a,b), in which MITRAS is included, is available online at https://www.mi.uni-hamburg.de/memi under "Numerical Models". A detailed description of MITRAS version 2 can be found in Salim et al. (2018).

The initialisation profiles for the model runs can be found in the supplement of this article (Appendix A.1.5). The scripts used for the analyses in this paper are archived on Zenodo (https://doi.org/10.5281/zenodo.14269493, Samsel (2024)).

A.1.2 Author contributions

KSS organised the paper and collected the contributions. HS coordinated the model development since the beginning and is with DG overall responsible for the model and its documentation. MB developed the snow cover parameterisation in the mesoscale model METRAS and provided KSS with code and help. KS contributed to the introduction. All authors reviewed and edited the paper.

A.1.3 Competing interests

The authors declare that they have no conflict of interest.

A.1.4 Acknowledgements

This work was financed within the framework of the Helmholtz Institute for Climate Service Science (HICSS), a cooperation between Climate Service Center Germany (GERICS) and University Hamburg, Germany, and conducted as part of the WINTER project (Investigating climate change related impacts on the urban winter climate of Hamburg). This work was partly funded by the Deutsche Forschungsgemeinschaft (DFG, German Research Foundation) under Germany's Excellence Strategy – EXC 2037 'CLICCS – Climate, Climatic Change, and Society' – Project Number: 390683824. The work contributes to the Center for Earth System Research and Sustainability (CEN) of University of Hamburg.

A.1.5 Supplement

Table A.1: Initialisation profiles for cases Winit and Wwr_noprecip

z	u [ms^{-1}]	v [ms^{-1}]	θ [K]	p_0 [hPa]	ρ_0 [kgm^3]	q_1^1 [kgkg^{-1}]	q_1^{2c} [kgkg^{-1}]
1.5	0.6294	0.3303	280.81	989.82	1.2288	0.0037377	0.0
4.5	0.8676	0.4366	280.81	989.46	1.2285	0.0037314	0.0
7.5	1.0135	0.4924	280.81	989.1	1.2282	0.0037251	0.0
10.5	1.1195	0.527	280.81	988.73	1.2278	0.0037187	0.0
13.5	1.2045	0.5504	280.82	988.37	1.2275	0.0037124	0.0
16.5	1.277	0.5669	280.82	988.01	1.2272	0.0037061	0.0
19.5	1.3415	0.5785	280.82	987.65	1.2269	0.0036998	0.0
22.5	1.4003	0.5863	280.83	987.29	1.2265	0.0036936	0.0

25.5	1.4549	0.5912	280.83	986.93	1.2262	0.0036873	0.0
28.5	1.5065	0.5934	280.83	986.57	1.2259	0.003681	0.0
31.5	1.5545	0.5933	280.83	986.21	1.2255	0.0036748	0.0
34.75	1.6042	0.591	280.84	985.82	1.2252	0.003668	0.0
38.55	1.6606	0.5852	280.84	985.36	1.2248	0.0036601	0.0
43.0	1.7232	0.5747	280.85	984.83	1.2243	0.0036509	0.0
48.2	1.7924	0.5575	280.85	984.2	1.2237	0.0036401	0.0
54.3	1.868	0.5308	280.86	983.47	1.223	0.0036275	0.0
61.5	1.9504	0.4904	280.86	982.61	1.2223	0.0036127	0.0
70.0	2.0361	0.4312	280.87	981.59	1.2213	0.0035953	0.0
80.0	2.1204	0.3454	280.88	980.39	1.2202	0.0035749	0.0
91.75	2.1875	0.2289	280.89	978.98	1.219	0.0035511	0.0
105.55	2.2093	0.0692	280.91	977.33	1.2174	0.0035232	0.0
121.75	2.0164	−0.0467	280.92	975.4	1.2157	0.0034908	0.0
140.8	1.9989	−0.0007	280.94	973.13	1.2136	0.003453	0.0
163.2	2.0	−0.0	280.96	970.47	1.2112	0.003409	0.0
189.5	2.0	−0.0	280.99	967.35	1.2083	0.0033579	0.0
220.4	2.0	−0.0	281.02	963.69	1.205	0.0032987	0.0
256.7	2.0	−0.0	281.06	959.4	1.201	0.0032303	0.0
299.35	2.0	−0.0	281.1	954.39	1.1964	0.0031515	0.0
349.5	2.0	0.0	281.15	948.52	1.191	0.0030609	0.0
408.45	2.0	0.0	281.2	941.65	1.1847	0.0029573	0.0
477.7	2.0	0.0	281.27	933.62	1.1772	0.0028393	0.0

559.05	2.0	0.0	281.35	924.26	1.1686	0.002706	0.0
654.65	2.0	0.0	281.45	913.35	1.1584	0.002556	0.0
767.0	2.0	−0.0	281.56	900.65	1.1465	0.0023889	0.0
899.0	2.0	−0.0	281.69	885.89	1.1327	0.0022046	0.0
1054.1	2.0	−0.0	281.84	868.78	1.1165	0.0020037	0.0
1236.35	2.0	−0.0	282.02	848.99	1.0977	0.0017877	0.0
1450.5	2.0	−0.0	282.24	826.16	1.0759	0.0015597	0.0
1702.15	2.0	−0.0	282.49	799.91	1.0506	0.0013241	0.0
1997.85	2.0	−0.0	282.78	769.86	1.0213	0.0010868	0.0
2345.3	2.0	−0.0	283.13	735.63	0.98754	0.00085568	0.0
2753.55	2.0	−0.0	283.54	696.86	0.94881	0.00063942	0.0
3224.1	2.0	−0.0	284.01	654.07	0.90539	0.00045035	0.0
3724.1	2.0	−0.0	284.51	610.76	0.86068	0.00030461	0.0
4224.1	2.0	−0.0	285.02	569.61	0.81743	0.00020182	0.0
4724.1	2.0	−0.0	285.52	530.55	0.77562	0.00013077	0.0
5224.1	2.0	−0.0	286.03	493.5	0.73524	$8.2699e-05$	0.0

Table A.2: Initialisation profiles for case Wwr, Wwr_np, and Wice

z	u [ms^{-1}]	v [ms^{-1}]	θ [K]	p_0 [hPa]	ρ_0 [kgm^3]	q_1^1 [kgkg^{-1}]	q_1^{2c} [kgkg^{-1}]
1.5	0.6165	0.338	280.81	989.82	1.2538	0.0037377	0.02
4.5	0.8516	0.4476	280.81	989.45	1.2535	0.0037314	0.02
7.5	0.9973	0.5059	280.81	989.08	1.2532	0.0037251	0.02
10.5	1.1044	0.5425	280.82	988.71	1.2528	0.0037188	0.02
13.5	1.1913	0.5675	280.82	988.34	1.2525	0.0037126	0.02
16.5	1.2663	0.5852	280.82	987.97	1.2521	0.0037063	0.02
19.5	1.3338	0.5978	280.83	987.6	1.2518	0.0037	0.02
22.5	1.3959	0.6063	280.83	987.23	1.2514	0.0036938	0.02
25.5	1.454	0.6115	280.83	986.87	1.2511	0.0036875	0.02
28.5	1.5094	0.6137	280.84	986.5	1.2507	0.0036813	0.02
31.5	1.5611	0.6133	280.84	986.13	1.2504	0.0036751	0.02
34.75	1.6148	0.6101	280.84	985.73	1.25	0.0036683	0.02
38.55	1.6761	0.6028	280.85	985.27	1.2496	0.0036605	0.02
43.0	1.7442	0.5897	280.85	984.72	1.2491	0.0036513	0.02
48.2	1.8196	0.5682	280.86	984.08	1.2485	0.0036406	0.02
54.3	1.9015	0.5349	280.87	983.34	1.2478	0.003628	0.02
61.5	1.99	0.4841	280.88	982.46	1.247	0.0036133	0.02
70.0	2.0786	0.4101	280.89	981.42	1.246	0.0035959	0.02
80.0	2.1601	0.3012	280.9	980.19	1.2448	0.0035756	0.02
91.75	2.2086	0.1596	280.91	978.76	1.2435	0.0035519	0.02
105.55	2.1846	−0.0259	280.93	977.08	1.2419	0.0035242	0.02

121.75	2.0027	−0.0122	280.95	975.11	1.2401	0.0034919	0.02
140.8	2.0	−0.0002	280.97	972.79	1.2379	0.0034542	0.02
163.2	2.0	−0.0	281.0	970.07	1.2353	0.0034103	0.02
189.5	2.0	−0.0	281.03	966.89	1.2323	0.0033595	0.02
220.4	2.0	−0.0	281.06	963.16	1.2288	0.0033005	0.02
256.7	2.0	−0.0	281.11	958.79	1.2247	0.0032324	0.02
299.35	2.0	0.0	281.16	953.68	1.2199	0.0031538	0.02
349.5	2.0	0.0	281.22	947.69	1.2142	0.0030636	0.02
408.45	2.0	0.0	281.29	940.69	1.2076	0.0029603	0.02
477.7	2.0	0.0	281.37	932.51	1.1998	0.0028427	0.02
559.05	2.0	−0.0	281.47	922.97	1.1907	0.0027097	0.02
654.65	2.0	−0.0	281.58	911.85	1.1801	0.0025602	0.02
767.0	2.0	−0.0	281.71	898.92	1.1676	0.0023936	0.02
899.0	2.0	−0.0	281.87	883.89	1.1531	0.0022096	0.02
1054.1	2.0	−0.0	282.06	866.48	1.1356	0.002009	0.019459
1236.35	2.0	−0.0	282.27	846.37	1.114	0.0017933	0.017636
1450.5	2.0	−0.0	282.52	823.23	1.0889	0.0015653	0.015495
1702.15	2.0	−0.0	282.81	796.71	1.0601	0.0013294	0.012978
1997.85	2.0	−0.0	283.14	766.44	1.027	0.0010917	0.010021
2345.3	2.0	−0.0	283.52	732.06	0.99036	0.00085986	0.007698
2753.55	2.0	−0.0	283.96	693.24	0.94859	0.00064276	0.0049763
3224.1	2.0	−0.0	284.45	650.53	0.90214	0.00045281	0.0018393
3724.1	2.0	−0.0	284.96	607.42	0.85596	0.00030628	0.0

4224.1	2.0	−0.0	285.47	566.49	0.81295	0.00020293	0.0
4724.1	2.0	−0.0	285.97	527.64	0.77137	0.00013149	0.0
5224.1	2.0	−0.0	286.48	490.8	0.73121	$8.3154e-05$	0.0

Table A.3: Initialisation profiles for case Cwr and Cice

z	u [ms^{-1}]	v [ms^{-1}]	θ [K]	p_0 [hPa]	ρ_0 [kgm^3]	q_1^1 [kgkg^{-1}]	q_1^{2c} [kgkg^{-1}]
1.5	0.6036	0.342	272.78	989.81	1.292	0.0021123	0.02
4.5	0.8359	0.4538	272.79	989.43	1.2916	0.0021085	0.02
7.5	0.9813	0.5139	272.79	989.05	1.2913	0.0021047	0.02
10.5	1.0893	0.5519	272.79	988.67	1.2909	0.0021009	0.02
13.5	1.1779	0.578	272.8	988.29	1.2905	0.0020971	0.02
16.5	1.2551	0.5967	272.8	987.91	1.2902	0.0020934	0.02
19.5	1.3251	0.6099	272.8	987.53	1.2898	0.0020896	0.02
22.5	1.39	0.6189	272.81	987.15	1.2894	0.0020858	0.02
25.5	1.451	0.6242	272.81	986.77	1.2891	0.002082	0.02
28.5	1.5095	0.6263	272.81	986.39	1.2887	0.0020783	0.02
31.5	1.5642	0.6254	272.82	986.01	1.2883	0.0020745	0.02
34.75	1.6211	0.6215	272.82	985.6	1.2879	0.0020705	0.02
38.55	1.6864	0.6128	272.83	985.12	1.2875	0.0020657	0.02
43.0	1.759	0.5975	272.83	984.56	1.2869	0.0020602	0.02
48.2	1.8391	0.5725	272.84	983.9	1.2863	0.0020537	0.02
54.3	1.9261	0.5338	272.85	983.13	1.2855	0.0020462	0.02
61.5	2.0186	0.4751	272.85	982.23	1.2847	0.0020373	0.02
70.0	2.1101	0.3885	272.86	981.16	1.2836	0.0020269	0.02
80.0	2.1854	0.2642	272.88	979.9	1.2824	0.0020146	0.02
91.75	2.2083	0.0974	272.89	978.42	1.281	0.0020003	0.02
105.55	2.0603	−0.0648	272.91	976.69	1.2793	0.0019837	0.02

121.75	1.9988	−0.0014	272.93	974.66	1.2773	0.0019643	0.02
140.8	2.0	−0.0	272.95	972.27	1.275	0.0019416	0.02
163.2	2.0	−0.0	272.98	969.47	1.2722	0.0019153	0.02
189.5	2.0	−0.0	273.01	966.19	1.269	0.0018848	0.02
220.4	2.0	−0.0	273.04	962.35	1.2653	0.0018495	0.02
256.7	2.0	−0.0	273.09	957.85	1.2609	0.0018087	0.02
299.35	2.0	0.0	273.14	952.59	1.2557	0.0017618	0.02
349.5	2.0	0.0	273.2	946.43	1.2497	0.0017079	0.02
408.45	2.0	0.0	273.27	939.22	1.2426	0.0016465	0.02
477.7	2.0	0.0	273.35	930.81	1.2343	0.0015767	0.02
559.05	2.0	−0.0	273.45	920.99	1.2246	0.0014979	0.02
654.65	2.0	−0.0	273.56	909.56	1.2133	0.0014097	0.02
767.0	2.0	−0.0	273.7	896.26	1.2001	0.0013118	0.02
899.0	2.0	−0.0	273.85	880.82	1.1847	0.0012042	0.02
1054.1	2.0	−0.0	274.04	862.94	1.1661	0.0010875	0.019459
1236.35	2.0	−0.0	274.26	842.3	1.1431	0.00096297	0.017636
1450.5	2.0	−0.0	274.51	818.56	1.1167	0.00083243	0.015495
1702.15	2.0	−0.0	274.8	791.37	1.0862	0.00069873	0.012978
1997.85	2.0	−0.0	275.13	760.37	1.0513	0.00056565	0.010021
2345.3	2.0	−0.0	275.51	725.2	1.0126	0.00043778	0.007698
2753.55	2.0	−0.0	275.95	685.54	0.96855	0.00032024	0.0049763
3224.1	2.0	−0.0	276.45	641.96	0.91965	0.0002197	0.0018393
3724.1	2.0	−0.0	276.96	598.05	0.87107	0.0001442	0.0

4224.1	2.0	−0.0	277.46	556.44	0.82583	$9.2503e-05$	0.0
4724.1	2.0	−0.0	277.97	517.01	0.78216	$5.7892e-05$	0.0
5224.1	2.0	−0.0	278.47	479.69	0.74004	$3.5269e-05$	0.0

Table A.4: Initialisation profiles for cases Hwr and Hice

z	u [ms^{-1}]	v [ms^{-1}]	θ [K]	p_0 [hPa]	ρ_0 [kgm^3]	q_1^1 [kgkg^{-1}]	q_1^{2c} [kgkg^{-1}]
1.5	0.6332	0.3299	288.83	989.82	1.217	0.0063763	0.02
4.5	0.8721	0.4359	288.83	989.46	1.2167	0.0063662	0.02
7.5	1.0181	0.4914	288.84	989.1	1.2164	0.0063561	0.02
10.5	1.1238	0.5258	288.84	988.75	1.2161	0.006346	0.02
13.5	1.2081	0.5491	288.84	988.39	1.2157	0.006336	0.02
16.5	1.2799	0.5654	288.85	988.03	1.2154	0.0063259	0.02
19.5	1.3435	0.5769	288.85	987.67	1.2151	0.0063159	0.02
22.5	1.4013	0.5848	288.85	987.32	1.2148	0.0063059	0.02
25.5	1.4549	0.5897	288.86	986.96	1.2145	0.0062959	0.02
28.5	1.5053	0.5921	288.86	986.6	1.2141	0.0062859	0.02
31.5	1.5523	0.5923	288.86	986.24	1.2138	0.0062759	0.02
34.75	1.6008	0.5902	288.87	985.86	1.2135	0.0062651	0.02
38.55	1.6558	0.585	288.87	985.4	1.2131	0.0062525	0.02
43.0	1.7167	0.5752	288.88	984.88	1.2126	0.0062378	0.02
48.2	1.7839	0.5591	288.88	984.26	1.212	0.0062206	0.02
54.3	1.8575	0.5339	288.89	983.53	1.2114	0.0062005	0.02
61.5	1.9373	0.4957	288.9	982.68	1.2106	0.0061768	0.02
70.0	2.0212	0.4387	288.91	981.67	1.2097	0.006149	0.02
80.0	2.1016	0.3573	288.92	980.48	1.2086	0.0061164	0.02
91.75	2.1667	0.2414	288.93	979.09	1.2074	0.0060782	0.02
105.55	2.1845	0.0924	288.95	977.46	1.2059	0.0060337	0.02

121.75	2.0839	−0.067	288.97	975.54	1.2042	0.0059818	0.02
140.8	1.9989	−0.0011	288.99	973.29	1.2021	0.0059212	0.02
163.2	2.0	−0.0	289.02	970.65	1.1997	0.0058506	0.02
189.5	2.0	−0.0	289.05	967.56	1.197	0.0057687	0.02
220.4	2.0	−0.0	289.08	963.94	1.1937	0.0056736	0.02
256.7	2.0	−0.0	289.13	959.69	1.1898	0.0055636	0.02
299.35	2.0	−0.0	289.18	954.73	1.1853	0.0054367	0.02
349.5	2.0	0.0	289.23	948.91	1.18	0.0052906	0.02
408.45	2.0	0.0	289.3	942.1	1.1738	0.0051231	0.02
477.7	2.0	0.0	289.38	934.15	1.1665	0.0049321	0.02
559.05	2.0	0.0	289.48	924.88	1.158	0.0047153	0.02
654.65	2.0	0.0	289.59	914.06	1.148	0.004471	0.02
767.0	2.0	−0.0	289.73	901.47	1.1364	0.0041976	0.02
899.0	2.0	−0.0	289.88	886.85	1.1228	0.0038945	0.02
1054.1	2.0	−0.0	290.06	869.89	1.1063	0.0035623	0.019459
1236.35	2.0	−0.0	290.28	850.29	1.0859	0.0032028	0.017636
1450.5	2.0	−0.0	290.53	827.73	1.0622	0.00282	0.015495
1702.15	2.0	−0.0	290.81	801.85	1.035	0.0024203	0.012978
1997.85	2.0	−0.0	291.14	772.28	1.0037	0.0020132	0.010021
2345.3	2.0	−0.0	291.52	738.66	0.96894	0.0016107	0.007698
2753.55	2.0	−0.0	291.96	700.66	0.92932	0.0012275	0.0049763
3224.1	2.0	−0.0	292.45	658.78	0.88519	0.00088539	0.0018393
3724.1	2.0	−0.0	292.95	616.45	0.84128	0.00061512	0.0

4224.1	2.0	−0.0	293.46	576.19	0.80036	0.00041939	0.0
4724.1	2.0	−0.0	293.96	537.91	0.76074	0.0002802	0.0
5224.1	2.0	−0.0	294.47	501.54	0.72242	0.00018313	0.0

A.2 Derivation of cloud microphysics equations and their units

In Sec. (2.6) the cloud microphysics parameterisation of MITRAS is presented. Here, some derivations are shown.

A.2.1 Terminal Velocity of Rain

The terminal velocity of rain (Eq. 2.5) as used in MITRAS is derived in Doms (1985).

The rain water content q_1^{2r} is defined using the drop distribution function $N(m)$ with the drop mass m as

$$\rho q_1^{2r} = \int N(m) m dm \tag{A.1}$$

with the atmospheric density ρ. For rain water content, the limits of the integral are the separation drop mass m_t and infinity. The rain water flux I^{2r} can be expressed as

$$I^{2r} = \int_{m_t}^{\infty} N(m) \dot{m} dm \tag{A.2}$$

and the sedimentation flux of rain I_s^{2r} as

$$I_s^{2r} = \int_{m_t}^{\infty} N(m) m v_T(m) dm. \tag{A.3}$$

The drop mass dependent sedimentation speed is $v_T(m)$.

The sedimentation flux Eq.(A.3) is expressed depending on the rain rate RR (mmh^{-1}) in

$$I_s^{2r} = \rho_w RR. \tag{A.4}$$

For raindrops, a Marshall-Palmer size distribution

$$N_{MP}(D) = N_0 e^{-\lambda D} \tag{A.5}$$

with the empirical parameter $N_0 = 8 \cdot 10^6\,\mathrm{m}^{-4}$, a slope parameter λ in m^{-1}, and the rain droplet diameter D is assumed. The empirical relation for the slope parameter λ is

$$\lambda = 41 \cdot \frac{1}{\mathrm{m}} \left(\frac{\mathrm{h}}{\mathrm{mm}} \right)^{-0.21} \cdot 10^2 \cdot RR^{-0.21} \tag{A.6}$$

(Marshall and Palmer, 1948).

Applying the Marshall-Palmer size distribution (Eq. A.5) for the rain water content Eq. (A.1) results in an expression for the rain water content

$$\rho q_1^{2r} = \int_0^\infty N_{MP} \rho_w \frac{1}{6} \pi D^3 dD = \frac{\rho_w \pi N_0}{6} \int_0^\infty e^{-\lambda D} D^3 dD = \frac{\pi \rho_w N_0}{\lambda^4} \tag{A.7}$$

with the water density $\rho_w = 1000\,\mathrm{kgm}^{-3}$.

Inserting the rain rate dependent empirical relation for the slope parameter λ (Eq. A.6) into the expression for the rain water content Eq. (A.7) leads to a rain rate dependent expression of the rain water content, which has to be solved for the rain rate:

$$\begin{aligned} \rho q_1^{2r} &= \frac{\pi \rho_w N_0}{\left(41 \cdot \frac{1}{\mathrm{m}} \left(\frac{\mathrm{h}}{\mathrm{mm}} \right)^{-0.21} \cdot 10^2 \right)^4} \cdot RR^{0.84} \\ RR &= \left(\frac{\pi \rho_w N_0}{\left(41 \cdot \frac{1}{\mathrm{m}} \left(\frac{\mathrm{h}}{\mathrm{mm}} \right)^{-0.21} \cdot 10^2 \right)^4} \right)^{-\frac{1}{0.84}} \left(\rho q_1^{2r} \right)^{\frac{1}{0.84}} \end{aligned} \tag{A.8}$$

The terminal velocity of rain can be expressed as

$$v_{TR} = \frac{I_s^{2r}}{\rho q_1^{2r}} \tag{A.9}$$

where Eq. (A.4) is inserted for the sedimentation flux I_s^{2r} and Eq. (A.8) for the rain rate RR.

$$\begin{aligned} v_{TR} =& \rho_w RR \left(\rho q_1^{2r}\right)^{-1} = \\ & \rho_w \left(\frac{\pi \rho_w N_0}{\left(41 \cdot \frac{1}{\mathrm{m}} \left(\frac{\mathrm{h}}{\mathrm{mm}}\right)^{-0.21} \cdot 10^2\right)^4} \left(\frac{10^{-3}}{3600}\right)^{-0.84} \right)^{-\frac{1}{0.84}} \left(\rho q_1^{2r}\right)^{\frac{1}{0.84}} \left(\rho q_1^{2r}\right)^{-1} = \\ & \rho_w \left(\frac{\pi \rho_w N_0}{\left(41 \cdot \frac{1}{\mathrm{m}} \left(\frac{\mathrm{h}}{\mathrm{mm}}\right)^{-0.21} \cdot 10^2\right)^4} \right)^{-\frac{1}{0.84}} \left(\rho q_1^{2r}\right)^{0.1905}. \end{aligned} \tag{A.10}$$

Inserting the parameters leads to the terminal velocity of rain as used in MITRAS (Eq. 2.5):

$$\begin{aligned} v_{TR} =& 10^3 \frac{\mathrm{kg}}{\mathrm{m}^3} \left(\frac{\pi \cdot 10^3 \frac{\mathrm{kg}}{\mathrm{m}^3} \cdot 8 \cdot 10^6 \frac{1}{\mathrm{m}^4}}{\left(41 \cdot \frac{1}{\mathrm{m}} \left(\frac{\mathrm{h}}{\mathrm{mm}}\right)^{-0.21} \cdot 10^2\right)^4} \right)^{-\frac{1}{0.84}} \left(\rho q_1^{2r}\right)^{0.1905} \\ &= 10^3 \left(\frac{\pi \cdot 10^3 \cdot 8 \cdot 10^6}{(41 \cdot 10^2)^4}\right)^{-\frac{1}{0.84}} \frac{\mathrm{kg}}{\mathrm{m}^3} \left(\frac{\mathrm{kg}}{\mathrm{m}^3}\right)^{-\frac{1}{0.84}} \left(\left(\frac{\mathrm{mm}}{\mathrm{s}}\right)^{-0.84}\right)^{-\frac{1}{0.84}} \left(\rho q_1^{2r}\right)^{0.1905} \\ &= 10^3 \left(\frac{\pi \cdot 10^3 \cdot 8 \cdot 10^6}{(41 \cdot 10^2)^4}\right)^{-\frac{1}{0.84}} \frac{10^{-3}}{3600} \cdot \frac{\mathrm{m}}{\mathrm{s}} \left(\frac{\mathrm{kg}}{\mathrm{m}^3}\right)^{-0.1905} \left(\rho q_1^{2r}\right)^{0.1905} \\ &= \left(\frac{\pi \cdot 10^3 \cdot 8 \cdot 10^6}{(41 \cdot 10^2)^4}\right)^{-\frac{1}{0.84}} \frac{1}{3600} \cdot \frac{\mathrm{m}}{\mathrm{s}} \left(\frac{\mathrm{kg}}{\mathrm{m}^3}\right)^{-0.1905} \left(\rho q_1^{2r}\right)^{0.1905} \\ &= 18.46 \cdot \frac{\mathrm{m}}{\mathrm{s}} \left(\frac{\mathrm{kg}}{\mathrm{m}^3}\right)^{-0.1905} \left(\rho q_1^{2r}\right)^{0.1905} \\ &= 68.81 \cdot \frac{\mathrm{m}}{\mathrm{s}} \left(\frac{\mathrm{kg}}{\mathrm{m}^3}\right)^{-0.1905} \left(10^{-3} \cdot \rho q_1^{2r}\right)^{0.1905} \end{aligned} \tag{A.11}$$

A.2.2 Terminal Velocity of Snow

The terminal velocity of snow (Eq. 2.42) as used in MITRAS is derived in Doms et al. (2011). For snow, the Gunn-Marshall size distribution

$$N_{GM}(D) = N_0^s e^{-\lambda_s D} \tag{A.12}$$

(Gunn and Marshall, 1958) is assumed. The equivalent diameter D is the diameter a spherical water drop made of the melted snowflake with particle mass

$$m_s = \frac{\pi \rho_w}{6} D^3 \tag{A.13}$$

would have. Doms et al. (2011) calculated the slope parameter λ_s by solving the integral for snow water content (Eq. A.1):

$$\begin{aligned} \rho q_1^{3s} &= \frac{\rho_w \pi N_0^s}{6} \int_0^\infty e^{-\lambda_s D} D^3 dD = \frac{\rho_w \pi N_0^s}{\lambda_s^4} \\ \lambda_s &= \left(\frac{\pi \rho_w N_0^s}{\rho q_1^{3s}} \right)^{\frac{1}{4}} \end{aligned} \tag{A.14}$$

Inserting the Gunn-Marshall distribution (Eq. A.12), the particle mass (Eq. A.13), and the relation for the sedimentation speeds for individual snow particles

$$v_T^s = a_s D^{b_s} \tag{A.15}$$

with $a_s = 9.356\,\mathrm{m}^{0.7}\mathrm{s}^{-1}$ and $b_s = 0.3$ (Doms et al., 2011) in the equation for the sedimentation flux for snow (Eq. A.3) and solving the integral leads to

$$
\begin{aligned}
I_s^{3s} &= \int_0^\infty N_{GM}(D) v_T^s(D) m_s(D) dD = \frac{\rho_w \pi N_0^s a_s}{6} \int_0^\infty e^{-\lambda_s D} D^{b_s} D^3 dD \\
&= \frac{\rho_w \pi N_0^s a_s \Gamma(4+b_s)}{6\lambda_s^{4+b_s}}.
\end{aligned}
\tag{A.16}
$$

The terminal velocity for snow can be expressed like for rain using Eq. (A.3). For the sedimentation flux of snow I_s^{3s}, Eq. (A.16) is inserted and for the slope parameter λ_s, Eq. (A.14) is used leading to

$$
\begin{aligned}
v_{TS} &= \frac{I_s^{3s}}{\rho q_1^{3s}} = \frac{\rho_w \pi N_0^s a_s \Gamma(4+b_s)}{6} \lambda^{-(4+b_s)} \left(\rho q_1^{3s}\right)^{-1} \\
&= \frac{\rho_w \pi N_0^s a_s \Gamma(4+b_s)}{6} \left(\frac{\pi \rho_w N_0^s}{\rho q_1^{3s}}\right)^{-\frac{4+b_s}{4}} \left(\rho q_1^{3s}\right)^{-1} \\
&= \frac{a_s \Gamma(4+b_s)}{6} \left(\pi \rho_w N_0^s\right)^{-\frac{b_s}{4}} \left(\rho q_1^{3s}\right)^{\frac{b_s}{4}}.
\end{aligned}
\tag{A.17}
$$

Insertig the parameters leads to the terminal velocity for snow as used in MITRAS (Eq. 2.42):

$$
\begin{aligned}
v_{TS} &= \frac{9.356 \frac{m^{0.7}}{s} \cdot 8.86}{6} \left(\pi \cdot 10^3 \frac{\mathrm{kg}}{\mathrm{m}^3} 4 \cdot 10^5 \frac{1}{m^4}\right)^{-0.075} \left(\rho q_1^{3s}\right)^{0.075} \\
&= \frac{9.356 \cdot 8.86}{6} \left(\pi \cdot 10^3 \cdot 4 \cdot 10^5\right)^{-0.075} \frac{m^{-0.3} m}{s} \left(\frac{\mathrm{kg}}{m^7}\right)^{-0.075} \left(\rho q_1^{3s}\right)^{0.075} \\
&= 2.87 \cdot \left(\rho q_1^{3s}\right)^{0.075} \\
&= 4.82 \cdot \left(10^{-3} \cdot \rho q_1^{3s}\right)^{0.075}
\end{aligned}
\tag{A.18}
$$

(Doms et al., 2011).

A.2.3 Alternative Terminal Velocity for Rain

Deriving the terminal velocity of rain using the same approach as used for the snow terminal velocity leads to the equation for the terminal velocity of rain as used for the model COSMO (Doms et al., 2011). The sedimentation speed for individual rain drops is given as

$$v_T(D) = a\left(\frac{D}{D_0}\right)^b \tag{A.19}$$

with $a = 13\,\mathrm{ms}^{-1}$, $D_0 = 10^{-2}\,\mathrm{m}$, and $b = 0.5$ (Kessler, 1969; Doms, 1985; Doms et al., 2011). This leads to a sedimentation flux of

$$\begin{aligned} I_s^{2r} = &\int_0^\infty N_{MP}(D)v_T(D)m(D)dD = \frac{\rho_w \pi N_0 a}{6}\int_0^\infty e^{-\lambda D}D^b D^3 dD \\ =&\frac{\rho_w \pi N_0 a \Gamma(4+b)}{6\lambda^{4+b}} \end{aligned} \tag{A.20}$$

and a rain water content of

$$\begin{aligned} \rho q_1^{2r} = &\frac{\rho_w \pi N_0}{6}\int_0^\infty e^{-\lambda D}D^3 dD = \\ &\lambda = \left(\frac{\pi \rho_w N_0}{\rho q_1^{2r}}\right)^{\frac{1}{4}}. \end{aligned} \tag{A.21}$$

Inserting this in Eq. (A.9) yields

$$
\begin{aligned}
v_{TR,COSMO} &= \frac{13\frac{m}{s}\cdot 11.63}{6\cdot(10^{-2}m)^{0.5}}\left(\pi\cdot 10^3\frac{\mathrm{kg}}{\mathrm{m}^3}8\cdot 10^6\frac{1}{m^4}\right)^{-0.125}\left(\rho q_1^{2r}\right)^{0.125} \\
&= 12.63\left(\frac{\mathrm{kg}}{\mathrm{m}^3}\right)^{-0.125}\frac{m}{s}\left(\rho q_1^{2r}\right)^{0.125} \\
&= 12.63\cdot\left(\rho q_1^{2r}\right)^{0.125}.
\end{aligned}
\tag{A.22}
$$

A.2.4 Accretion

The parameterisation of accretion is based on the continuous model for drop growth. A rain drop with radius R, mass m and sedimentation speed $v_T(R)$ falls through an air volume in which cloud drops with radii r and sedimentation speeds $v_T(r)$ are distributed uniformly and continuously. This results in the mass growth rate of an individual rain drop of

$$
\dot{m}(R)|_{coa} = \pi\left(R+r\right)^2 E_c(R,r)\left(v_T(R)-v_T(r)\right)\left(\rho q_1^{2c}\right) \tag{A.23}
$$

with the geometrical collision cross section $\pi\left(R+r\right)^2$ and the collection efficiency $E_c(R,r)$ which together with the difference of sedimentation speeds makes the collection kernel for hydrodynamic gravitational capture.

Assuming $r \ll R$, $v_T(r) = 0$, and a constant mean collection efficiency $\overline{E}_c$ leads to the individual growth rates

$$
\dot{m}(D)|_{ac} = \frac{\pi}{4}D^2\overline{E}_c v_T(D)\left(\rho q_1^{2c}\right). \tag{A.24}
$$

Integrating the individual growth rates (Eq. A.24) over the entire rain drop spectrum (Eq. A.5) thereby using the sedimentation speed for individual rain drops (Eq. A.19) and the expression for λ in Eq. (A.21) results in an expression for the accretion rate:

$$\begin{aligned}\rho B_{acc} =& \int_0^\infty \dot{m}(D)|_{ac}\, N_{MP}(D) dD = \frac{\pi N_0 \overline{E}_c}{4} \left(\rho q_1^{2c}\right) \int_0^\infty e^{-\lambda D} D^2 v_T(D) dD \\ =& \frac{\pi N_0 \overline{E}_c a}{4 D_0^b} \left(\rho q_1^{2c}\right) \int_0^\infty e^{-\lambda D} D^{2+b} dD = \frac{\pi N_0 \overline{E}_c a}{4 D_0^b} \left(\rho q_1^{2c}\right) \lambda^{-b-3} \Gamma(3+b) \\ =& \frac{\pi N_0 \overline{E}_c a}{4 D_0^b} \left(\pi \rho_w N_0\right)^{-\frac{3+b}{4}} \Gamma(3+b) \left(\rho q_1^{2c}\right) \left(\rho q_1^{2r}\right)^{\frac{3+b}{4}}.\end{aligned} \tag{A.25}$$

Inserting the following parameters

$$\begin{aligned} N_0 =& 0.1 \cdot 10^8 \mathrm{m}^{-4} \\ \overline{E}_c =& 1 \end{aligned} \tag{A.26}$$

(Doms, 1985; Köhler, 1990) leads to the accretion equation used in MITRAS (Eq. 2.8):

$$\begin{aligned} B_{acc} =& \frac{\pi \cdot 0.1 \cdot 10^8 \mathrm{m}^{-4} \cdot 1 \cdot 13 \cdot \frac{\mathrm{m}}{\mathrm{s}}}{4 \cdot (10^{-2}\mathrm{m})^{0.5}} \left(\pi \cdot 10^3 \frac{\mathrm{kg}}{\mathrm{m}^3} 0.1 \cdot 10^8 \mathrm{m}^{-4}\right)^{-\frac{3+0.5}{4}} \Gamma(3.5) q_1^{2c} \left(\rho q_1^{2r}\right)^{\frac{3+0.5}{4}} \\ =& \frac{\pi \cdot 0.1 \cdot 10^8 \cdot 13}{4 \cdot (10^{-2})^{0.5}} \left(\pi \cdot 10^{10}\right)^{-0.875} 3.323351 \frac{1}{\mathrm{s}\mathrm{m}^{4\frac{7}{8}}} \left(\frac{\mathrm{kg}}{\mathrm{m}^3 \mathrm{m}^4}\right)^{-0.875} q_1^{2c} \left(\rho q_1^{2r}\right)^{0.875} \\ =& 2.216 \cdot \frac{1}{\mathrm{s}} \left(\frac{\mathrm{kg}}{\mathrm{m}^3}\right)^{-0.875} q_1^{2c} \left(\rho q_1^{2r}\right)^{0.875} \\ =& 934.63 \cdot \frac{1}{\mathrm{s}} \left(\frac{\mathrm{kg}}{\mathrm{m}^3}\right)^{-0.875} q_1^{2c} \left(10^{-3} \rho q_1^{2r}\right)^{0.875} \end{aligned} \tag{A.27}$$

Inserting different parameters ($N_0 = 8 \cdot 10^6\,\mathrm{m}^{-4}$ and $\overline{E} = 0.8$) leads to the accretion equation used in Doms et al. (2011).

A.2.5 Riming

For riming, the individual growth rates are given similarly to rain as

$$\dot{m}_s(D_s)|_{rim} = \frac{\pi}{4} D_s^2 \overline{E}_c^s v_T^s(D) \left(\rho q_1^{2c}\right) \tag{A.28}$$

with the constant mean collection efficiency by snow $\overline{E}_c^s = 0.875$ and the sedimentation speed $v_T^s(D)$. The snowflake mass is defined depending on the crystal diameter D_s as

$$m_s(D_s) = a_m(T)(D_s)^2 \tag{A.29}$$

with the temperature dependent mass-size relation of snow $a_m(T)$ (Eq. 2.46). The conversion equation for the different diameters is

$$D_s = D^{\frac{3}{2}} \sqrt{\frac{\pi \rho_w}{6 a_m(T)}} \tag{A.30}$$

using Eqs. (A.13) and (A.29).

The riming rate is calculated similarly to the accretion rate (Sec. A.2.4):

$$\rho B_{rim} = \int_0^\infty \dot{m}(D, D_s) N_{GM}(D) dD = \frac{\pi^2 N_0^s \overline{E}_c^s \rho_w a_s}{24 a_m(T)} \left(\rho q_1^{2c}\right) \int_0^\infty D^{3.3} e^{-\lambda_s D} dD \tag{A.31}$$

using the individual snow particle growth rate (Eq. A.28), the Gunn-Marshall distribution (Eq. A.12), the conversion factor for the different diameters (Eq. A.30), and the sedimentation speeds for snow particles (Eq. A.15). Solving the integral and inserting the parameter λ_s

$$\lambda_s = 25.5 \cdot 10^2 \frac{1}{m} \left(\frac{mm}{hr}\right)^{0.48} \cdot SR^{-0.48} \tag{A.32}$$

(Gunn and Marshall, 1958) leads to the riming rate

$$\rho B_{rim} = \frac{1}{a_m(T)} \frac{\pi}{24} \overline{E}_c^s a_s \Gamma(4.3) \left(\rho_w \pi N_0^s\right)^{-\frac{0.3}{4}} \left(\rho q_1^{2c}\right) \left(\rho q_1^{3s}\right)^{\frac{4.3}{4}} = \frac{1}{a_m(T)} \cdot 1.97 \cdot \left(\rho q_1^{2c}\right) \left(\rho q_1^{3s}\right)^{1.075} \tag{A.33}$$

for temperatures below the freezing temperature.

A.2.6 Condensation

The condensation parameter α_{cond} (Eq. 2.10) in the condensation equation (Eq. 2.9) is derived from the Tetens equation for the saturation vapour pressure of water over water

$$P_{\text{sat}} = P_R \cdot \exp\left(\frac{a\,(T - T_R)}{T - b}\right). \tag{A.34}$$

It is assumed that variations in pressure are neglectable compared to variations in temperature. Therefore the concentration of water vapour at saturation is only a function of height and potential temperature.

$$\begin{aligned} q_{sat} =& \frac{P_{sat}}{\rho_0 R_1 T_0} = \frac{P_R}{\rho_0 R_1 T_0} \cdot \exp\left(\frac{a\,(T - T_R)}{T - b}\right) \\ =& \frac{P_R}{\rho_0 R_1 \theta_0 \left(\frac{p}{p_0}\right)^{\frac{R}{c_p}}} \cdot \exp\left(\frac{a\left(\theta \left(\frac{p}{p_0}\right)^{\frac{R}{c_p}} - T_R\right)}{\theta \left(\frac{p}{p_0}\right)^{\frac{R}{c_p}} - b}\right) \end{aligned} \tag{A.35}$$

$$
\begin{aligned}
\alpha_{\text{cond}} =& 1 + \frac{l_{21}}{c_p \left(\frac{p_0}{p}\right)^{\frac{R}{cp}}} \left(\frac{\partial q_{sat}}{\partial \theta}\right) \\
=& 1 + \frac{l_{21}}{c_p \left(\frac{p_0}{p}\right)^{\frac{R}{cp}}} \cdot \frac{a \left(\frac{p}{p_0}\right)^{\frac{R}{cp}} \cdot \left(\theta \left(\frac{p}{p_0}\right)^{\frac{R}{cp}} - b\right) - \left(a \left(\theta \left(\frac{p}{p_0}\right)^{\frac{R}{cp}} - T_R\right)\right) \cdot \left(\frac{p}{p_0}\right)^{\frac{R}{cp}}}{\left(\theta \left(\frac{p}{p_0}\right)^{\frac{R}{cp}} - b\right)^2} \cdot q_{\text{sat}} \\
=& 1 + \frac{l_{21} \cdot q_{\text{sat}}}{c_p \left(\theta \left(\frac{p}{p_0}\right)^{\frac{R}{cp}} - b\right)^2} \cdot \left(a \cdot \theta \left(\frac{p}{p_0}\right)^{\frac{R}{cp}} - a \cdot b - a \cdot \theta \left(\frac{p}{p_0}\right)^{\frac{R}{cp}} + a \cdot T_R\right) \\
=& 1 + \frac{l_{21} \cdot q_{\text{sat}} \cdot a \left(T_r - b\right)}{c_p \left(\theta \left(\frac{p}{p_0}\right)^{\frac{R}{cp}} - b\right)^2}
\end{aligned}
\tag{A.36}
$$

It is unclear, where the constants for the equation were taken from. Doms (1985) and Köhler (1990) did not specify. In MITRAS, the potential temperature is given in K, while for the Teten's equation it is given in °C. Reverse engineering leads to the following equations:

$$
\begin{aligned}
T_R &= 0\,^\circ\text{C} = 273.15\,\text{K} \\
b &= 38.33\,\text{K} = -234.82\,^\circ\text{C} \\
a &= 17.15
\end{aligned}
\tag{A.37}
$$

Units:

$$
\alpha_{\text{cond}} = 1\,\text{s} + \frac{\text{J}\,\text{kg}\,\text{K} \cdot 4028\,\text{K}}{\text{kg}\,\text{J}\left(\text{K} - 38.33\,\text{K}\right)^2} = 1\,\text{s} + \frac{\text{K}^2}{\text{K}^2}
\tag{A.38}
$$

For it to make sense, a should have the unit seconds.

A.2.7 Evaporation of Rain Drops

The particle growth rate $\dot{m}(D)$ is based on the Howell equations with the Howell factor for water being

$$H_w = \frac{K l_{21}^2}{\nu_{air} R_v T^2} \rho_0 q_{sat} \tag{A.39}$$

with the molecular diffusion coefficient K, the latent heat of vapourisation l_{21}, and the thermal conductivity of dry air ν_{air} (Doms et al., 2011). The particle growth rate is given as

$$\dot{m}_{evap} = \frac{2\pi D K}{1 + H_w} F_v(D) \rho_0 \left(q_1^1 - q_{sat}\right). \tag{A.40}$$

Inserting the Howell factor (Eq. A.39) and saturation

$$S = \frac{q_1^1 - q\mathrm{sat}}{q_{\mathrm{sat}}} \cdot 100 \tag{A.41}$$

yields

$$\begin{aligned} \dot{m}_{evap} &= 2\pi D \frac{K \rho_0}{1 + \frac{K l_{21}^2 \rho_0 q_{sat}}{\nu_{\mathrm{air}} R_v T^2}} F_v(D) \left(q_1^1 - q_{sat}\right) \\ \dot{m}_{evap} &= 2\pi D \frac{K \rho_0 q_{sat} 10^{-2}}{1 + \frac{K l_{21}^2 \rho_0 q_{sat}}{\nu_{\mathrm{air}} R_v T^2}} F_v(D) S. \end{aligned} \tag{A.42}$$

The rain water flux is given with Eq. (A.2). The Marshall-Palmer size distribution (Eq. A.5) is assumed leading to

$$
\begin{aligned}
I^{2r} &= \int_0^\infty N_{MP}(D)\dot{m}_{evap}dD \\
&= \int_0^\infty N_0 e^{-\lambda D}\frac{2\pi DK\rho_0 q_{sat}}{1+\frac{KI_{21}^2\rho_0 q_{sat}}{\nu_{\text{air}}R_v T^2}}F_v(D)SdD \\
&= \frac{2\pi K\rho_0 q_{sat}SN_0}{1+\frac{KI_{21}^2\rho_0 q_{sat}}{\nu_{\text{air}}R_v T^2}}\int_0^\infty e^{-\lambda D}DF_v(D)dD
\end{aligned}
\tag{A.43}
$$

The ventilation factor is according to Doms (1985)

$$
F_v = c_1 + c_2\sqrt{N_{Re}}\left(\frac{\nu}{K}\right)^{1/3} \tag{A.44}
$$

with the constants c_1 and c_2, the kinematic viscosity of air ν, and the Reynolds number

$$
N_{Re} = \frac{Dv_T(D)}{\nu}. \tag{A.45}
$$

Using Eq. (A.19) for the sedimentation speed of rain drops v_T leads to the following expression for the ventilation factor

$$
F_v = c_1 + c_2\left(\frac{\nu}{K}\right)^{1/3}\sqrt{\frac{aD^{b+1}}{D_0^b\nu}}. \tag{A.46}
$$

Solving the integral of the evaporation rate (Eq. A.43) using Eq. (A.46) leads to

$$
\begin{aligned}
I^{2r} &= \frac{2\pi K\rho_0 q_{sat}SN_0}{1+\frac{KI_{21}^2\rho_0 q_{sat}}{\nu_{\text{air}}R_v T^2}}\int_0^\infty e^{-\lambda D}D\left(c_1 + c_2\left(\frac{\nu}{K}\right)^{1/3}\sqrt{\frac{aD^{b+1}}{D_0^b\nu}}\right)dD \\
&= \frac{2\pi K\rho_0 q_{sat}SN_0}{1+\frac{KI_{21}^2\rho_0 q_{sat}}{\nu_{\text{air}}R_v T^2}}\left(c_1\int_0^\infty e^{-\lambda D}DdD + c_2\left(\frac{\nu}{K}\right)^{1/3}\sqrt{\frac{a}{D_0^b\nu}}\int_0^\infty e^{-\lambda D}D\sqrt{D^{b+1}}dD\right) \\
&= \frac{2\pi K\rho_0 q_{sat}SN_0}{1+\frac{KI_{21}^2\rho_0 q_{sat}}{\nu_{\text{air}}R_v T^2}}\left(\frac{c_1}{\lambda^2} + c_2\left(\frac{\nu}{K}\right)^{1/3}\sqrt{\frac{a}{D_0^b\nu}}\lambda^{-\frac{b+5}{2}}\Gamma\left(\frac{b+5}{2}\right)\right).
\end{aligned}
\tag{A.47}
$$

With the expression for λ Eq. (A.21):

$$
\begin{aligned}
I^{2r} =& \sqrt{\frac{\rho q_1^{2r}}{\pi \rho_w N_0}} \frac{2\pi K \rho_0 q_{sat} S N_0}{1 + \frac{K l_{21}^2 \rho_0 q_{sat}}{\nu_{\text{air}} R_v T^2}} \left[c_1 + c_2 \left(\frac{\nu}{K}\right)^{1/3} \sqrt{\frac{a}{D_0^b \nu}} \left(\frac{\pi \rho_w N_0}{\rho_0 q_1^{2r}}\right)^{-\frac{b+1}{8}} \Gamma\left(\frac{b+5}{2}\right) \right] \\
=& \sqrt{\frac{4\pi^2 N_0^2}{\pi \rho_w N_0}} \frac{K \rho_0 q_{sat}}{1 + \frac{K l_{21}^2 \rho_0 q_{sat}}{\nu_{\text{air}} R_v T^2}} \sqrt{\rho_0 q_1^{2r}} \\
& \left[c_1 + c_2 \left(\frac{\nu}{K}\right)^{1/3} \sqrt{\frac{a}{D_0^b \nu}} \Gamma\left(\frac{b+5}{2}\right) (\pi \rho_w N_0)^{-\frac{b+1}{8}} \left(\rho_0 q_1^{2r}\right)^{\frac{b+1}{8}} \right] S \\
=& \sqrt{\frac{4\pi N_0}{\rho_w}} \frac{K \rho_0 q_{sat}}{1 + \frac{K l_{21}^2 \rho_0 q_{sat}}{\nu_{\text{air}} R_v T^2}} \sqrt{\rho_0 q_1^{2r}} \\
& \left[c_1 + c_2 \left(\frac{\nu}{K}\right)^{1/3} \sqrt{\frac{a}{D_0^b \nu}} \Gamma\left(\frac{5+b}{2}\right) (\pi \rho_w N_0)^{-\frac{1+b}{8}} \left(\rho_0 q_1^{2r}\right)^{\frac{1+b}{8}} \right] S
\end{aligned}
\tag{A.48}
$$

The term in the square brackets denotes the ventilation factor F_v. Inserting the parameters

$$
\begin{aligned}
c_1 &= 0.78 \\
c_2 \left(\frac{\nu}{K}\right)^{1/3} &= 0.277 \\
a &= 2115 \text{cms}^{-1} \\
b &= 0.8 \\
D_0 &= 1\text{cm} \\
\nu &= 0.14 \text{cm}^2\text{s}^{-1} \\
\rho_w &= 1 \text{gcm}^{-3} \\
N_0 &= 0.1 \text{cm}^{-4}
\end{aligned}
\tag{A.49}
$$

(Doms, 1985) yields

$$
\begin{aligned}
F_v =& 0.78 + 0.277 \cdot \sqrt{\frac{2115\,\mathrm{cm}}{\mathrm{s}} \frac{1}{\mathrm{cm}^{0.8}} \frac{\mathrm{s}}{0.14\mathrm{cm}^2}} \Gamma\left(\frac{5.8}{2}\right) \\
& \left(\pi \frac{\mathrm{g}}{\mathrm{cm}^3} 0.1 \frac{1}{\mathrm{cm}^4}\right)^{-1.8/8} \left(\rho_0 q_1^{2r}\right)^{1.8/8} \left(\frac{\mathrm{g}}{\mathrm{cm}^3}\right)^{1.8/8} \\
=& 0.78 + 0.277 \cdot \sqrt{\frac{2115}{0.14}} \cdot 1.827 \cdot (\pi \cdot 0.1)^{-0.225} \left(\frac{1}{\mathrm{cm}^{1.8}}\right)^{1/2} \left(\frac{1}{\mathrm{cm}^4}\right)^{-1.8/8} \\
& \left(\frac{\mathrm{g}}{\mathrm{cm}^3}\right)^{-0.225} \left(\rho_0 q_1^{2r}\right)^{0.225} \left(\frac{\mathrm{g}}{\mathrm{cm}^3}\right)^{0.225} \\
=& 0.78 + 80.73 \left(\frac{\mathrm{g}}{\mathrm{cm}^3}\right)^{-0.225} \left(\rho_0 q_1^{2r}\right)^{0.225} \left(\frac{\mathrm{g}}{\mathrm{cm}^3}\right)^{0.225} \\
=& 0.78 + 80.73 \left(\frac{\mathrm{kg}}{\mathrm{m}^3}\right)^{-0.225} \left(10^3\right)^{-0.225} \left(\rho_0 q_1^{2r}\right)^{0.225} \left(10^3\right)^{0.225} \left(\frac{\mathrm{kg}}{\mathrm{m}^3}\right)^{0.225}
\end{aligned}
\tag{A.50}
$$

which is Eq. (5.-125a) in Doms (1985), which was used in MITRAS (Eq. 2.13). Note that vor a and b other parameters were used than for the accretion.

The first two fractions in Eq. (A.48) represent the parameter for the droplet spectrum A_t, which is using parameters

$$
\begin{aligned}
K &= 7.399 \cdot 10^{-6}\, \frac{\mathrm{m}^2}{\mathrm{s}} \\
I_{21} &= 2.5 \cdot 10^6\, \frac{\mathrm{m}^2}{\mathrm{s}^2} \\
R_v &= 461\, \frac{\mathrm{m}^2}{\mathrm{K\,s}^2} \\
\nu_{\mathrm{air}} &= 0.026\, \frac{\mathrm{kg\,m}}{\mathrm{K\,s}^3}.
\end{aligned}
\tag{A.51}
$$

I reverse engineered the molecular diffusion coefficient.

$$
\begin{aligned}
A_t =& \sqrt{\frac{4\pi N_0}{\rho_w}} \frac{K \rho_0 q_{sat}}{1 + \frac{K I_{21}^2 \rho_0 q_{sat}}{\nu_{\text{air}} R_v T^2}} = \frac{A \cdot (\rho_0 \cdot q_{\text{sat}})}{1 + B \cdot (\rho_0 \cdot q_{\text{sat}}) T^{-2}} \\
A =& \sqrt{\frac{4\pi N_0}{\rho_w}} \cdot K \\
B =& \frac{K I_{21}^2}{\nu_{\text{air}} R_v}
\end{aligned}
\tag{A.52}
$$

$$
\begin{aligned}
A &= \sqrt{\frac{4 \cdot \pi \cdot 0.1 \cdot 10^8 \cdot \frac{1}{\text{m}^4}}{10^3 \cdot \frac{\text{kg}}{\text{m}^3}}} \cdot 7.399 \cdot 10^{-6} \cdot \frac{\text{m}^2}{\text{s}} \\
&= \sqrt{4 \cdot \pi \cdot 10^4} \cdot 7.399 \cdot 10^{-6} \cdot \left(\frac{\text{m}^3}{\text{kg}\,\text{m}^4} \right)^{0.5} \frac{\text{m}^2}{\text{s}} \\
&= 2.622 \cdot 10^{-3} \cdot \left(\frac{\text{m}^3}{\text{kg}} \right)^{0.5} \frac{1}{\text{s}}
\end{aligned}
\tag{A.53}
$$

$$
\begin{aligned}
B =& \frac{K I_{21}^2}{\nu_{\text{air}} R_v} \\
=& \frac{7.399 \cdot 10^{-6} \frac{\text{m}^2}{\text{s}} \left(2.5 \cdot 10^6 \frac{\text{m}^2}{\text{s}^2} \right)^2}{0.026 \cdot \frac{\text{kg}\,\text{m}}{\text{K}\,\text{s}^3} \cdot 461 \cdot \frac{\text{m}^2}{\text{K}\,\text{s}^2}} \\
=& \frac{7.399 \cdot 10^{-6} \cdot (2.5 \cdot 10^6)^2}{0.026 \cdot 461} \frac{\text{m}^6}{\text{s}^5} \frac{\text{K}\,\text{s}^3}{\text{kg}\,\text{m}} \frac{\text{K}\,\text{s}^2}{\text{m}^2} \\
=& 3.858 \cdot 10^6 \frac{\text{m}^3 \text{K}^2}{\text{kg}}
\end{aligned}
\tag{A.54}
$$

$$
\begin{aligned}
A_t =& \frac{2.622 \cdot 10^{-3} \cdot \left(\frac{\mathrm{m}^3}{\mathrm{kg}}\right)^{0.5} \frac{1}{\mathrm{s}} \cdot (\rho_0 \cdot q_{\mathrm{sat}})}{1 + 3.858 \cdot 10^6 \frac{\mathrm{m}^3\mathrm{K}^2}{\mathrm{kg}} \cdot (\rho_0 \cdot q_{\mathrm{sat}} T^{-2})} \\
=& \frac{2.622 \left(\frac{\mathrm{m}^3}{\mathrm{kg}}\right)^{0.5} \frac{1}{\mathrm{s}} \cdot (\rho_0 \cdot 10^{-3} \cdot q_{\mathrm{sat}})}{1 + 3.858 \cdot 10^9 \frac{\mathrm{m}^3\mathrm{K}^2}{\mathrm{kg}} \cdot (\rho_0 \cdot 10^{-3} \cdot q_{\mathrm{sat}})\, T^{-2}} \\
A_t =& \frac{2.623 \cdot 10^{-3} \cdot \left(\frac{\mathrm{m}^3}{\mathrm{kg}}\right)^{0.5} \frac{1}{\mathrm{s}} (\rho_0 \cdot 10^{-3} \cdot q_{sat})}{1 + 1.282 \cdot 10^{10} \cdot \frac{\mathrm{m}^3\mathrm{K}^2}{\mathrm{kg}} \cdot (\rho_0 \cdot 10^{-3} \cdot q_{sat})\, \theta^{-2}}
\end{aligned}
\tag{A.55}
$$

Units:

$$
\begin{aligned}
I^{2r} =& \frac{2.623 \cdot 10^{-3} \cdot \left(\frac{\mathrm{m}^3}{\mathrm{kg}}\right)^{0.5} \frac{1}{\mathrm{s}} (\rho_0 \cdot 10^{-3} \cdot q_{sat})}{1 + 1.282 \cdot 10^{10} \cdot \frac{\mathrm{m}^3\mathrm{K}^2}{\mathrm{kg}} \cdot (\rho_0 \cdot 10^{-3} \cdot q_{sat})\, \theta^{-2}} \cdot \sqrt{\rho_0 q_1^{2\mathrm{r}}} \cdot \\
& \left[0.78 + 80.73 \left(\frac{\mathrm{kg}}{\mathrm{m}^3}\right)^{-0.225} \left(\rho_0 10^3 q_1^{2r}\right)^{0.225}\right] S \\
B_{\mathrm{evap}} =& A_{\mathrm{t}} \cdot \sqrt{\rho_0 \cdot 10^{-3} \cdot q_1^{2\mathrm{r}}} \cdot F_{\mathrm{v}} \cdot \frac{S}{\rho_0 \cdot 10^{-3}} \\
\frac{1}{\mathrm{s}} =& \left(\frac{\mathrm{m}^3}{\mathrm{kg}}\right)^{0.5} \frac{1}{\mathrm{s}} \cdot \frac{\mathrm{kg}}{\mathrm{m}^3} \cdot \frac{1}{1 + \frac{\mathrm{m}^3\mathrm{K}^2}{\mathrm{kg}} \frac{\mathrm{kg}}{\mathrm{m}^3\mathrm{K}^2}} \cdot \left(\frac{\mathrm{kg}}{\mathrm{m}^3}\right)^{0.5} \cdot \left[0.78 + \left(\frac{\mathrm{kg}}{\mathrm{m}^3}\right)^{-0.225} \cdot \left(\frac{\mathrm{kg}}{\mathrm{m}^3}\right)^{0.225}\right] \cdot \frac{\mathrm{m}^3}{\mathrm{kg}} \\
\frac{1}{\mathrm{s}} =& \frac{1}{\mathrm{s}}
\end{aligned}
\tag{A.56}
$$

A.3 Hit rates with WMO thresholds

Table A.5: Thresholds for the absolute (W) and relative deviation (D) for hit rate calculation (q) for wind speed components u, v, w, temperature T, net long and short wave radiation LW_{net} and SW_{net}, and precipitation amount P on ground.

	u	v	w	T	LW_{net}	SW_{net}	P
W	$0.5\,\text{ms}^{-1}$	$0.5\,\text{ms}^{-1}$	$0.5\,\text{ms}^{-1}$	0.2 K	$5\,\text{Wm}^{-2}$	$5\,\text{Wm}^{-2}$	0.1 mm
D [%]	10	10	10	0.04	5	2	2

Table A.6: Hit rates q in percent of wind components (u, v, w), temperature (T), net surface long wave and short wave radiation (LW_{net} SW_{net}), and precipitation amount (P) on ground after 1 hour simulation time using thresholds based on WMO (2023a).

Cases	u	v	w	T	LW_{net}	SW_{net}	P
Wwr - Wwr_np	100	100	100	100	100	100	100
Wwr_noprecip - Winit	100	100	100	99	100	100	-
Wwr - Wwr_noprecip	84	44	99	0	0	0	0
Cice - Cwr	96	94	97	53	38	0	100
Hice - Hwr	49	55	100	12	12	0	100
Wice - Wwr	92	79	96	36	47	8	100

A.4 Radiation plots

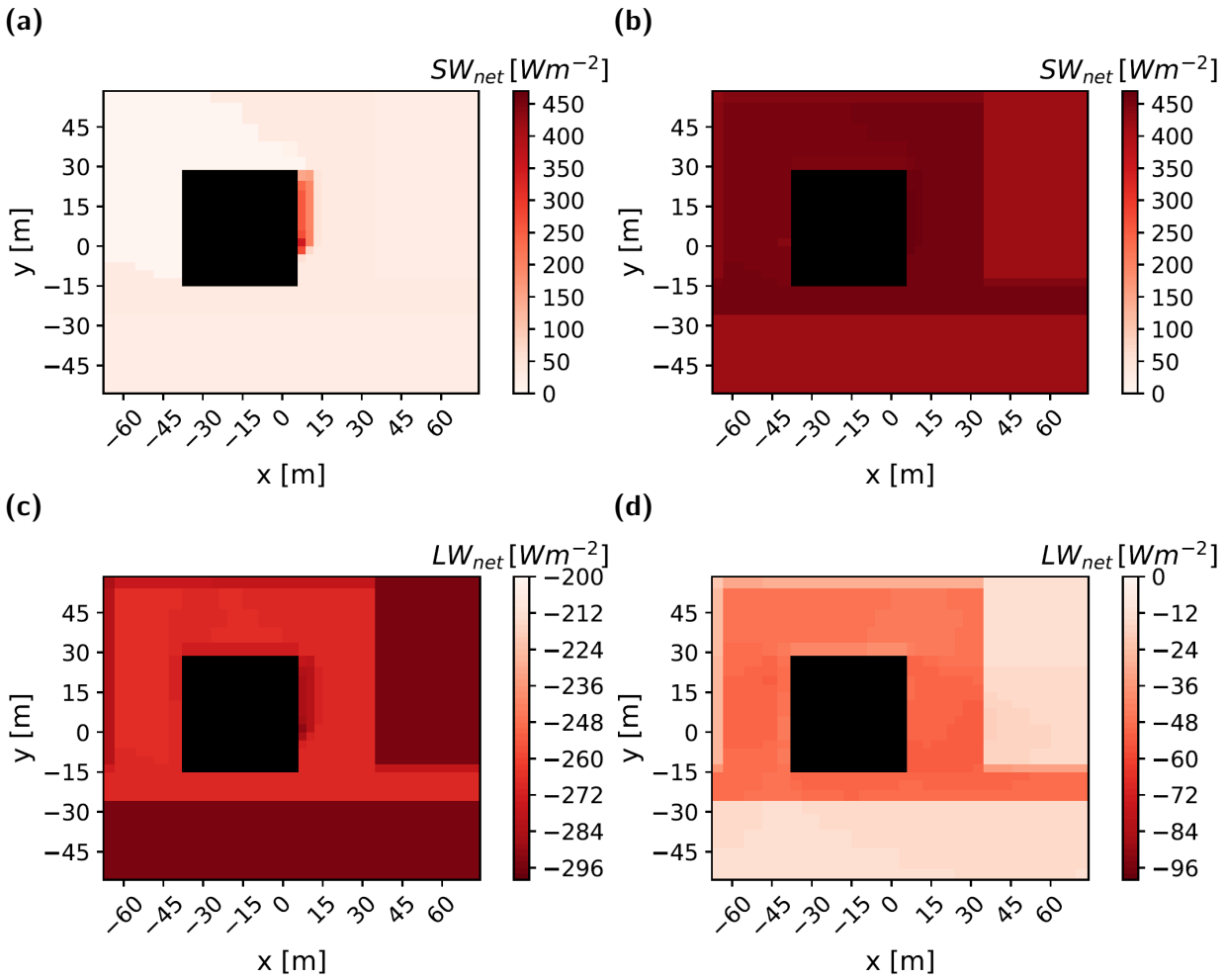

Figure A.1: Net surface short wave radiation SW_{net} (a,b) and long wave radiation $LW_$net (c,d) of Wwr_noprecip (a,c) and Wwr (b,d) after one hour of simulation time.

B Supporting information to Chapter 3

B.1 Statements on submitted manuscript

B.1.1 Acknowledgements

This work was financed within the framework of the Helmholtz Institute for Climate Service Science (HICSS), a cooperation between Climate Service Center Germany (GERICS) and Universität Hamburg, Germany, and conducted as part of the WINTER project (Investigating climate change related impacts on the urban winter climate of Hamburg).

The radar data forcing development and corresponding model evaluation were funded by the Deutsche Forschungsgemeinschaft (DFG, German Research Foundation) under Germany's Excellence Strategy - EXC 2037 'CLICCS - Climate, Climatic Change, and Society' - Project Number: 390683824. The work contributes to the Center for Earth System Research and Sustainability (CEN) of Universität Hamburg.

Thanks go to Dr. Peter Hoffmann (GERICS) and Dr. Kevin Sieck (GERICS) for constructive comments on an earlier version of this paper and to Dr. David Grawe (Universität Hamburg) for his support in the model development and the analysis of the results.

B.2 Plots of normalised rain amounts

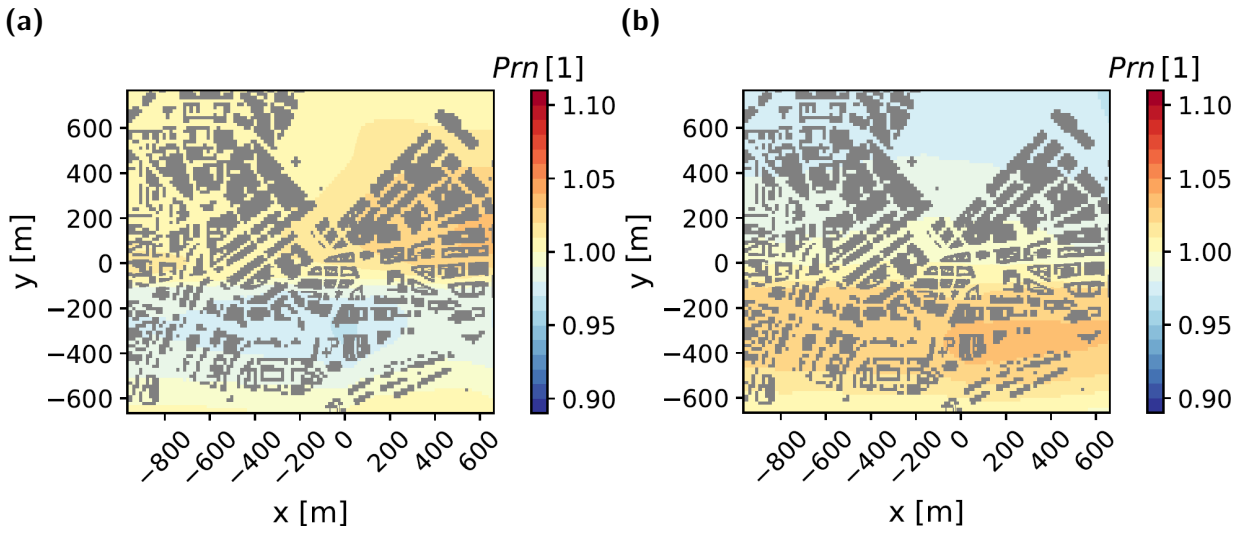

Figure B.1: Horizontal cross section of the normalised rain amount Prn with weighted mean on ground in phase III for (a) RH_LL27 and (b) RH_LM27. [1] denotes non-dimensional values.

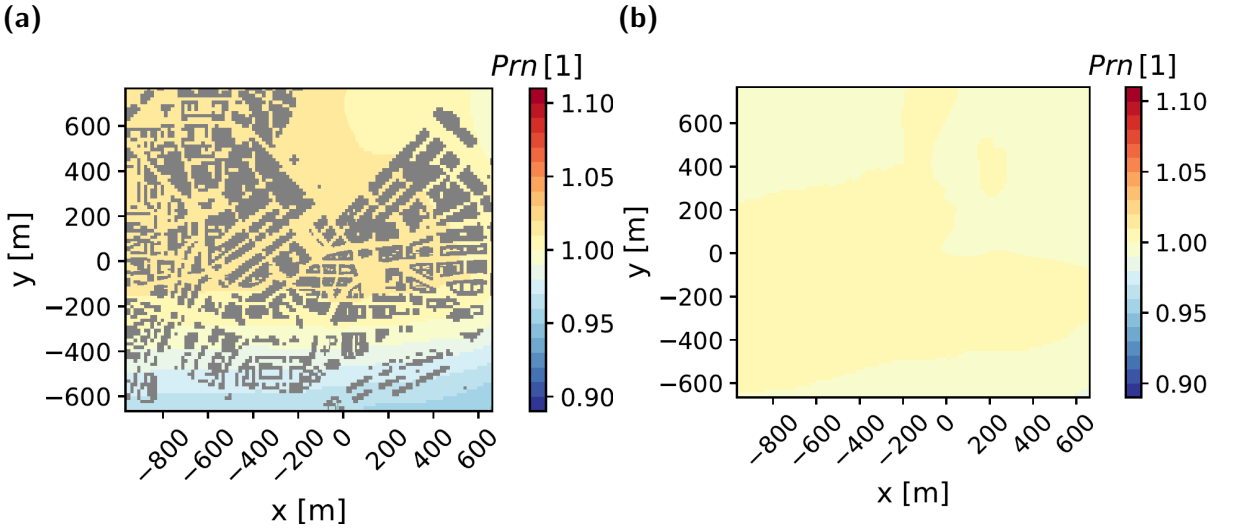

Figure B.2: Horizontal cross section of the normalised rain amount Prn with weighted mean on ground in phase III for (a) RH_MM27norog and (b) RH_MM27nobuild. [1] denotes non-dimensional values.

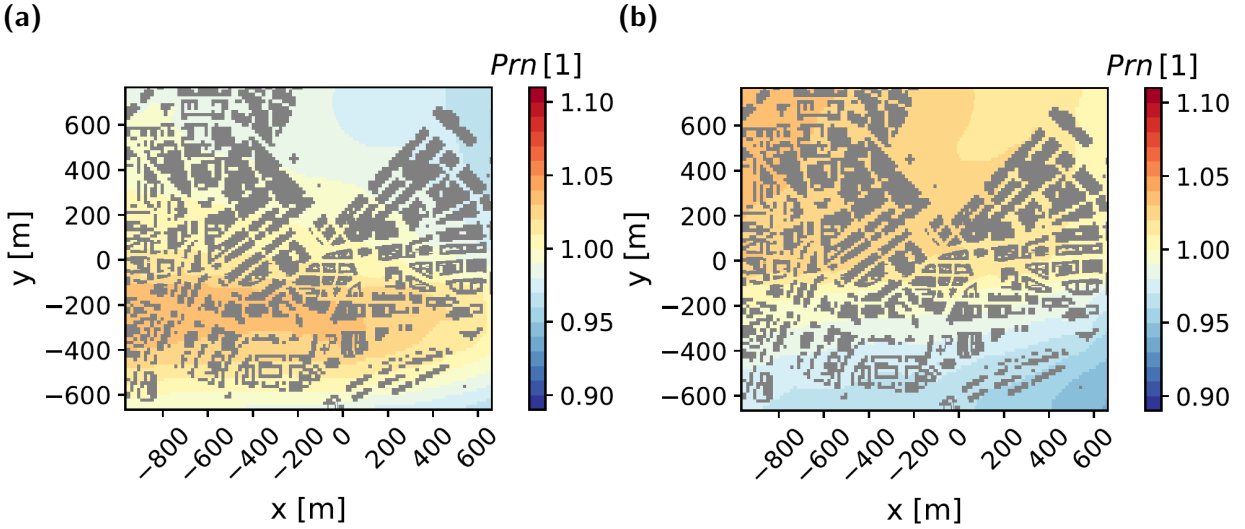

Figure B.3: Horizontal cross section of the normalised rain amount Prn with weighted mean on ground in phase III for (a) RH_HM27 and (b) RH_HH27. [1] denotes non-dimensional values.

C Supporting information to Chapter 4

C.1 Statements on submitted manuscript

C.1.1 Acknowledgements

This work was financed within the framework of the Helmholtz Institute for Climate Service Science (HICSS), a cooperation between Climate Service Center Germany (GERICS) and University Hamburg, Germany, and conducted as part of the WINTER project (Investigating climate change related impacts on the urban winter climate of Hamburg).

This work was partly funded by the Deutsche Forschungsgemeinschaft (DFG, German Research Foundation) under Germany's Excellence Strategy – EXC 2037 'CLICCS – Climate, Climatic Change, and Society' – Project Number: 390683824. The work contributes to the Center for Earth System Research and Sustainability (CEN) of University of Hamburg.

C.1.2 Code availability

Currently the MITRAS source code is distributed upon request under the terms of a user agreement with the Mesoscale and Microscale Modeling (MeMi) working group at the Meteorological Institute, University of Hamburg (https//www.mi.uni-hamburg.de/memi). A copy of the user agreement is available upon request. Due to current copyright restrictions, users are requested to contact the corresponding authors to obtain access to the code free of charge for research purposes under a collaboration agreement (metras@uni-hamburg.de).

C.2 Precipitation heterogeneities of simulations with 230° initial wind direction

For the sensitivity studies in Chapter 4, two simulations were performed with an initial wind direction at 10 m height of 230 °: SP_LL23 and SP_LS23. The initial conditions – except for the wind direction – were the same as in SP_LL27 and SP_LS27 (Tab. 4.1). The precipitation heterogeneity of the precipitation amount on ground accumulated between 8:30:00 and 8:35:00 LST given as in Tab. 4.2 for SP_LL23 is 6.5 % and for SP_LS23 it is 10.4 %. The mean snow amount is 0.2 mm in both cases. For the precipitation accumulated between 8:35:00 and 9:00:00 LST, the values for SP_LL23 are 9.5 % with 1.4 mm and for SP_LS23 3.9 % with 1.6 mm. The mean rain amounts are zero in both cases and time spans.

C.3 Normalised precipitation amounts on ground

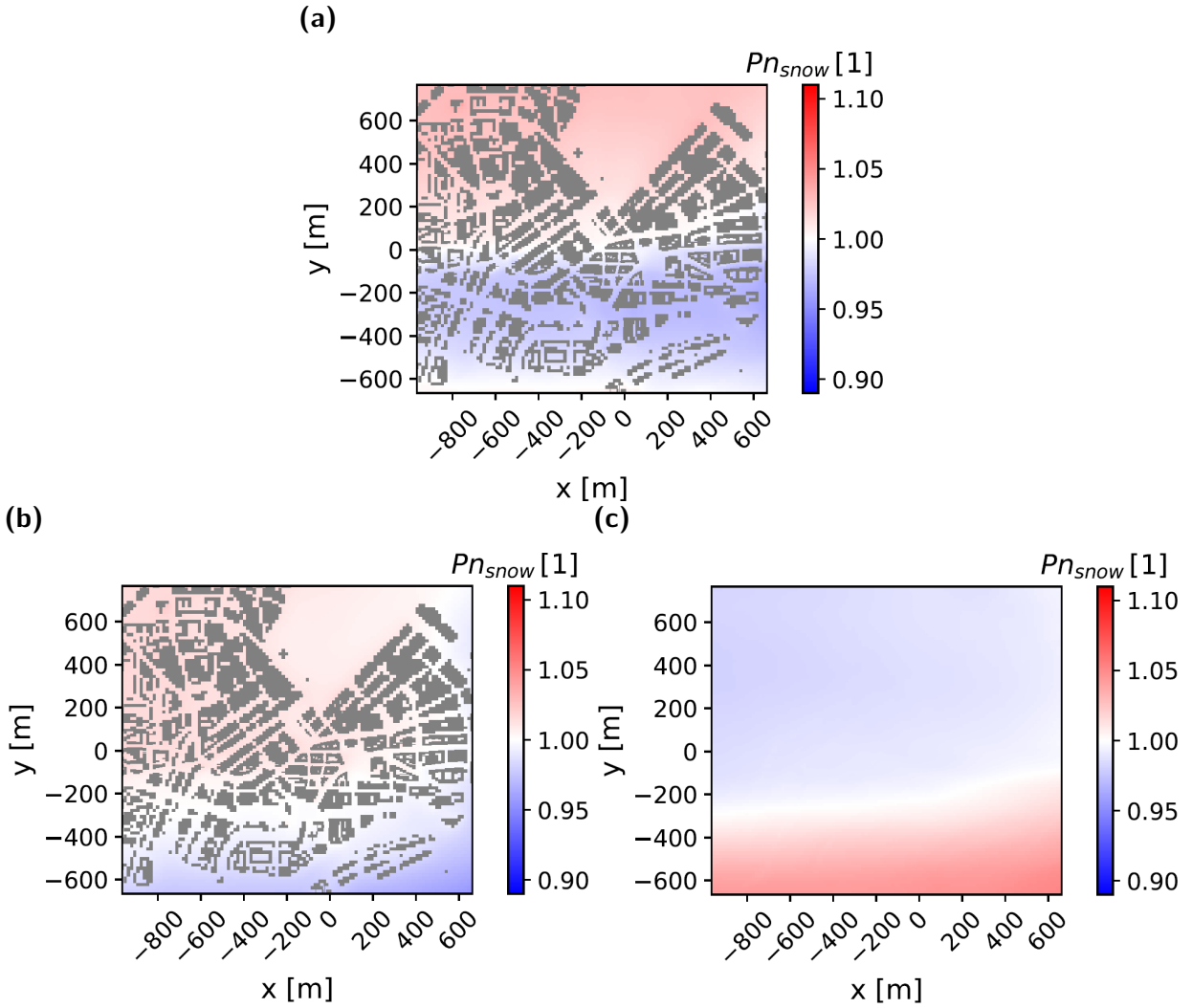

Figure C.1: Horizontal cross sections of the normalised snow amount on ground accumulated between 8:35:00 and 9:00:00 LST for (a) SP_LS27, (b) SP_LS27_norog, and (c) SP_LS27_nobuild. Pn_{snow} is calculated as deviation from the area weighted mean of the snow amount.

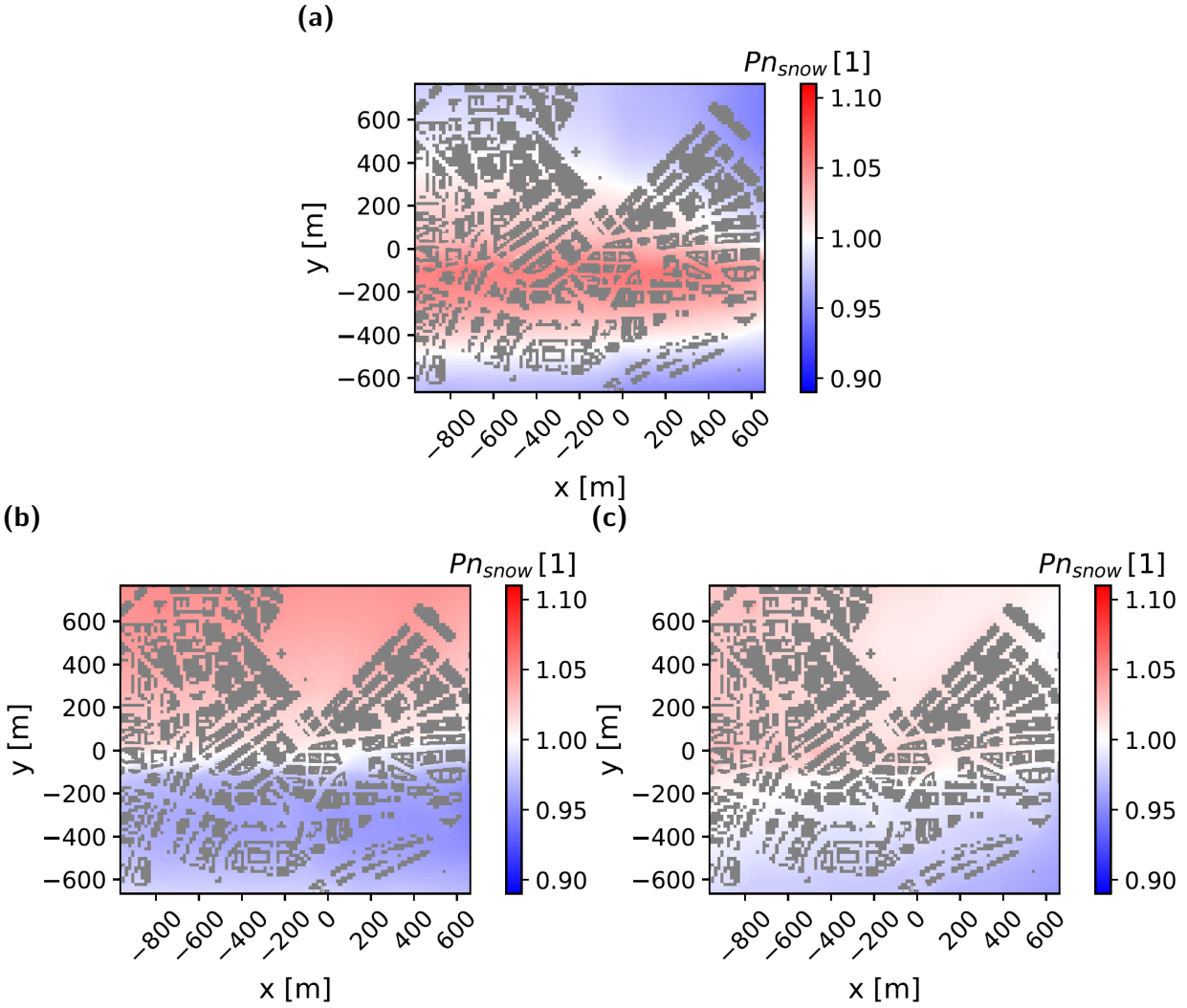

Figure C.2: Horizontal cross sections of the normalised snow amount on ground accumulated between 8:35:00 and 9:00:00 LST for (a) SP_ML27, (b) SP_MS27, and (c) SP_LM27. Pn_{snow} is calculated as deviation from the area weighted mean of the snow amount.

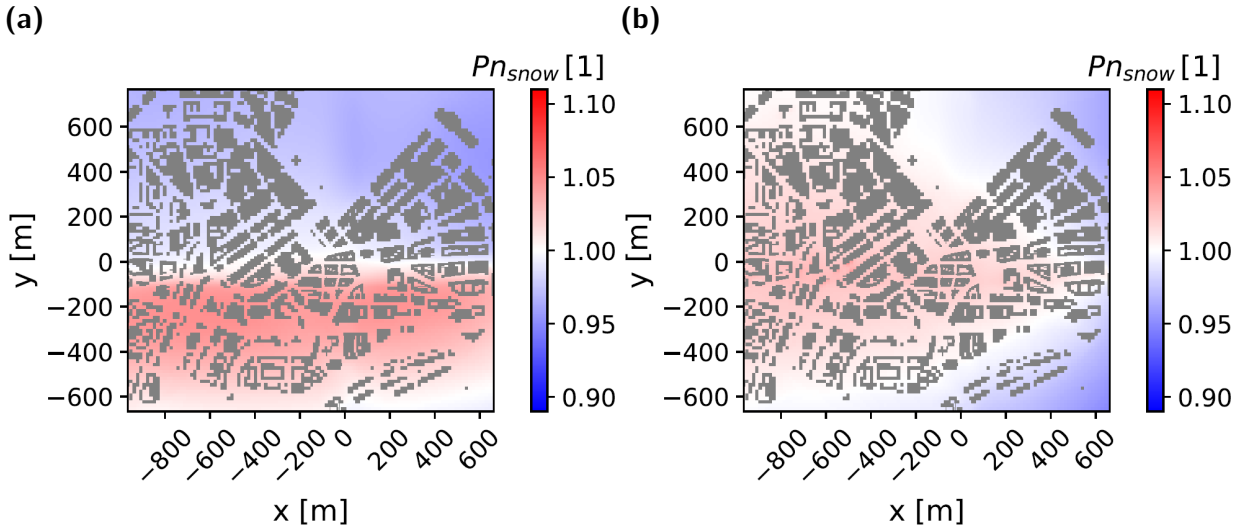

Figure C.3: Horizontal cross sections of the normalised snow amount on ground accumulated between 8:35:00 and 9:00:00 LST for (a) SP_LL27_light and (b) SP_LL27_heavy. Pn_{snow} is calculated as deviation from the area weighted mean of the snow amount.

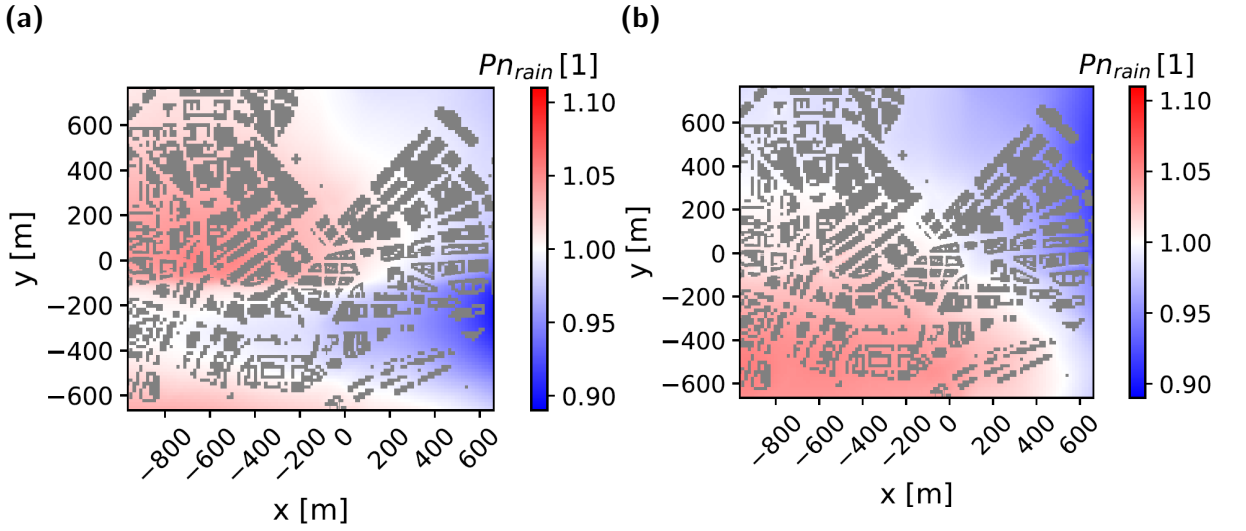

Figure C.4: Horizontal cross sections of the normalised rain amount on ground accumulated between 8:35:00 and 9:00:00 LST for (a) SP_HL27 and (b) SP_HS27. Pn_{rain} is calculated as deviation from the area weighted mean of the rain amount.

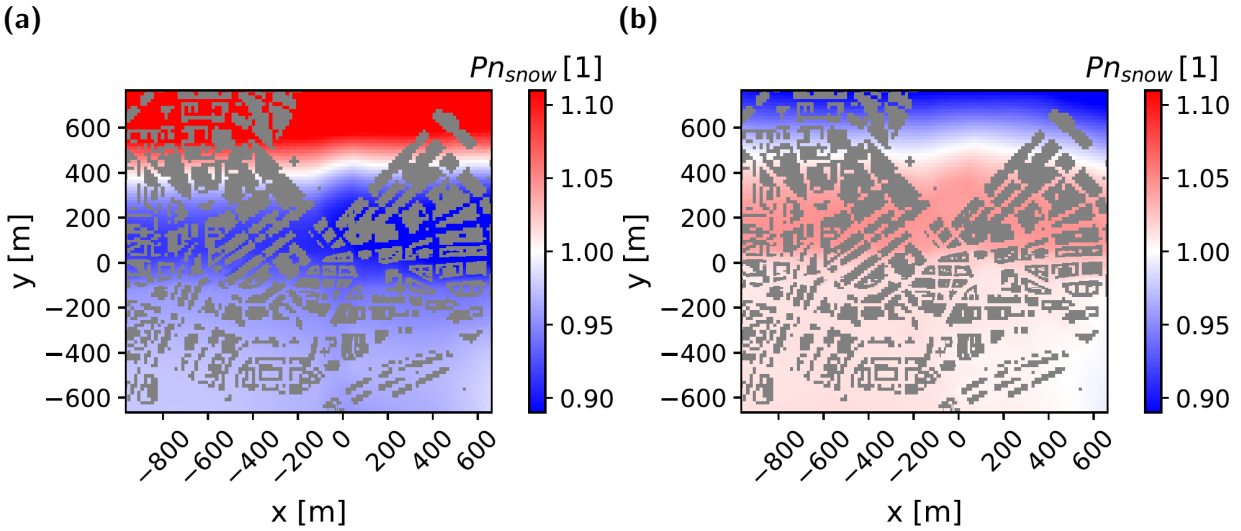

Figure C.5: Horizontal cross sections of the normalised snow amount on ground accumulated between 8:35:00 and 9:00:00 LST for (a) SP_LL23 and (b) SP_LS23. Pn_{snow} is calculated as deviation from the area weighted mean of the snow amount.

C.4 Normalised temperatures on ground

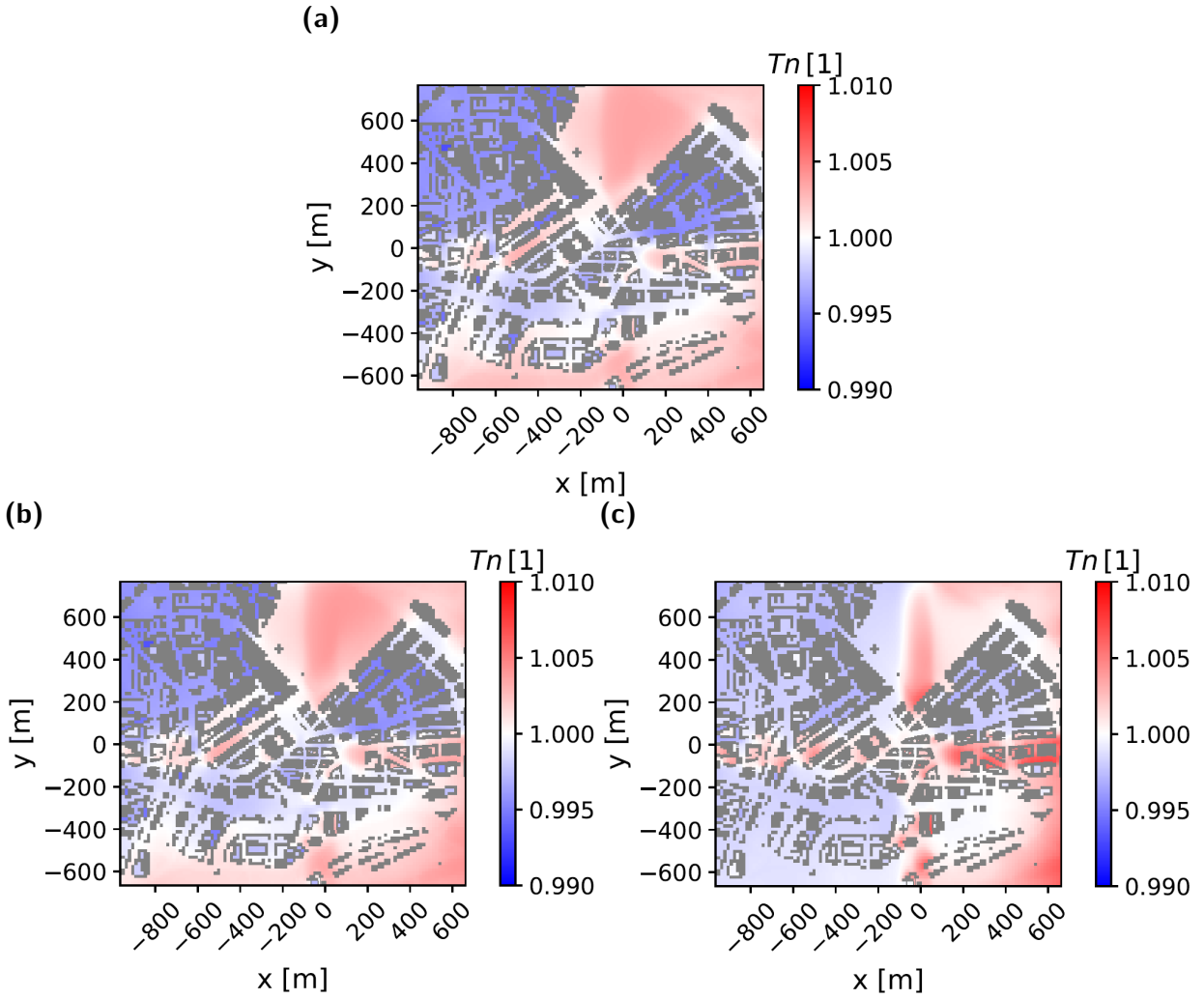

Figure C.6: Horizontal cross sections of the normalised air temperature at 8:45:00 LST for (a) SP_LS27, (b) SP_MS27, and (c) SP_HS27. Tn is calculated as deviation from the area weighted mean of the temperature above ground.

C.5 Surface influences on snow patterns for SP_ML27

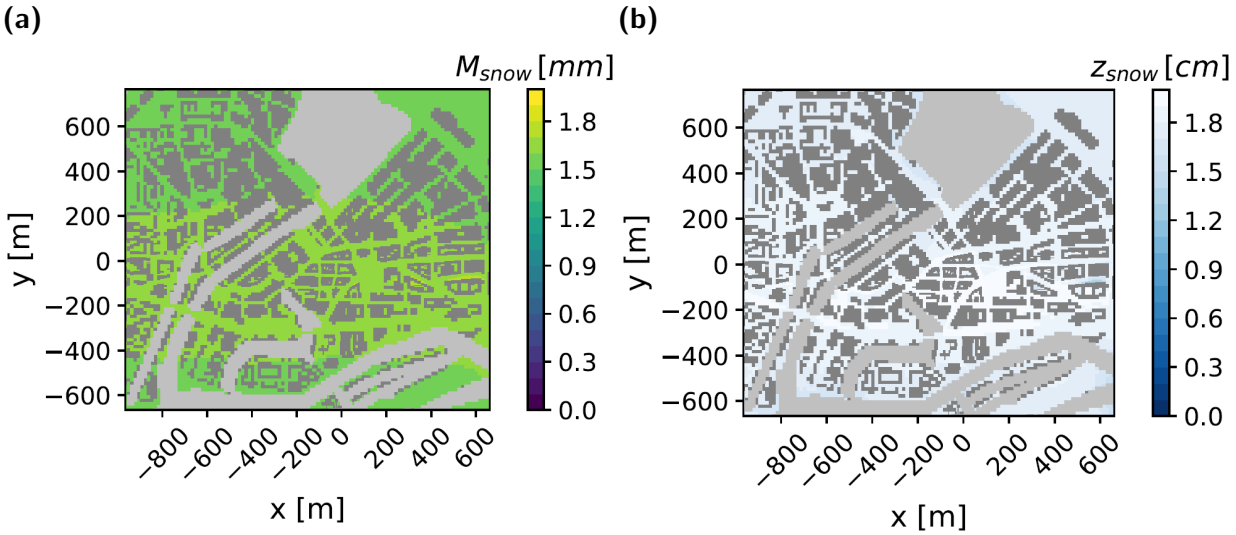

Figure C.7: Horizontal cross sections of (a) the amount of melted snow water equivalent $M_$snow and (b) the snow height z_{snow} at 9:00:00 LST for SP_ML27. Light grey denotes water surfaces and dark grey denotes buildings.

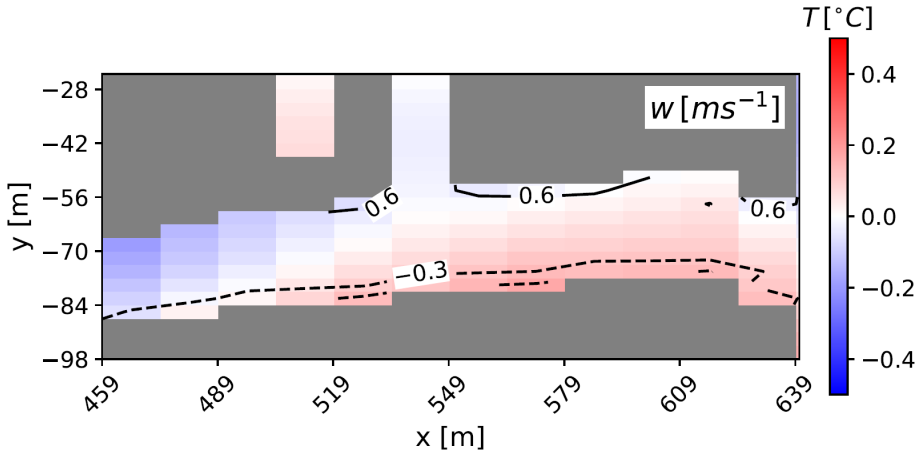

Figure C.8: Horizontal cross section of the temperature T (colours) and vertical velocity w (upwinds solid lines, downwinds dashed lines) at Altstädterstraße for SP_ML27 at 14 m height at 8:40:00.

List of Acronyms

ATKIS	amtliches topographisch-kartographisches Informationssystem (official topographic-cartographic information system)
DKRZ	Deutsches Klimarechenzentrum (German Climate Computing Center)
DWD	Deutscher Wetterdienst (German meteorological service)
GRQ	guiding research question
J14	Järvi et al. (2014)
LoD	level of detail
LST	Local Solar Time
METRAS	mesoscale transport and stream model
MITRAS	microscale transport and stream model
M-SYS	multiscale model system
PALM	independent name of model system
RAMS	regional atmospheric modelling system
RQ	research question
RR	rain rate
rwc	rain water content
SWE	snow water equivalent
UTC	Universal Time Coordinated
V91	Verseghy (1991)
VDI	Verein Deutscher Ingenieure (association of German engineers)
WDCC	World Data Center for Climate
WMO	World Meteorological Organization

List of Symbols

Latin Letters

A_t	parameter for the rain droplet spectrum
a_mc	parameter for $a_\mathrm{m}(T)$ ($0.08\,\mathrm{kgm}^{-2}$)
a_mv	parameter for $a_\mathrm{m}(T)$ ($0.02\,\mathrm{kgm}^{-2}$)
$a_\mathrm{m}(T)$	mass-size relation of snow
$B^\mathrm{c}_\mathrm{acc}$	accretion rate (ice scheme)
$B^\mathrm{w}_\mathrm{acc}$	accretion rate (warm rain scheme)
B^c_au	autoconversion rate (ice scheme)
B^w_au	autoconversion rate (warm rain scheme)
B_cfrz	contact nucleation rate
B_cond	condensation rate
B_dep	deposition rate
B_evap	evaporation rate
bh	roof height
B_ifrz	immersion freezing rate
B_melt	melting rate
B_nuc	nucleation rate
B_rim	riming rate
B_she	shedding rate
B^*	heat conduction parameter
c_p	specific heat of dry air at constant pressure
c_ice	specific heat capacity of ice
$c_\mathrm{v,snow}$	volumetric heat capacity of snow
D	threshold value for relative deviation
dd_init	initial wind direction
D_VDI	threshold value for relative deviation for wind speed following VDI (2017) (0.05)
E	rate of evaporation on ground
E_cf	collection efficiency ($5.0 \cdot 10^{-3}$)
F	correction factor
ff	wind speed
ff_init	initial wind speed
ffn	normalised wind speed
F_v	ventilation factor
$\overline{F}_{\overline{\phi}}$	diffusion term
$\overline{F}_{\overline{\phi},\dot{x}^1}$	diffusion term in x-direction

G_{soil}	heat flux to soil
h	orography height
H_{S}	sensible heat flux
hr	roof height
h_{snow}	depth of daily temperature wave in snow
h_{soil}	depth of daily temperature wave in soil
i	location index
l_{21}	latent heat of vaporisation
l_{31}	latent heat of sublimation
l_{32}	latent heat of fusion
k	location index
K_{hor}	horizontal exchange coefficient
K_{ver}	vertical exchange coefficient
$k^{\text{s}}_{\text{cold}}$	inverse autoconversion interval for snow ($10^{-3}\,\text{s}^{-1}$)
$k^{\text{r}}_{\text{cold}}$	inverse autoconversion interval for rain in ice scheme ($10^{-4}\,\text{s}^{-1}$)
k_{snow}	thermal diffusivity in snow
k_{soil}	thermal diffusivity in soil
$k^{\text{r}}_{\text{warm}}$	inverse autoconversion interval for rain in warm rain scheme ($10^{-3}\,\text{s}^{-1}$)
LW_{net}	net surface long wave radiation
L_{S}	latent heat flux
M	melting rate of SWE on ground
M_{snow}	Amount of melted snow on ground
N	total number of compared values
$N_{\text{cf},0} = 2.0 \cdot 10^5$	concentration of natural contact ice nuclei active at -4°C at sea level
n	hit/ fail
n_t	time step
O	observation/ older model version
P	precipitation amount on ground
p_0	basic state atmospheric pressure
Pd	prediction/ newer model version
Pn_{snow}	normalised snow amount
P_{rain}	rain amount on ground
P_{rate}	precipitation rate
p_{ref}	reference pressure (100 000 Pa)
Prn	normalised rain amount
Pr_{snow}	rate of snowfall
p_{S}	atmospheric pressure on ground surface
P_{snow}	snow amount on ground
$p_{\text{snow}_{z_0}}$	snow cover fraction

q	hit rate
q_1^1	specific humidity
$q_{1,\mathrm{sat}}^1$	saturation specific humidity over water
$q_{1,\mathrm{sat,ice}}^1$	saturation specific humidity over ice
q_1^{2c}	cloud water content
$q_{1,\mathrm{cri}}^{2c}$	critical value for autoconversion ($10^{-3}\,\mathrm{kgkg}^{-1}$)
q_1^{2r}	rain water content
q_1^{3s}	snow water content
R	gas constant for dry air
S	saturation
SWE	snow water equivalent
SWE_{crit}	critical SWE (0.05 m)
SW_{net}	net surface short wave radiation
T	temperature
T_0	freezing point (273.16 K)
T_1	minimum temperature for mass-size relation of snow (253.16 K)
T_2	minimum temperature for temperature function (235.16 K)
$T_{\mathrm{h,soil}}$	deep soil temperature
T_{init}	initial temperature
T_{S}	temperature on ground surface
t	time
u	wind in west-east direction
U_{ref}	reference wind speed
v	wind in south-north direction
v_{T}	sedimentation velocity
v_{TR}	terminal velocity of rain
v_{TS}	terminal velocity of snow
W	threshold value for absolute deviation
W_{VDI}	threshold value for absolute deviation for wind speed following VDI (2017) ($0.01\,\mathrm{ms}^{-1}$)
w	wind in vertical direction
x	horizontal coordinate in west-east direction in Cartesian coordinate system
$\dot{x}^1$	coordinate in terrain-following coordinate system
$\dot{x}^2$	coordinate in terrain-following coordinate system
$\dot{x}^3$	coordinate in terrain-following coordinate system
y	horizontal coordinate in south-north direction in Cartesian coordinate system
z	vertical coordinate in Cartesian coordinate system
z_0	roughness length

$z_{0_{\mathrm{ini}}}$	initial z_0 without snow cover
$z_{0_{\mathrm{snow}}}$	snow roughness length (10^{-3} m)
z_{snow}	snow depth

Greek Letters

α	albedo
α_{cf}	contact nucleation factor ($1.55 \cdot 10^{-3}$)
α_{cond}	condensation parameter
α_{dep}	deposition factor
α_{if}	immersion freezing factor ($9.95 \cdot 10^{-5}$)
α_{ini}	initial α without snow cover
α_{max}	maximum α_{snow} (0.85)
α_{melt}	melting factor ($7.2 \cdot 10^{-6}$)
α_{min}	minimum α_{snow} (0.18)
$\alpha_{\mathrm{min,J14}}$	minimum α_{snow} following Järvi et al. (2014) (0.18)
$\alpha_{\mathrm{min,V91}}$	minimum α_{snow} following Verseghy (1991)(0.5)
α^*	grid volume
β	empirical factor for roughness length (0.408)
β_{dep}	deposition factor (13.0)
β_{melt}	melting factor (13.0)
ΔSWE	difference of SWE
ΔSW_{net}	difference of SW_{net}
Δt	time step
Δv	difference of v wind component
ϵ	very small number (10^{-6})
$\epsilon(T)$	temperature function
ν_{ice}	thermal conductivity of ice
ν_{snow}	thermal conductivity of snow
ν_{soil}	thermal conductivity of soil
θ	potential temperature
ρ_0	basic state atmospheric density
$\overline{\rho_A^1}$	mean area density of the vertically integrated water vapour (kg m^{-2})
$\overline{\rho_A^{2c}}$	mean area density of the vertically integrated cloud water content (kg m^{-2})
$\overline{\rho_A^{2r}}$	mean area density of the vertically integrated rain water content (kg m^{-2})
$\overline{\rho_A^{3s}}$	mean area density of the vertically integrated snow water content (kg m^{-2})
ρ_{ice}	density of ice (918.9 kgm$^-$3)
ρ_{max}	maximum ρ_{snow} (300 kgm$^-$3)
ρ_{min}	minimum ρ_{snow} (100 kgm$^-$3)
ρ_{ref}	reference density (1.29 kgm^{-3})
ρ_{snow}	snow pack density

ρ_{w}	density of water
σ_n	precipitation heterogeneity
τ	period of temperature wave (86400 s)
τ_1	time period parameter (86400 s)
τ_{f}	empirical parameter for ρ_{snow} (0.24)
$\tau_{\mathrm{f},\alpha}$	empirical parameter for albedo (0.11)
$\tau_{\mathrm{f},\alpha,\mathrm{J14}}$	empirical parameter for albedo following Järvi et al. (2014) (0.11)
$\tau_{\mathrm{f},\alpha,\mathrm{V91}}$	empirical parameter for albedo following Verseghy (1991) (0.24)
τ_α	empirical parameter for albedo (0.18)
$\tau_{\alpha,\mathrm{J14}}$	empirical parameter for albedo following Järvi et al. (2014) (0.18)
$\tau_{\alpha,\mathrm{V91}}$	empirical parameter for albedo following Verseghy (1991) (0.008)
ϕ	any scalar quantity
ϕ_0	basic state part of ϕ
$\tilde{\phi}$,	deviation of ϕ
ψ_0	observation values of rain radar
ψ_{f}	rain radar model results
ψ_{m}	weighted mean of rain radar model values

References

Arakawa, A. and Lamb, V. R.: Computational Design of the Basic Dynamical Processes of the UCLA General Circulation Model, Method. Comput. Phys., 17, 173–265, https://doi.org/10.1016/b978-0-12-460817-7.50009-4, 1977.

Asai, T.: A Numerical Study of the Air-Mass Transformation over the Japan Sea in Winter, Journal of the Meteorological Society of Japan. Ser. II, 43, 1–15, https://doi.org/10.2151/JMSJ1965.43.1_1, 1965.

Badeke, R., Matthias, V., and Grawe, D.: Parameterizing the vertical downward dispersion of ship exhaust gas in the near field, Atmospheric Chemistry and Physics, 21, 5935–5951, https://doi.org/10.5194/ACP-21-5935-2021, 2021.

Baker, D. G., Skaggs, R. H., and Ruschy, D. L.: Snow Depth Required to Mask the Underlying Surface, Journal of Applied Meteorology and Climatology, 30, 387–392, https://doi.org/https://doi.org/10.1175/1520-0450(1991)030⟨0387:SDRTMT⟩2.0.CO;2, 1991.

Bell, L.: Analysis and evaluation of cold season characteristics and their future development: A case study for the region of Hamburg, PhD Thesis, University of Hamburg, Hamburg, Germany, URL https://ediss.sub.uni-hamburg.de/handle/ediss/11332, 2024.

Bergeron, O. and Strachan, I. B.: Wintertime radiation and energy budget along an urbanization gradient in Montreal, Canada, International Journal of Climatology, 32, 137–152, https://doi.org/10.1002/JOC.2246, 2012.

Bhumralkar, C. M.: Numerical Experiments on the Computation of Ground Surface Temperature in an Atmospheric General Circulation Model, Journal of Applied Meteorology and Climatology, 14, 1246–1258, https://doi.org/https://doi.org/10.1175/1520-0450(1975)014⟨1246:NEOTCO⟩2.0.CO;2, 1975.

Blocken, B. and Carmeliet, J.: A review of wind-driven rain research in building science, Journal of Wind Engineering and Industrial Aerodynamics, 92, 1079–1130, https://doi.org/10.1016/j.jweia.2004.06.003, 2004.

Boettcher, M.: Selected climate mitigation and adaptation measures and their impact on the climate of the region of Hamburg, PhD Thesis, University of Hamburg, Hamburg, Germany, URL https://ediss.sub.uni-hamburg.de/handle/ediss/7546, 2017.

Bohnenstengel, S. I., Schlünzen, K. H., and Beyrich, F.: Representativity of in situ precipitation measurements – A case study for the LITFASS area in North-Eastern Germany, Journal of Hydrology, 400, 387–395, https://doi.org/10.1016/J.JHYDROL.2011.01.052, 2011.

Bouteloup, Y., Seity, Y., and Bazile, E.: Description of the sedimentation scheme used operationally in all Météo-France NWP models, Tellus A, 63, 300–311, https://doi.org/10.1111/j.1600-0870.2010.00484.x, 2011.

Briscolini, M. and Santangelo, P.: Development of the mask method for incompressible unsteady flows, Journal of Computational Physics, 84, 57–75, https://doi.org/10.1016/0021-9991(89)90181-2, 1989.

Burgemeister, F., Clemens, M., and Ament, F.: Multi-year X-band weather radar observations in Hamburg (LAWR HHG), World Data Center for Climate (WDCC) at DKRZ, https://doi.org/10.26050/WDCC/LAWR_UHH_HHG, 2022.

Castelli, S. T. and Reisin, T. G.: Evaluation of the atmospheric RAMS model in an obstacle resolving configuration, Environmental Fluid Mechanics, 10, 555–576, https://doi.org/10.1007/s10652-010-9167-y, 2010.

Changnon, S. A., Shealy, R. T., and Scott, R. W.: Precipitation Changes in Fall, Winter, and Spring Caused by St. Louis, Journal of Applied Meteorology and Climatology, 30, 126–134, https://doi.org/https://doi.org/10.1175/1520-0450(1991)030%3C0126:PCIFWA%3E2.0.CO;2, 1991.

Chen, X., Yu, Z., Liu, Z., Cao, R., and Zhu, F.: A prediction model for roof snow distribution during long-period snowfall using Euler-Lagrangian method, Cold Regions Science and Technology, 190, 103 347, https://doi.org/10.1016/J.COLDREGIONS.2021.103347, 2021.

Claus, J., Coceal, O., Thomas, T. G., Branford, S., Belcher, S. E., and Castro, I. P.: Wind-Direction Effects on Urban-Type Flows, Boundary-Layer Meteorology, 142, 265–287, https://doi.org/10.1007/S10546-011-9667-4, 2012.

Costa, I. T., Wollmann, C. A., Writzl, L., Iensse, A. C., da Silva, A. N., de Freitas Baumhardt, O., Gobo, J. P. A., Shooshtarian, S., and Matzarakis, A.: A Systematic Review on Human Thermal Comfort and Methodologies for Evaluating Urban Morphology in Outdoor Spaces, Climate, 12, 30, https://doi.org/10.3390/cli12030030, 2024.

Coutu, S., Wyrsch, V., Rossi, L., Emery, P., Golay, F., and Carneiro, C.: Modelling wind-driven rain on buildings in urbanized area using 3-D GIS and LiDAR datasets, Building and Environment, 59, 528–535, https://doi.org/10.1016/j.buildenv.2012.09.022, 2013.

Cox, R., Bauer, B. L., and Smith, T.: A Mesoscale Model Intercomparison, American Meteorological Society, 79, 265–284, 1998.

Cristiano, E., Veldhuis, M. C. T., and Giesen, N. V. D.: Spatial and temporal variability of rainfall and their effects on hydrological response in urban areas - A review, Hydrology and Earth System Sciences, 21, 3859–3878, https://doi.org/10.5194/hess-21-3859-2017, 2017.

Deardorff, J. W.: Efficient prediction of ground surface temperature and moisture, with inclusion of a layer of vegetation, Journal of Geophysical Research: Oceans, 83, 1889–1903, https://doi.org/10.1029/JC083IC04P01889, 1978.

Deutscher Wetterdienst: https://www.dwd.de/DE/service/lexikon/Functions/glossar.html?lv2=101812&lv3=101906: accessed at 01.02.2022, 2022a.

Deutscher Wetterdienst: https://opendata.dwd.de/climate_environment/CDC/observations_germany/\radiosondes/low_resolution/historical/2019/: accessed at 01.02.2022, 2022b.

Dobre, R. G., Gaitanaru, D. S., and Gogu, C. R.: Snowmelt modelling aspects in urban areas, Procedia Engineering, 209, 127–134, https://doi.org/10.1016/j.proeng.2017.11.138, 2017.

Doms, G.: Fluid- und Mikrodynamik in numerischen Modellen konvektiver Wolken, Inst. für Meteorologie und Geophysik der Univ. Frankfurt/Main, 1985.

Doms, G., Förstner, J., Heise, E., Herzog, H.-J., Mironov, D., Raschendorfer, M., Reinhardt, T., Ritter, B., Schrodin, R., Schulz, J.-P., and Vogel, G.: A Description of the Nonhydrostatic Regional COSMO Model Part II : Physical Parameterizations, Deutscher Wetterdienst, Offenbach, Germany, URL www.cosmo-model.org, 2011.

Dong, C.: Remote sensing, hydrological modeling and in situ observations in snow cover research: A review, Journal of Hydrology, 561, 573–583, https://doi.org/10.1016/J.JHYDROL.2018.04.027, 2018.

Douville, H., Royer, J. F., and Mahfouf, J. F.: A new snow parameterization for the Météo-France climate model, Climate Dynamics, 12, 21–35, 1995.

Dutra, E., Balsamo, G., Viterbo, P., Miranda, P. M., Beljaars, A., Schar, C., and Elder, K.: An Improved Snow Scheme for the ECMWF Land Surface Model: Description and Offline Validation, Journal of Hydrometeorology, 11, 899–916, https://doi.org/10.1175/2010JHM1249.1, 2010.

Eichhorn, J. and Kniffka, A.: The numerical flow model MISKAM: State of development and evaluation of the basic version, Meteorologische Zeitschrift, 19, 81–90, https://doi.org/10.1127/0941-2948/2010/0425, 2010.

Ferner, K. S., Boettcher, M., and Schlünzen, K. H.: Modelling the heterogeneity of rain in an urban neighbourhood with an obstacle-resolving model, Meteorologische Zeitschrift, 32, 67–81, https://doi.org/10.1127/METZ/2022/1149, 2023.

Ferner, K. S., Boettcher, M., Sieck, K., and Voss, V.: Sensitivity studies on rain heterogeneity in Hamburg city centre using the obstacle-resolving model MITRAS, https://doi.org/10.26050/WDCC/MitrasWinterHamburg, dataset, DOI: 10.26050/WDCC/MitrasWinterHamburg, 2024.

Fischereit, J.: Influence of urban water surfaces on human thermal environments - an obstacle resolving modelling approach, PhD Thesis, University of Hamburg, Hamburg, Germany, URL https://ediss.sub.uni-hamburg.de/handle/ediss/8005, 2018.

Franke, J., Sturm, M., and Kalmbach, C.: Validation of OpenFOAM 1.6.x with the German VDI guideline for obstacle resolving micro-scale models, Journal of Wind Engineering and Industrial Aerodynamics, 104-106, 350–359, https://doi.org/10.1016/J.JWEIA.2012.02.021, 2012.

Freitag, B. M., Nair, U. S., and Niyogi, D.: Urban Modification of Convection and Rainfall in Complex Terrain, Geophysical Research Letters, 45, 2507–2515, https://doi.org/10.1002/2017GL076834, 2018.

Geletič, J., Lehnert, M., Resler, J., Krč, P., Middel, A., Krayenhoff, E. S., and Krüger, E.: High-fidelity simulation of the effects of street trees, green roofs and green walls on the distribution of thermal exposure in Prague-Dejvice, Building and Environment, 223, 109 484, https://doi.org/10.1016/J.BUILDENV.2022.109484, 2022.

Geleyn, J.-F., Catry, B., Bouteloup, Y., and Brožková, R.: A statistical approach for sedimentation inside a microphysical precipitation scheme, Tellus A: Dynamic Meteorology and Oceanography, 60, 649–662, https://doi.org/10.1111/j.1600-0870.2008.00323.x, 2008.

Gholamalipour, P., Ge, H., and Stathopoulos, T.: Wind-driven rain (WDR) loading on building facades: A state-of-the-art review, Building and Environment, 221, 109 314, https://doi.org/10.1016/J.BUILDENV.2022.109314, 2022.

Grawe, D., Schlünzen, K. H., and Pascheke, F.: Comparison of results of an obstacle resolving microscale model with wind tunnel data, Atmospheric Environment, 79, 495–509, https://doi.org/10.1016/j.atmosenv.2013.06.039, 2013.

Grawe, D., Bächlin, W., Brünger, H., Eichhorn, J., Franke, J., Leitl, B., Müller, W., Öttl, D., Salim, M. H., Schlünzen, K. H., Winkler, C., and Zimmer, M.: An Updated Evaluation Guideline for Prognostic Microscale Wind Field Models, 9th International Conference on Urban Climate, Toulouse, France, 2015.

Gunn, K. L. S. and Marshall, J. S.: The Distribution with Size of Aggregate Snowflakes, Journal of Meteorology, 15, 452–461, https://doi.org/10.1175/1520-0469(1958)015⟨0452:tdwsoa⟩2.0.co;2, 1958.

Haddid, H. A. and Al-Obaidi, K. M.: Examining the impact of urban canyons morphology on outdoor environmental conditions in city centres with a temperate climate, Energy Nexus, 8, 100 159, https://doi.org/10.1016/J.NEXUS.2022.100159, 2022.

Han, J. Y., Baik, J. J., and Lee, H.: Urban impacts on precipitation, Asia-Pacific Journal of Atmospheric Sciences, 50, 17–30, https://doi.org/10.1007/S13143-014-0016-7/METRICS, 2014.

Haney, C.: Beyond "Snow Shoveler's Infarction": Broadening perspectives on winter health risks, Geography Compass, 14, https://doi.org/10.1111/gec3.12494, 2020.

Hirota, T., Pomeroy, J. W., Granger, R. J., and Maule, C. P.: An extension of the force-restore method to estimating soil temperature at depth and evaluation for frozen soils under snow, Journal of Geophysical Research Atmospheres, 107, ACL 11–1–ACL 11–10, https://doi.org/10.1029/2001JD001280, 2002.

Ho, C. L. and Valeo, C.: Observations of urban snow properties in Calgary, Canada, Hydrological Processes, 19, 459–473, https://doi.org/10.1002/HYP.5544, 2005.

Hu, C., Tam, C. Y., liang Yang, Z., and Wang, Z.: Analyzing urban influence on extreme winter precipitation through observations and numerical simulation of two South China case studies, Scientific Reports 2024 14:1, 14, 1–21, https://doi.org/10.1038/s41598-024-52193-2, 2024.

Jensen, N. E. and Pedersen, L.: Spatial variability of rainfall: Variations within a single radar pixel, Atmospheric Research, 77, 269–277, https://doi.org/10.1016/j.atmosres.2004.10.029, 2005.

Järvi, L., Grimmond, C. S., Taka, M., Nordbo, A., Setälä, H., and Strachan, I. B.: Development of the Surface Urban Energy and Water Balance Scheme (SUEWS) for cold climate cities, Geoscientific Model Development, 7, 1691–1711, https://doi.org/10.5194/GMD-7-1691-2014, 2014.

Järvi, L., Grimmond, C. S., McFadden, J. P., Christen, A., Strachan, I. B., Taka, M., Warsta, L., and Heimann, M.: Warming effects on the urban hydrology in cold climate regions, Scientific Reports 2017 7:1, 7, 1–8, https://doi.org/10.1038/s41598-017-05733-y, 2017.

Katzfey, J., Schlünzen, K. H., and Hoffmann, P.: Effects of urban areas on the diurnal cycle of temperature and precipitation in a global climate simulation, Quarterly Journal of the Royal Meteorological Society, 150, 4885–4914, https://doi.org/10.1002/QJ.4847, 2024.

Kessler, E.: On the Distribution and Continuity of Water Substance in Atmospheric Circulations, Meteorological Monographs, 10, https://doi.org/10.1007/978-1-935704-36-2, 1969.

Khain, A. P., Beheng, K. D., Heymsfield, A., Korolev, A., Krichak, S. O., Levin, Z., Pinsky, M., Phillips, V., Prabhakaran, T., Teller, A., Heever, S. C. V. D., and Yano, J. I.: Representation of microphysical processes in cloud-resolving models: Spectral (bin) microphysics versus bulk parameterization, Reviews of Geophysics, 53, 247–322, https://doi.org/10.1002/2014RG000468, 2015.

Khalifa, A., Marchetti, M., Bouilloud, L., Martin, E., Bues, M., and Chancibaut, K.: Accounting for anthropic energy flux of traffic in winter urban road surface temperature simulations with the TEB model, Geoscientific Model Development, 9, 547–565, https://doi.org/10.5194/GMD-9-547-2016, 2016.

Kottek, M., Grieser, J., Beck, C., Rudolf, B., and Rubel, F.: World Map of the Köppen-Geiger climate classification updated, Meteorologische Zeitschrift, 15, 259–263, https://doi.org/10.1127/0941-2948/2006/0130, 2006.

Kubilay, A., Derome, D., Blocken, B., and Carmeliet, J.: CFD simulation and validation of wind-driven rain on a building facade with an Eulerian multiphase model, Building and Environment, 61, 69–81, https://doi.org/10.1016/j.buildenv.2012.12.005, 2013.

Kubilay, A., Derome, D., and Carmeliet, J.: Coupling of physical phenomena in urban microclimate: A model integrating air flow, wind-driven rain, radiation and transport in building materials, Urban Climate, 24, 398–418, https://doi.org/10.1016/j.uclim.2017.04.012, 2018.

Köhler, A.: Parameterisierung der Wolkenmikrophysik und der Strahlung in einem mesoskaligen Transport- und Strömungsmodell, Diploma Thesis, University of Hamburg, Hamburg, Germany, 1990.

Lange, I.: Wind, temperature, relative humidity, rain rate, surface pressure and soil temperature data at boundary layer weather mast Hamburg for 2019, Meteorological Institute, University of Hamburg, data obtained from ICDC, CEN, University of Hamburg, 2021.

Lee, W. Y., Gim, H. J., and Park, S. K.: Parameterizations of Snow Cover, Snow Albedo and Snow Density in Land Surface Models: A Comparative Review, Asia-Pacific Journal of Atmospheric Sciences 2023 60:2, 60, 185–210, https://doi.org/10.1007/S13143-023-00344-2, 2023.

Lemonsu, A., Bélair, S., Mailhot, J., Benjamin, M., Chagnon, F., Morneau, G., Harvey, B., Voogt, J., and Jean, M.: Overview and First Results of the Montreal Urban Snow Experiment 2005, Journal of Applied Meteorology and Climatology, 47, 59–75, https://doi.org/10.1175/2007JAMC1639.1, 2008.

Lemonsu, A., Bélair, S., Mailhot, J., and Leroyer, S.: Evaluation of the Town Energy Balance Model in Cold and Snowy Conditions during the Montreal Urban Snow Experiment 2005, Journal of Applied Meteorology and Climatology, 49, 346–362, https://doi.org/10.1175/2009JAMC2131.1, 2010.

Li, Q., Yang, J., and Yang, L.: Impact of Urban Roughness Representation on Regional Hydrometeorology: An Idealized Study, Journal of Geophysical Research: Atmospheres, 126, e2020JD033 812, https://doi.org/10.1029/2020JD033812, 2021.

Liu, J. and Niyogi, D.: Meta-analysis of urbanization impact on rainfall modification, Scientific Reports, 9, https://doi.org/https://doi.org/10.1038/s41598-019-42494-2, 2019.

Lopez-Cabeza, V., Loor-Vera, M., Diz-Mellado, E., Rivera-Gomez, C., and Galan-Marin, C.: Decoding outdoor thermal comfort: The role of location in urban canyon microclimate, Sustainable Energy Technologies and Assessments, 72, 104 095, https://doi.org/10.1016/j.seta.2024.104095, 2024.

Lu, Y., Yu, Z., Albertson, J. D., Chen, H., Hu, L., Pendergrass, A., Chen, X., and Li, Q.: Understanding the Influence of Urban Form on the Spatial Pattern of Precipitation, Earth's Future, 12, e2023EF003 846, https://doi.org/10.1029/2023EF003846, 2024.

López, S.: Numerische Modellierung Turbulenter Umströmungen von Gebäuden, Reports on Polar and Marine Research, 418, 93, 2002.

Malevich, S. B. and Klink, K.: Relationships between Snow and the Wintertime Minneapolis Urban Heat Island, Journal of Applied Meteorology and Climatology, 50, 1884–1894, https://doi.org/10.1175/JAMC-D-11-05.1, 2011.

Marginean, I., Cuaresma, J. C., Hoffmann, R., Muttarak, R., Gao, J., and Daloz, A. S.: High-Resolution Modeling and Projecting Local Dynamics of Differential Vulnerability to Urban Heat Stress, Earth's Future, 12, e2024EF004 431, https://doi.org/10.1029/2024EF004431, 2024.

Maronga, B., Gross, G., Raasch, S., Banzhaf, S., Forkel, R., Heldens, W., Kanani-Sühring, F., Matzarakis, A., Mauder, M., Pavlik, D., Pfafferott, J., Schubert, S., Seckmeyer, G., Sieker, H., and Winderlich, K.: Development of a new urban climate model based on the model PALM - Project overview, planned work, and first achievements, Meteorologische Zeitschrift, 28, 105–119, https://doi.org/10.1127/metz/2019/0909, 2019.

Maronga, B., Banzhaf, S., Burmeister, C., Esch, T., Forkel, R., Fröhlich, D., Fuka, V., Gehrke, K. F., Geletič, J., Giersch, S., Gronemeier, T., Groß, G., Heldens, W., Hellsten, A., Hoffmann, F., Inagaki, A., Kadasch, E., Kanani-Sühring, F., Ketelsen, K., Khan, B. A., Knigge, C., Knoop, H., Krč, P., Kurppa, M., Maamari, H., Matzarakis, A., Mauder, M., Pallasch, M., Pavlik, D., Pfafferott, J., Resler, J., Rissmann, S., Russo, E., Salim, M., Schrempf, M., Schwenkel, J., Seckmeyer, G., Schubert, S., Sühring, M., Tils, R. V., Vollmer, L., Ward, S., Witha, B., Wurps, H., Zeidler, J., and Raasch, S.: Overview of the PALM model system 6.0, Geoscientific Model Development, 13, 1335–1372, https://doi.org/10.5194/GMD-13-1335-2020, 2020.

Marshall, J. S. and Palmer, W. M.: The Distribution of Raindrops with Size, Journal of Meteorology, 5, 165–166, https://doi.org/https://doi.org/10.1175/1520-0469(1948)005⟨0165:TDORWS⟩2.0.CO;2, 1948.

Meinke, I., Maneke, M., Riecke, W., and Tinz, B.: Norddeutscher Klimamonitor - Klimazustand und Klimaentwicklung in Norddeutschland innerhalb der letzten 60 Jahre (1951-2010), DMG Mitteilung, 01, 2–11, 2014.

Meinke, I., Rechid, D., Tinz, B., Maneke, M., Lefebvre, C., and Isokeit, E.: Klima der Region – Zustand, bisherige Entwicklung und mögliche Änderungen bis 2100, Hamburger Klimabericht – Wissen über Klima, Klimawandel und Auswirkungen in Hamburg und Norddeutschland, pp. 15–36, https://doi.org/10.1007/978-3-662-55379-4_2, 2018.

Mittal, R. and Iaccarino, G.: Immersed Boundary Methods, Annual Review of Fluid Mechanics, 37, 239–261, https://doi.org/10.1146/annurev.fluid.37.061903.175743, 2005.

Moghadas, S., Gustafsson, A. M., Muthanna, T. M., Marsalek, J., and Viklander, M.: Review of models and procedures for modelling urban snowmelt, Urban Water Journal, 13, 396–411, https://doi.org/10.1080/1573062X.2014.993996, 2016.

Mori, K. and Sato, T.: Evaluating the Role of Snow Cover in Urban Canopy Layer on the Urban Heat Island in Sapporo, Japan with a Regional Climate Model, Journal of the Meteorological Society of Japan. Ser. II, 93, 581–592, https://doi.org/10.2151/JMSJ.2015-039, 2015.

Müller, W. and Seyfert, E.: ATKIS® data base revision and generation of digital topographic base maps, International Archives of Photogrammetry and Remote Sensing, 33, 710–717, 2000.

Niemczynowicz, J.: The rainfall movement — A valuable complement to short-term rainfall data, Journal of Hydrology, 104, 311–326, https://doi.org/10.1016/0022-1694(88)90172-2, 1988.

Oberkampf, W. L. and Trucano, T. G.: Verification and validation in computational fluid dynamics, Progress in Aerospace Sciences, 38, 209–272, https://doi.org/10.1016/S0376-0421(02)00005-2, 2002.

Oke, T. R., Mills, G., Christen, A., and Voogt, J. A.: Urban climates, Cambridge University Press, https://doi.org/10.1017/9781139016476, 2017.

Pedersen, L., Jensen, N. E., Christensen, L. E., and Madsen, H.: Quantification of the spatial variability of rainfall based on a dense network of rain gauges, Atmospheric Research, 95, 441–454, https://doi.org/10.1016/j.atmosres.2009.11.007, 2010.

Perryman, N. and Dixon, P. G.: A Radar Analysis of Urban Snowfall Modification in Minneapolis–St. Paul, Journal of Applied Meteorology and Climatology, 52, 1632–1644, https://doi.org/10.1175/JAMC-D-12-090.1, 2013.

Pielke, R. A.: Mesoscale Meteorological Modeling, Academic Press, 3rd edn., 2013.

Pielke, R. A., Cotton, W. R., Walko, R. L., Tremback, C. J., Lyons, W. A., Grasso, L. D., Nicholls, M. E., Moran, M. D., Wesley, D. A., Lee, T. J., and Copeland, J. H.: A comprehensive meteorological modeling system - RAMS, Meteorology and Atmospheric Physics, 49, 69–91, https://doi.org/10.1007/BF01025401, 1992.

Purr, C., Brisson, E., and Ahrens, B.: Convective rain cell characteristics and scaling in climate projections for Germany, International Journal of Climatology, 41, 3174–3185, https://doi.org/10.1002/JOC.7012, 2021.

Roeckner, E., Baeuml, G., Bonventura, L., Brokopf, R., Esch, M., Giorgetta, M., Hagemann, S., Kirchner, I., Kornblueh, L., Manzini, E., Rhodin, A., Schlese, U., Schulzweida, U., and Tompkins, A. K.: The atmospheric general circulation model ECHAM5. PART I: Model description, Max Planck Institute for Meteorology, Hamburg, Germany, 2003.

Rosenhagen, G., Schatzmann, M., and Schrön, A.: Das Klima der Metropolregion auf Grundlage meteorologischer Messungen und Beobachtungen, Klimabericht für die Metropolregion Hamburg, pp. 19–59, https://doi.org/10.1007/978-3-642-16035-6_2, 2011.

Salim, M. H., Schlünzen, K. H., and Grawe, D.: Including trees in the numerical simulations of the wind flow in urban areas: Should we care?, Journal of Wind Engineering and Industrial Aerodynamics, 144, 84–95, https://doi.org/https://doi.org/10.1016/j.jweia.2015.05.004, 2015.

Salim, M. H., Schlünzen, K. H., Grawe, D., Boettcher, M., Gierisch, A. M., and Fock, B. H.: The microscale obstacle-resolving meteorological model MITRAS v2.0: Model theory, Geoscientific Model Development, 11, 3427–3445, https://doi.org/10.5194/gmd-11-3427-2018, 2018.

Salvi, K. A. and Kumar, M.: Imprint of urbanization on snow precipitation over the continental USA, Nature Communications 2024 15:1, 15, 1–11, https://doi.org/10.1038/s41467-024-46699-6, 2024.

Samsel, K. S.: A method for assessing model extensions: Application to modelling winter precipitation with a microscale obstacle-resolving meteorological model (MITRAS v4.0), Zenodo [Code], https://doi.org/10.5281/zenodo.14269493, 2024.

Samsel, K. S., Boettcher, M., Grawe, D., Schlünzen, K. H., and Sieck, K.: A method for assessing model extensions: Application to modelling winter precipitation with a microscale obstacle-resolving meteorological model (MITRAS v4.0), Geoscientific Model Development (in review), 2025.

Schatz, J. and Kucharik, C. J.: Seasonality of the Urban Heat Island Effect in Madison, Wisconsin, Journal of Applied Meteorology and Climatology, 53, 2371–2386, https://doi.org/10.1175/JAMC-D-14-0107.1, 2014.

Schatzmann, M. and Leitl, B.: Issues with validation of urban flow and dispersion CFD models, Journal of Wind Engineering and Industrial Aerodynamics, 99, 169–186, https://doi.org/10.1016/J.JWEIA.2011.01.005, 2011.

Schatzmann, M., Bächlin, W., Emeis, S., Kühlwein, J., Leitl, B., Müller, W. J., Schäfer, K., and Schlünzen, H.: Development and validation of tools for the implementation of European air quality policy in Germany (Project VALIUM), Atmospheric Chemistry and Physics, 6, 3077–3083, https://doi.org/10.5194/acp-6-3077-2006, 2006.

Schlünzen, K. and Sokhi, R., eds.: Overview of Tools and Methods for Meteorological and Air Pollution Mesoscale Model Evaluation and User Training. Joint Report of COST Action 728 and GURME, GAW Report 181, World Meteorological Organization (WMO), Geneva, Switzerland, URL https://library.wmo.int/idurl/4/47523, 2008.

Schlünzen, K. H., Hinneburg, D., Knoth, O., Lambrecht, M., Leitl, B., López, S., Lüpkes, C., Panskus, H., Renner, E., Schatzmann, M., Schoenemeyer, T., Trepte, S., and Wolke, R.: Flow and transport in the obstacle layer: First results of the micro-scale model MITRAS, Journal of Atmospheric Chemistry, 44, 113–130, https://doi.org/10.1023/A:1022420130032, 2003.

Schlünzen, K. H., Hoffmann, P., Rosenhagen, G., and Riecke, W.: Long-term changes and regional differences in temperature and precipitation in the metropolitan area of Hamburg, International Journal of Climatology, 30, 1121–1136, https://doi.org/10.1002/joc.1968, 2010.

Schlünzen, K. H., Boettcher, M., Fock, B. H., Gierisch, A., Grawe, D., and Salim, M.: Scientific Documentation of the Multiscale Model System M-SYS, Meteorologisches Institut, University of Hamburg, MeMi Technical Report 4, p. 153 pp., 2018a.

Schlünzen, K. H., Boettcher, M., Fock, B. H., Gierisch, A., Grawe, D., and Salim, M.: Technical Documentation of the Multiscale Model System M-SYS, Meteorologisches Institut, University of Hamburg, MeMi Technical Report 3, p. 136 pp., 2018b.

Schlünzen, K. H., Riecke, W., Bechtel, B., Boettcher, M., Buchholz, S., Grawe, D., Hoffmann, P., Petrik, R., Schoetter, R., Trusilova, K., and Wiesner, S.: Stadtklima in Hamburg, pp. 37–53, Springer Berlin Heidelberg, https://doi.org/10.1007/978-3-662-55379-4_3, 2018c.

Shepherd, J. M.: A review of current investigations of urban-induced rainfall and recommendations for the future, Earth Interactions, 9, 1–27, https://doi.org/10.1175/EI156.1, 2005.

Shui, T., Liu, J., Zhang, P., Liu, S., and Zhao, Z.: Development of an urban canopy model for the evaluation of urban thermal climate with snow cover in severe cold regions, Building and Environment, 95, 160–170, https://doi.org/10.1016/J.BUILDENV.2015.09.016, 2016.

Shui, T., Liu, J., Xiao, Y., and Shi, L.: Effects of snow cover on urban surface energy exchange: Observations in Harbin, China during the winter season, International Journal of Climatology, 39, 1230–1242, https://doi.org/10.1002/JOC.5873, 2019.

Smoliak, B. V., Snyder, P. K., Twine, T. E., Mykleby, P. M., and Hertel, W. F.: Dense Network Observations of the Twin Cities Canopy-Layer Urban Heat Island, Journal of Applied Meteorology and Climatology, 54, 1899–1917, https://doi.org/10.1175/JAMC-D-14-0239.1, 2015.

Song, Y., Liu, H., Wang, X., Zhang, N., and Sun, J.: Numerical simulation of the impact of urban non-uniformity on precipitation, Advances in Atmospheric Sciences, 33, 783–793, https://doi.org/10.1007/S00376-016-5042-1/METRICS, 2016.

Stadtreinigung Hamburg: Snow-how sehr gefragt [press release 16.04.2024], URL https://www.stadtreinigung.hamburg/ueber-uns/pressemitteilungen/16-04-2024-winterdienstbilanz/, 2024.

Statistik Nord: Straßenverkehrsunfälle in Hamburg 2023 - Endgültige Ergebnisse, Statistisches Amt für Hamburg und Schleswig-Holstein, 2024.

Terink, W., Leijnse, H., van den Eertwegh, G., and Uijlenhoet, R.: Spatial resolutions in areal rainfall estimation and their impact on hydrological simulations of a lowland catchment, Journal of Hydrology, 563, 319–335, https://doi.org/10.1016/j.jhydrol.2018.05.045, 2018.

Theeuwes, N. E., Solcerová, A., and Steeneveld, G. J.: Modeling the influence of open water surfaces on the summertime temperature and thermal comfort in the city, Journal of Geophysical Research: Atmospheres, 118, 8881–8896, https://doi.org/10.1002/JGRD.50704, 2013.

Tominaga, Y.: Computational fluid dynamics simulation of snowdrift around buildings: Past achievements and future perspectives, Cold Regions Science and Technology, 150, 2–14, https://doi.org/10.1016/J.COLDREGIONS.2017.05.004, 2018.

Tominaga, Y., Okaze, T., and Mochida, A.: CFD modeling of snowdrift around a building: An overview of models and evaluation of a new approach, Building and Environment, 46, 899–910, https://doi.org/10.1016/J.BUILDENV.2010.10.020, 2011.

Trukenmüller, A., Grawe, D., and Schlünzen, K. H.: A model system for the assessment of ambient air quality conforming to EC directives, Meteorologische Zeitschrift, 13, 387–394, https://doi.org/10.1127/0941-2948/2004/0013-0387, 2004.

Uphoff, M.: Einflüsse von Wolkeneffektparametrisierung und Modellauflösung auf simuliertes bodennahes Ozon, PhD Thesis, University of Hamburg, Hamburg, Germany, URL https://ediss.sub.uni-hamburg.de/handle/ediss/6167, 2019.

VDI: Environmental meteorology - Prognostic microscale wind field models - Evaluation for flow around buildings and obstacles, Technical Report, VDI Guideline 3783, Blatt 9, 2017.

Verseghy, D. L.: Class—A Canadian land surface scheme for GCMS. I. Soil model, International Journal of Climatology, 11, 111–133, https://doi.org/10.1002/JOC.3370110202, 1991.

von Salzen, K., Claussen, M., and Schlünzen, K. H.: Application of the concept of blending height to the calculation of surface fluxes in a mesoscale model, Meteorologische Zeitschrift, 5, 60–66, https://doi.org/10.1127/METZ/5/1996/60, 1996.

Watanabe, N., Setoguchi, T., Maeda, K., Iwakuni, D., Guo, Z., and Tsutsumi, T.: Sustainable Block Design Process for High-Rise and High-Density Districts with Snow and Wind Simulations for Winter Cities, Sustainability, 9, 2132, https://doi.org/10.3390/SU9112132, 2017.

Wiesner, S., Bechtel, B., Fischereit, J., Gruetzun, V., Hoffmann, P., Leitl, B., Rechid, D., Schlünzen, K. H., and Thomsen, S.: Is It Possible to Distinguish Global and Regional Climate Change from Urban Land Cover Induced Signals? A Mid-Latitude City Example, Urban Science, 2, 34, https://doi.org/10.3390/URBANSCI2010012, 2018.

WMO: W.M.O.: Guide to Meteorological Instruments and Methods of Observation, WMO-No. 8, World Meteorological Organization (WMO), Geneva, Switzerland, 7 edn., 2008.

WMO: Guide to Instruments and Methods of Observation Volume I - Measurement of Meteorological Variables, 2023 edition, WMO-No. 8, World Meteorological Organization (WMO), Geneva, Switzerland, URL https://library.wmo.int/idurl/4/68695, 2023a.

WMO: Guidance on Measuring, Modelling and Monitoring the Canopy Layer Urban Heat Island (CL-UHI), WMO-No. 1292, World Meteorological Organization (WMO), Geneva, Switzerland, 2023b.

Zhang, Q., Zhang, Y., Yin, Z., Zhang, G., Mo, H., and Fan, F.: Experimental Study of Interference Effects of a High-Rise Building on the Snow Load on a Low-Rise Building with a Flat Roof, Applied Sciences 2021, 11, 11 163, https://doi.org/10.3390/APP112311163, 2021.

Zhang, W., Yang, J., Yang, L., and Niyogi, D.: Impacts of City Shape on Rainfall in Inland and Coastal Environments, Earth's Future, 10, https://doi.org/10.1029/2022EF002654, 2022.

Zhou, X., Liu, Z., Ma, W., Kosugi, K., and Gu, M.: Experimental investigation of snow drifting on flat roofs during snowfall: Impact of roof span and snowfall intensity, Cold Regions Science and Technology, 190, 103 356, https://doi.org/10.1016/J.COLDREGIONS.2021.103356, 2021.

Versicherung an Eides statt

Hiermit erkläre ich an Eides statt, dass ich die vorliegende Dissertationsschrift selbst verfasst und keine anderen als die angegebenen Quellen und Hilfsmittel benutzt habe.
Sofern im Zuge der Erstellung der vorliegenden Dissertationsschrift generative Künstliche Intelligenz (gKI) basierte elektronische Hilfsmittel verwendet wurden, versichere ich, dass meine eigene Leistung im Vordergrund stand und dass eine vollständige Dokumentation aller verwendeten Hilfsmittel gemäß der Guten wissenschaftlichen Praxis vorliegt. Ich trage die Verantwortung für eventuell durch die gKI generierte fehlerhafte oder verzerrte Inhalte, fehlerhafte Referenzen, Verstöße gegen das Datenschutz- und Urheberrecht oder Plagiate.

Hamburg, den 03.02.2025 (Karolin S. Samsel)